Photometric Calibration of Wide Field Imagers

Nicolas Regnault

Thèse d'Habilitation

Photometric Calibration of Wide Field Imagers

On Light Emitting Diodes, Stars and Supernovae

Nicolas Regnault

December 1, 2012

soutenue le 8 janvier 2013, devant le jury composé de:

Mamoru Doi	rapporteur,
Mike Irwin	rapporteur,
David Burke	rapporteur,
Michael Joyce	examinateur,
François Pajot	examinateur.
Michel Piat	examinateur.

Laboratoire de Physique Nucléaire et de Hautes-Énergies
IN2P3 - CNRS - UPMC - UPD
Barre 12-22 1er étage
4 place Jussieu
75252 Paris CEDEX 05

Contents

EDWIN HUBBLE'S CAR

— http://xkcd.com/1125/

Introduction

In this document, I describe my past activities, on supernova cosmology and photometric calibration, within the Supernova Legacy Survey (SNLS). When I joined the LPNHE Cosmology Group, at the end of 2004, the subject was not entirely new to me, as I had done my PhD on the measurement of H_0 with nearby type Ia supernovae. Discovering and following up a dozen of SNe Ia was a difficult task at that time. I had been lucky enough to be able to catch and follow-up about 20 of them. This allowed me to verify that the standardization relations proposed by Tripp (1998) were indeed working pretty well. I was also able to re-derive yet another measurement of H_0, anchored on the few nearby SNe Ia with Cepheid distances that were available.

When I first heard about SNLS (I was a postdoc in Saul Perlmutter's group at that time) the project immediately appeared to me as a game changer, and I decided to join the Paris group as soon as I could. This took a little more time than I had initially anticipated. Before then, I spent two enjoyable years working at Laboratoire Leprince Ringuet (École Polytechnique, Palaiseau, France) on the CMS experiment.

When I arrived in the group, SNLS was already taking data, and the first year analysis was starting to take form. There were still many standing problems though, among which "a few things to be checked with the survey calibration". I took up the task, and it appeared quickly that calibration would be our main source of systematics for quite a while. And indeed, our calibration related systematics are just starting to decrease, after seven years of intense work. Despite these small difficulties, SNLS turned out to be a game changer indeed. We were ourselves amazed by the precision we were able to attain with just the first year data (Astier et al., 2006).

Working within the LPNHE Cosmology group has been a wonderful experience. Data, ideas, thoughts and tasks are freely shared between members, allowing the group to be much more than just a collection of individuals. For a young physicist such as I, this has been an extremely formative experience.

In the tradition of the french "habilitation theses", this document should be seen as a collection of reviews, on a selection of subjects I have been working on since I obtained my PhD. Supernova cosmology (chapter 1) has attracted a lot of attention over the last years. As a consequence, it is difficult to produce something very original. I tried to write an introductory text as complete and easy to read as possible, that could be helpful for newcomers in the field. Photometric calibration (chapter 2) is a more esoteric topic, seldom covered in reviews. It is also a vast subject, and calibrators generally have very different requirements, depending on the science goals they pursue. Here, I deliberately adopted the perspective of a dark energy survey designer, for whom all what matter is

the relative flux calibration of the imager passbands. The last chapter (chapter 3) is on instrumental calibration. This is a relatively new field, that emerged over the last decade. Since 2005, a flurry of instrumental calibration projects have been initiated, all with very different designs. Many are currently being tested on real instruments, and it is quite difficult to predict today which design is going to emerge from this worldwide competition. I will give an overview of this rapidly evolving field, concentrating on the calibrated sources, that are used to characterize wide field imagers. I also took the liberty to present in detail the DICE project with which I have been involved for the last three years.

1 Supernova Cosmology

1.1 Introduction

The discovery, at the turn of the century, that cosmic expansion was accelerating (Perlmutter et al., 1999; Riess et al., 1998) was met with less skepticism than could have been anticipated. The most natural way to explain this astonishing result was indeed to add a "Cosmological Constant" or some sort of "Dark Energy" to the constituents of the Universe. And it happens that at that time, there was a growing need for such an addition.

Before the discovery of cosmic acceleration, the dominant cosmological model was the "Einstein-de Sitter" (EdS) Universe, flat and matter dominated. Flatness was strongly motivated from inflationary scenarios introduced in the 1980s to explain the almost perfect isotropy of the cosmic microwave background. However, there were hints for a much lower matter density, either from galaxy clustering (Efstathiou et al., 1990; Bahcall and Fan, 1998), from cluster baryon mass fraction (White et al., 1993), or from persisting disagreements between the expansion age of the Universe and the age of the oldest globular clusters (e.g. Chaboyer et al., 1996)[1].

The evidence for a non-zero cosmological constant solved the tension between the observationally favored low-matter-density Universe and the theoretically motivated flat Universe. At about the same time, the precise measurement of the first peak of the CMB temperature anisotropy spectrum (de Bernardis et al., 2000), combined with the results of the HST key project to measure the Hubble constant (Freedman et al., 2001) gave strong constraints on the flatness, completing the puzzle.

The Concordance Model The cosmological model that emerged from this remarkable series of measurements is now called the "Concordance Model", or the "Standard Model of Cosmology". It is a consistent theoretical framework, which predicts, as a function of a limited number of free parameters, a wide variety of cosmological observations, such as the cosmic expansion (e.g. Suzuki et al., 2012), the temperature and polarization anisotropies of the CMB (Komatsu et al., 2011), the abundances of light elements (Fields and Olive, 2006), and the large scale structure of matter (Percival et al., 2007a). A notable success is the recent detection of the baryon acoustic peak in the galaxy power

[1] About forty years earlier, Sandage (1961) had noted potential disagreements between the expansion age and the lower limits from stellar studies, and mentioned $\Lambda > 0$ as a way to reconcile both estimates.

spectrum (Anderson et al., 2012; Percival et al., 2007b; Eisenstein et al., 2005). All these cosmological probes yield independent, but very concordant constrains on the standard model parameters.

With such a model now firmly established, the nature of observational cosmology has changed. We have entered an era of precision cosmology, and current projects are now in a position to challenge the standard model predictions, with precision measurements performed with many complementary probes. This allows one to over-constrain the cosmological parameters, and detect potential tensions between various predictions of the standard model.

The Dark Universe There is one last frontier however (some would say 'fortunately'), which cosmologists have started to explore over the last decade. It is the so-called "dark sector" of the cosmological model. The first mystery here is Dark Matter. There is ample evidence for the presence of non-baryonic, non relativistic Dark Matter at all scales in the Universe. Observational indications come from the rotation speed of galaxies, the motion of galaxies within clusters, or the temperature anisotropies of the CMB. Dark Matter density ($\sim 20\%$ of the total) exceeds by far the baryon density ($\sim 4\%$), making it about five times more prevalent in the Universe than normal matter. Only its gravitational effects have been detected so far, and nothing is known about its nature. Standard candidates today are either light supersymmetric particles (WIMPS) or axions (see e.g. Feng, 2010; Bertone et al., 2005). Up to now, this mysterious constituent has escaped all indirect (Porter et al., 2011) and direct (Brink, 2012) detection efforts.

Even more mysterious is the nature of Dark Energy, the hypothetical fluid introduced to explain cosmic acceleration, that seems to constitutes about 70% of the total energy density today. Actually, the term "Dark Energy" loosely refers to a wide range of models. A standard explanation is the Cosmological Constant, a modification of the Einstein equation, that can be interpreted as an additional fluid, of constant density and repulsive gravitational effect. A natural candidate for this is quantum vacuum energy. Unfortunately, natural values of vacuum energy seem to be many orders of magnitude larger than what is suggested by the observations[2] (Carroll, 2001; Weinberg, 1989). Another problem is the strange coincidence between the constant dark energy density and the matter density today. Since the latter varies as $(1+z)^3$, (for example, it has varied by a factor 10^{27} since big-bang nucleosynthesis), how come that we happen to live precisely at a time where both are almost equal ?

Many alternatives to a cosmological constant have been proposed (see e.g. Kunz, 2012; Copeland et al., 2006). Among the most popular are the Quintessence models that hypothesize a (undiscovered yet) particle field, with some level of self-interactions, modeled using a potential V. Judiciously choosing the shape and time evolution of V, it is possible to reproduce the behavior of a gravitationally repulsive fluid. More

[2] see however the discussion in (Martin, 2012) who shows that when applying a proper regularization scheme, the obtained vacuum energy density is much closer to what is being observed.

importantly, a subclass of potentials exhibit fixed points and attractors that make the field average energy density reach and then follow naturally the density of radiation and then matter. A nice feature of these models is that the field energy density at later times (i.e. today) is essentially independent of its initial value, making the coincidence more natural.

How can we discriminate between dark energy models ? Macroscopically, they exhibit different equations of state $p = w \times \rho$. The equation of state encodes the macroscopic properties of the field, in particular the evolution of its energy density and pressure with expansion. As we will see later, several cosmological probes, such as the study of cosmic expansion, are actually sensitive to w. Hence, it is possible to measure w (as well as its potential variations as a function of time or z) and to select the dark energy models compatible with the observations. As an example, most natural quintessence models exhibit a variable equation of state with $w > -0.8$ today, which is currently disfavored by the observations. The fluid associated to a cosmological constant has a static equation of state $p_\Lambda = -\rho_\Lambda$ (i.e. $w_\Lambda = -1$).

Cosmology with Type Ia Supernovae Type Ia supernovae (SNe Ia) have played an essential role in the elaboration of the concordance model. These stellar explosions proved to be the first reliable standard candles observable at cosmological distances. Early work by Tripp (1998); Riess et al. (1996); Phillips (1993); Pskovskii (1984) showed that the luminosities of SNe Ia could be standardized, yielding relative luminosity distance measurements precise at the level of 10% or better. Comparing SN Ia luminosity distances to their redshifts is the most direct probe of the expansion history of the Universe.

Nearby SNe Ia were first used to measure distances out in the linear Hubble flow, and were key to obtain the first accurate estimates of the expansion rate today, H_0 (Freedman et al., 2001). At about the same time, two independent groups, the Supernova Cosmology Project[3] and the High-z Supernova Search[4], set out to discover distant SNe Ia and measure the departure of the Hubble law from linearity at larger redshifts. The goal was to measure the then called "deceleration parameter", q_0, which would allow to place a constrain on the density and curvature of the Universe. These efforts culminated with a big surprise, the discovery of the accelerated expansion (Perlmutter et al., 1999; Riess et al., 1998), which turned out to be a very welcome fact after all.

Like all astrophysical objects, supernovae must be subject to cosmic evolution: since the chemical composition of the Universe evolves with time, the characteristics of distant and nearby SNe Ia, in particular, their average intrinsic luminosities, should differ at some extent. It was therefore anticipated that SNe Ia would quickly become less and less competitive, as evidence for evolution, and/or sensitivity to their environment would start to accumulate.

Ten years after the discovery of cosmic acceleration however, SNe Ia are still a major

[3] http://supernova.lbl.gov/
[4] http://www.cfa.harvard.edu/supernova/HighZ.html

player in the field. There are two reasons for this. First, constraining the expansion history at intermediate redshifts ($0.05 < z < 1$) is the most sensitive probe of w. In other words, it is the most efficient way to characterize Dark Energy. Second, for a given observing time budget, it is the probe which has the greatest statistical power. Indeed, is relatively easy, with today's wide field imagers, to accumulate hundreds — and soon thousands — of SNe Ia up to a redshift of 1. Given the intrinsic dispersion of SNe Ia, this allows one to measure the distance-redshift relation with a precision of $\sim 2\%$ at all redshifts (in redshift bins of ~ 0.1). Obtaining similar constrains by measuring, for example, the position of the baryon acoustic peak at several redshifts, requires to obtain over a million of galaxy spectra. Even with wide field spectrographs that can observe hundreds of objects at a time, this necessitates about 10 times as much observing time.

Systematics All recent measurements of the cosmological parameters performed with type Ia supernovae are now dominated by systematic uncertainties (see e.g. Conley et al., 2011). However, no uncertainty of astrophysical origin dominates the uncertainty budget on w. Quite unexpectedly, the major contribution to the systematic error budget rather comes from the photometric calibration of the imagers used to measure the supernova fluxes. Since this problem is purely of instrumental origin, it should be possible in theory to improve significantly the constrains delivered by current and future supernova surveys. On the other hand, if no progress is made on the subject, supernovae may not be able to improve much on the current results.

In this memoir, we describe the efforts invested by the major supernova surveys to obtain a sub-percent precision on their photometric calibration. The standard approach, relying on observations of stable stellar calibrators has been greatly optimized over the past few years. In particular, the traditional calibration paths that link the science observations to the fundamental calibrators have been drastically shortened (Betoule et al., 2012; Regnault et al., 2009; Holtzman et al., 2008). However, it seems that these techniques have now reached their limits and instrumental calibration techniques, relying on artificial light sources and laboratory flux standards are being investigated by several groups (Stubbs et al., 2010; Doi et al., 2010; Barrelet and Juramy, 2008).

The chapter is organized as follows. Section 1.2 will summarize the minimal cosmological background necessary to understand the measurements. In §1.3 we describe briefly the physics and the properties of SNe Ia. We then (§1.4) present the measurement principles, and summarize the results reported by recent supernova surveys (§1.5). Finally, we discuss where calibration enters the measurement, and why it has such a strong impact on the final result.

1.2 The Friedmann Universe

In this section, we summarize the essential concepts and formulas needed to understand the measurements performed with type Ia supernovae. We do not go deep into details,

as the subject is covered in all cosmology textbooks. The interested reader can refer to e.g. Rich (2010); Dodelson (2003) or Peacock (1999).

1.2.1 The Friedmann Equations

Metric On the large scales, the Universe is homogeneous and isotropic. A metric that allows for this is the Friedman-Lemaître-Robertson-Walker metric (FLRW, see e.g. Robertson, 1929; Walker, 1936):

$$ds^2 = dt^2 - a^2(t) \times \left(\frac{dr^2}{1 - kr^2} + r^2(d\theta^2 + \sin^2\theta \; d\phi^2) \right) \tag{1.1}$$

where $k = -1, 0, 1$ depend on whether the spacetime is open, flat or closed respectively. $a(t)$ is the scale factor, and encodes a global expansion or contraction of space.

Redshift The metric defines the space-time geodesics followed by massless particles, such as photons. One shows that the wavelengths of photons travelling between two comoving observers are related by:

$$\frac{\lambda_{\text{observer}}}{\lambda_{\text{emitter}}} = \frac{a_{\text{observer}}}{a_{\text{emitter}}} = 1 + z \tag{1.2}$$

z is called the redshift of the source. It can be measured accurately using spectroscopic observations of the object, by comparing the observed positions of identified absorption or emission lines with their expected positions known from laboratory measurements. The consequence of this, is that we have a direct observable to probe the relative variations of the scale factor a.

Friedmann equation(s) The Einstein equation connects the geometry of spacetime with the gravitation sources. Within the FLRW metric, its translates into two differential equations, originally derived by Friedmann (1922):

$$\left(\frac{\dot{a}}{a}\right)^2 = \frac{8\pi G}{3}\rho - \frac{k}{a^2(t)} + \frac{\Lambda}{3} \tag{1.3}$$

$$\left(\frac{\ddot{a}}{a}\right) = -\frac{4\pi G}{3}(\rho + 3p) + \frac{\Lambda}{3} \tag{1.4}$$

where Λ is the cosmological constant, ρ the total energy density of the fluids populating the Universe, and p their pressure. Pressure and density vary with the expansion. These variations depend on the properties of the fluid, generally encoded into its equation of state (EoS): $p = w \times \rho$. Inspecting equations (1.3) and (1.4), we see that the cosmological constant itself can be considered as an additional fluid, of constant density $\rho_\Lambda = \Lambda/8\pi G$. One also notices that $p_\Lambda = -\rho_\Lambda$.

	w	$\rho(a)$	$a(t)$
Non relativistic matter	0	a^{-3}	$t^{2/3}$
Radiation	1/3	a^{-4}	$t^{1/2}$
Λ	-1	a^0	$\exp(\Lambda t)$
Dark Energy	w	$a^{-3(1+w)}$	$t^{2/3(1+w)}$

Table 1.1: Properties of common fluids in the Universe. The $a(t)$ columns describes the evolution of the scale factor when this fluid dominates (i.e. neglecting all other fluids), in a flat Universe.

Conservation of Energy For a fluid of density ρ and pressure p enclosed in a volume $V \propto a^3$, we have $d(\rho V) = -pdV$, or equivalently:

$$\frac{d}{dt}(\rho a^3) = -3p\dot{a}a^2 \tag{1.5}$$

We see from the equation above, that for a fluid of constant density, we should have $p = -\rho$. So, for a cosmological constant, we should have $w = -1$.

Let's now consider a fluid that obeys equation of state: $p = w \times \rho$. It is easy to show from equation (1.5) above that its energy density varies like:

$$\rho(z) = \rho_0 \times a^{-3(1+w)} \tag{1.6}$$

if w is constant, and like

$$\rho(z) = \rho_0 \times \exp\left(3\int_0^z \frac{1+w(z')}{1+z'}dz'\right) \tag{1.7}$$

if w varies with time (e.g. $p = w(z) \times \rho$). Table (1.1) summarizes the properties of common fluids such as non-relativistic matter ($w = 0$) and radiation ($w = 1/3$). One notices that the densities of matter, radiation and "dark energy" vary at very different rates. This is illustrated on figure 1.1. Radiation used to be dominant in the early phases of the Universe (until $z \sim 4000$) but is completely negligible today. The matter dominated era ended quite recently (around $z \sim 0.5$), and we happen to live at a very special epoch, where the matter and "dark energy" densities are comparable.

Note that the two Friedman equations are not independant. For example (1.4) can be derived from (1.3) taking into account the conservation of energy to eliminate p. Knowing the equations of state of all fluids (hence, knowing how their densities vary with a), and given initial conditions (e.g. the densities today), one can solve equation 1.3 and obtain $a(t)$.

Hubble constant The Hubble parameter is defined as:

$$H(z) = \frac{\dot{a}}{a} \tag{1.8}$$

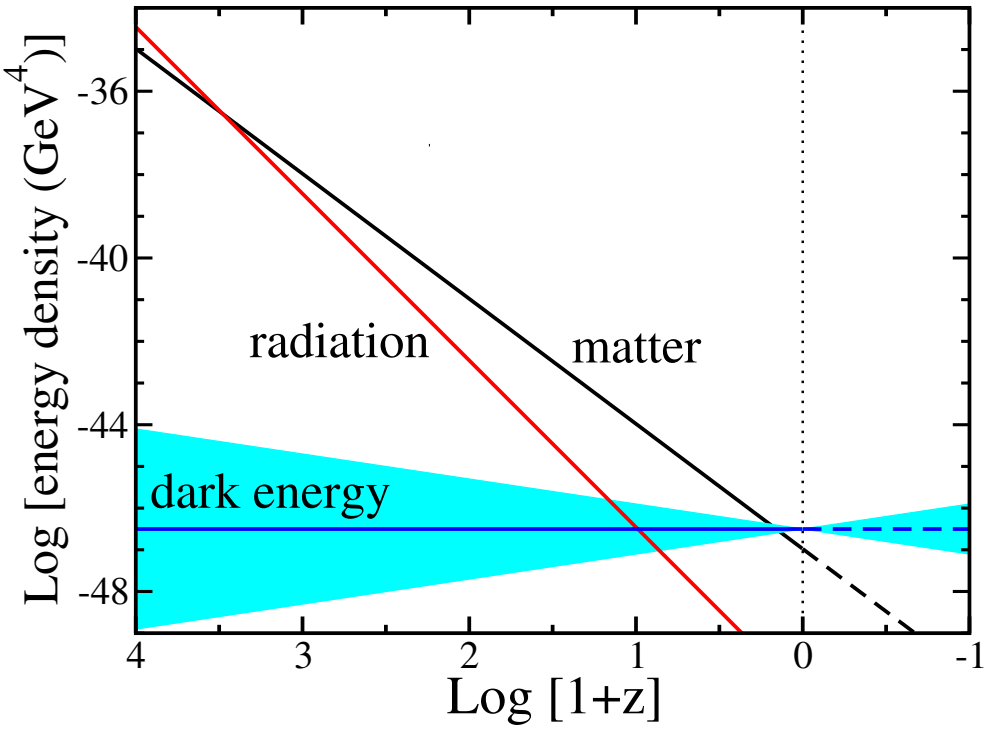

Figure 1.1: Evolution of the matter, radiation and "dark energy" densities as a function of z. The matter-radiation equality happened around $z \sim 4000$. The matter dominated era ended recently, around $z \sim 0.5$. The uncertainty band for dark energy corresponds to $w = -1 \pm 0.2$. (from Frieman et al., 2008).

and we note H_0 its current value (at redshift $z = 0$). H_0 is homogeneous to the inverse of a time, and generally expressed in kilometers per second and per megaparsec (km s^{-1} Mpc^{-1}). The absolute distance scale and age scale (in physical units) are proportional to $1/H_0$ (the so called "Hubble time"). After decades of uncertainties and controversies on the measurement of the Hubble constant, the first accurate (and consensual) determination was reported by Freedman et al. (2001). Combining several distance measurement techniques, all anchored on the cepheid distance scale they find $H_0 = 72 \pm 8$ km s^{-1} Mpc^{-1} (stat + sys). This estimate was refined by Riess et al. (2009) who report, using a larger cepheid sample all observed with the same instrument: $H_0 = 74.2 \pm 3.6$ km s^{-1} Mpc^{-1} (stat + sys).

Cosmological Parameters The parameters upon which $a(t)$ depends are the densities and equations of state of all the fluids that compose the Universe. These are a subset

of the ΛCDM parameters. In the framework of ΛCDM, these are: (1) non-relativistic matter (dark matter and baryons) and (2) dark energy. These parameters are generally expressed in fractions of today's critical density ρ_c, i.e. the energy density that gives a flat Universe ($k = 0$). From equation (1.3)

$$\rho_c = \frac{3H_0^2}{8\pi G} \tag{1.9}$$

and one defines:

$$\Omega_{\rm X} = \frac{\rho_{\rm X}}{\rho_c}, \quad \Omega_{\rm m} = \frac{\rho_{\rm m}}{\rho_c} = \frac{3\pi G\rho_{\rm m}}{3H_0^2}, \quad \Omega_\Lambda = \frac{\Lambda}{3H_0^2}, \quad \Omega_k = -\frac{k}{a_0^2 H_0^2} \tag{1.10}$$

From the definitions above and from (1.3) we find that the Friedman equation can be rewritten as:

$$H^2(z) = H_0^2\left(\Omega_{\rm m}(1+z)^3 + \Omega_k(1+z)^2 + \Omega_{\rm X}(1+z)^{3(1+w_{\rm X})}\right) \tag{1.11}$$

In the equation above, we have neglected today's radiation density $\Omega_{\rm r}$ which is a few 10^{-5} of the critical density. We have also introduced a generalized form of dark energy, characterized by its (unknown) equation of state $p = w \times \rho$. In particular: $\Omega_{\rm m} + \Omega_{\rm X} + \Omega_k = 1$. Equation (1.11) encodes the expansion history as a function of today's value of the cosmological parameters $(\Omega_{\rm m}, \Omega_k, \Omega_X, w)$.

Luminosity distance If one knows the instrinsic luminosity $\mathcal{L}$ (i.e. restframe energy per restframe unit time) of a distant astrophysical object, one can estimate its luminosity distance d_L defined as:

$$d_L = \sqrt{\frac{\mathcal{L}}{4\pi\phi}} \tag{1.12}$$

Objects or events of known (or at least, uniform) luminosities are called *standard candles*.

It can be shown that d_L is a simple function of the integrated expansion history ($\int H^{-1}dz$). Indeed, for a source at redshift z, one has:

$$d_L(z) = \frac{1+z}{H_0\sqrt{|\Omega_k|}}\ \mathcal{S}_k\left(H_0\sqrt{|\Omega_k|}\int_0^z \frac{dz'}{H(z')}\right) \tag{1.13}$$

where $\mathcal{S}_k(x) = \sin(x), x, \sinh(x)$ for $k = -1, 0, +1$ and $H(z)$ is given by equation (1.11). Therefore, constraining $d_L(z)$ over a large enough redshift range gives a constraint on the cosmological parameters. As shown on figure (1.2) one should expect degeneracies. In fact, one obtains one unique constraint on the cosmological parameters. It is apparent on the second panel that the probe is sensitive to the value of w, provided that one can measure luminosity distances at the percent level in the redshift range $0.4 \lesssim z \lesssim 1$..

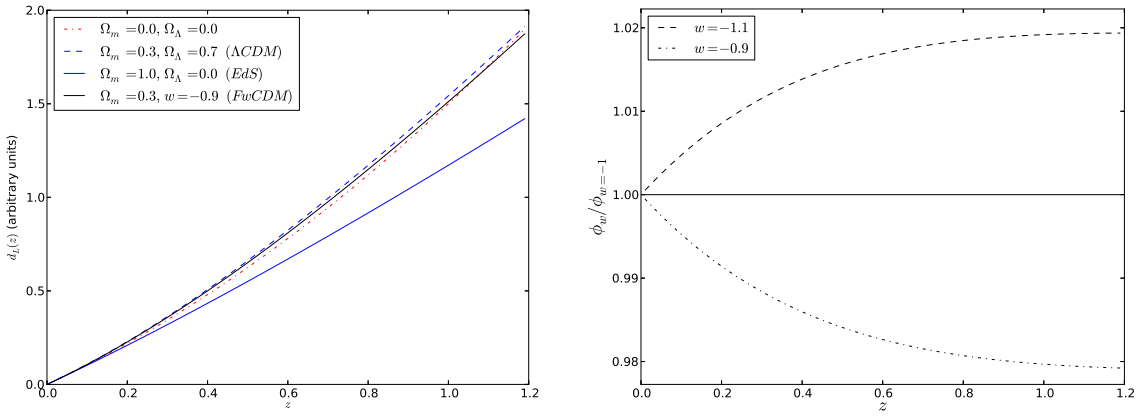

(a) $d_L(z)$ (b) Rel. $d_L(z)$

Figure 1.2: Effect of dark energy on comoving distances. Left: $d_L(z)$ for various cosmological models. The quasi-degeneracy between models is clearly visible. Right: sensitivity of $d_L(z)$ to the value of w. A variation of w of ~ 0.1 results in a variation of $d_L(z)$ of less than 2% at a redshift of 0.8. This sets a precision requirement on the measurement of the luminosity distances.

Classical Cosmological Tests The idea of studying the expansion history of the Universe, in order to "discriminate between world models" is as old as the discovery of cosmic expansion (Hubble and Humason (1931); Hubble (1929); Lemaître (1927)). Classical cosmological tests, all geometrical in essence, were devised in the early 1930s to map the expansion and constrain the density and curvature of the Universe. All these tests consist in comparing distances, look-back times or comoving volumes to redshift measurements. As soon as the Hale 200-inch telescope (Palomar Observatory, CA, USA) became available for research, large programs were initiated to carry out these tests (see Sandage, 1961, for a review). Measuring redshifts of objects at cosmological distances proved feasible. It essentially required a spectrograph, a large mirror and large amounts of observing time. On the other hand, all the initial attempts at measuring cosmological distances, relying on galaxies as standard candles, were plagued by strong evolution effects. Despite immense efforts, little progress was made for almost 40 years (Sandage, 1988), and in the 1980s, it became obvious that galaxies could not be used as standard markers.

1.3 Type Ia Supernovae

The term "super-nova" seems to have been coined by Baade and Zwicky (1934). They were the first to make the distinction between the *common novae*, and the much less

common *super-novae*, which are about 10^4 brighter and can be detected at extragalactic distances. Novae occur from runaway nuclear fusion reactions at the surface of white dwarfs accreting material from a companion. The physics of super-novae has long been a mystery and remains an area of active research today.

The first provisional supernova classification was proposed by (Minkowski, 1941). Inspecting the first supernova spectra, he noted that some lacked the presence of any hydrogen lines, but displayed strong silicon (Si II) features, while others showed Balmer lines, characteristics of the presence of hydrogen. The former were denominated "Type I supernovae", and the others, "type II supernovae". It was later realized from photometric and spectroscopic observations of larger supernova samples, that the hydrogen-deficient type I supernovae could be subdivided into several subclasses (Wheeler and Harkness, 1990; Elias et al., 1985), namely type Ia (strong Si II features), and type Ib/Ic (no silicium).

The consensus today is that type II and type Ibc events are associated to the gravitational collapse of massive ($\gtrsim 8M_\odot$) stars, while type Ia events are rather the thermonuclear explosion of carbon-oxygen white dwarfs having reached the Chandrasekhar limit ($\sim 1.4M_\odot$). The typical lifetime of massive stars is short ($10^6 - 10^7$ years). Hence, core-collapse SNe trace star formation history, and are found almost exclusively in active (star-forming) galaxies. White dwarfs are much older, and indeed SNe Ia are detected in all sorts of environments, (star forming or not).

1.3.1 Photometric and Spectroscopic Properties

Figure (1.3) shows typical SN Ia light curves and spectra. SNe Ia rise in about 17.4 days, reach a maximum, of a few 10^9 solar luminosities ($L_\odot$), and then decline in a few months (e.g Hayden et al., 2010). The luminosity of SNe Ia is set by the β and γ decay of the large quantities of ^{56}Ni synthesized during the explosion, more specifically, by the decay chain $^{56}\mathrm{Ni} \rightarrow {}^{56}\mathrm{Co} \rightarrow {}^{56}\mathrm{Fe}$ (e.g. Arnett, 1982). The half life of ^{56}Ni (6.1 days) is short compared to the rise time of the supernova. ^{56}Co is much longer lived, with a half time of 77 days. When the SN Ia reaches its maximum, ^{56}Co has not decayed yet, hence SNe Ia peak luminosities should be correlated primarily with the amount of ^{56}Ni initially present. Late time late curves are quasi-exponential, with a logarithmic slope that matches what can be expected from the decay of ^{56}Co.

Initially, the supernova envelope is optically thick. The $\gamma-$rays released by the radioactive decays are thermalized through Compton scattering and absorption/emission by the partially ionized atoms of the medium. At peak luminosity, most of the light is emitted in the optical, around 4000Å. As the supernova expands, the (wavelength-dependent) opacity of the medium varies. The SN light curve shape is the result of the rate of energy deposition modulated by these non-trivial opacity variations (note e.g. on figure (1.3) the secondary shoulder observed in the redder bands).

SN Ia spectra display strong absorption features from intermediate elements, such as Si II and Ca II. These features are blue-shifted and broadened by Doppler effect,

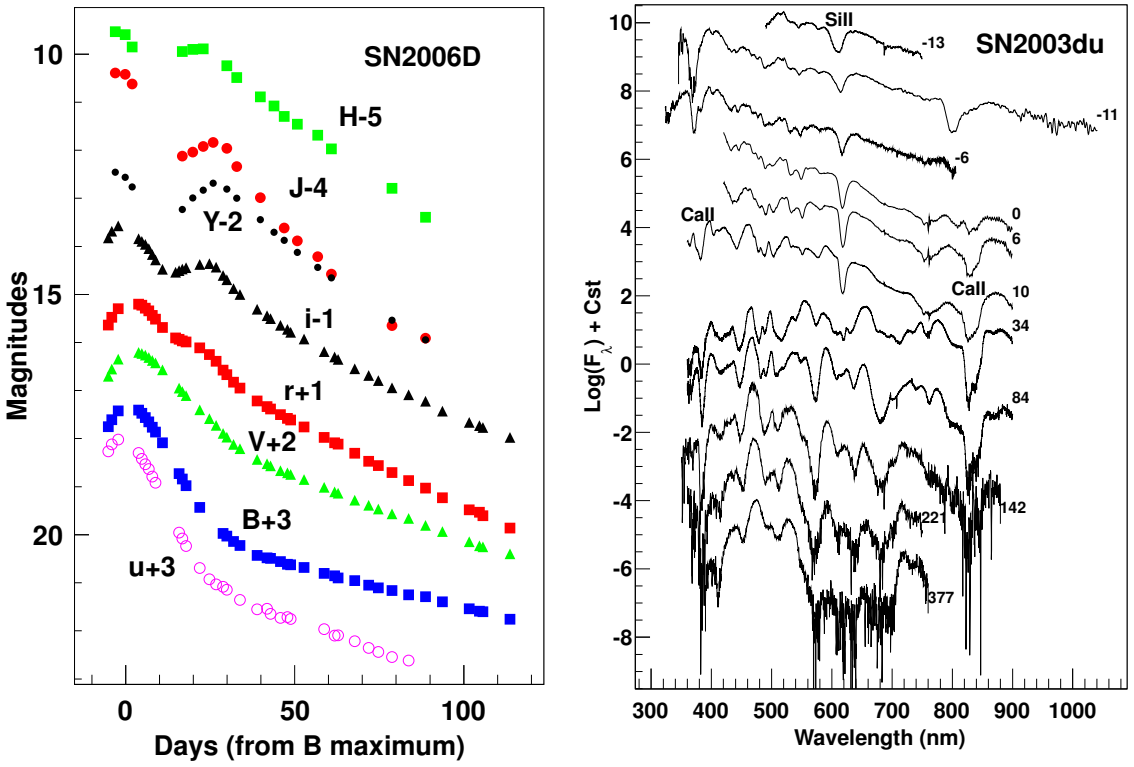

(a) SN Ia light curves

(b) SN Ia spectral sequence

Figure 1.3: Left. Light curves of SN2006D, in the near UV (u), visible (BVr) and the infrared ($iYJH$). Shifts have been applied to each light curve, in order to separate them from each other. Right. Spectral sequence of SN2003du. Note the strong Si II and Ca II features that are typical of SNe Ia.

since the absorbing layers are in rapid expansion towards the observer with typical velocities of $\sim 10,000$ km/s. As the supernova expands, the medium become optically thinner and the photosphere starts to recede towards the inner layers of the object. Around maximum light, spectral features display typical P-cygni shapes, which are the superposition of a strong, blue-shifted, absorption line and the same line re-emitted by the ejecta in expansion, and slightly red-shifted. At that stage, the spectral features are dominated by strong Si II absorption lines (at $4000, 5800$ and 6150 Å), as well as other intermediate mass elements such as Ca II, Mg II and S II. When the photosphere reaches the core of the exploding object, the ejecta are essentially transparent. The spectra are dominated by emission lines from the expanding ejecta. This is the so-called nebular-phase.

1.3.2 SN Ia Physics

The physics of Type Ia supernovae is an active research area. There is no consensus, either on the progenitors or on the physics of the explosion from the ignition to the flame propagation. The minimal model is that SNe Ia should arise from the thermonuclear explosion of a degenerate carbon-oxygen white-dwarf (Hoyle and Fowler, 1960). In a white dwarf, all fusion reactions have stopped. It is the electron degeneracy pressure that supports the star and counterbalances gravitational collapse. If by some mechanism the white dwarf accretes material, the object temperature rises, until the fusion of carbon is triggered, generally close to the Chandrasekhar limit ($\sim 1.38 M_\odot$). At that stage, the star may actually simmer for hundreds to thousands of years, cooled down only by convection. At some point, a larger instability initiates a thermonuclear runaway that disrupts the star in seconds.

Explosion Models The physics of the explosion itself is still uncertain (see e.g. Hillebrandt and Niemeyer, 2000, for a review). If the flame propagates at supersonic speeds (detonation), then mostly iron peak elements (such as ^{56}Ni) will be synthesized, and the abundance of intermediate mass elements will not match those inferred from spectroscopic observations. Subsonic flames (deflagrations), that allow the white dwarf to expand before burning, correctly reproduce the observed abundances of intermediate mass elements, and seem to predict correct peak luminosities. However, they fail to reproduce the observed expansion velocities of intermediate mass elements, and seem to overproduce neutron-rich iron-peak elements.

Delayed detonation models (DDT, Khokhlov, 1991), starting with a subsonic flame which transitions at some point to a supersonic regime are a good match to the observations. Although the transition mechanism remains obscure, recent DDT models seem to predict correct light curve shapes and spectra, and even subtle effects such as the correlations between light-curve shape and luminosity (Kasen et al., 2009). Since detonation is much more efficient at producing ^{56}Ni (hence bright supernovae), it has been suggested that the brighter (resp. dimmer) supernovae may result from a detonation (resp. deflagration) dominated explosion.

Progenitors There is a consensus on the fact that progenitors of SNe Ia involve a carbon-oxygen white dwarf close to Chandrasekhar mass. Since the typical mass of a carbon-oxygen white dwarf does not exceed 1 - 1.2 $M_\odot$, the star needs to accrete matter from a companion. Three classes of models have been proposed so far (see for example the review by Livio, 2000).

In the "single degenerate" scenario (Whelan and Iben, 1973), the white dwarf accretes material from an evolved companion, generally a red giant that fills its Roche lobe. The accreted material, generally hydrogen, is burnt into carbon and oxygen at the surface of the white-dwarf. There are however stringent limits on the accretion rate, which should stay in the range $10^{-8} - 10^{-7} \mathrm{M}_\odot/\mathrm{yr}$. Below, that range, the white dwarf may undergo

repeated nova bursts or helium flashes that would eject more mass than what is accreted. Above that range, both objects may form a common red giant like envelope, and again the white dwarf would loose mass due to drag and winds. This narrow range limits the chances to form a SN Ia from a binary system, and the inferred SN Ia rate from this single degenerate channel is of about 10% of the measured rate. However, the physics of such accreting binary systems is complex, and the arguments presented above may be revised in the future. Recently, Dilday et al. (2012) claimed to have detected multiple shells of circumstellar material around SN Ia `PTF-11kx`. Such a structure could be the result of repeated ancient nova bursts, similar to those encountered by RS Ophiuchi, a red giant-white dwarf system.

An alternative is the so-called "double degenerate" scenario (Iben and Tutukov, 1984). In this model, the progenitor is a system composed of two white dwarfs, decaying by emission of gravitational waves. This scenario is appealing because it may yield the "super-Chandrasekhar" progenitors that can explain very luminous events such as `SNLS-03D3bb`. However, the physics of white dwarf mergers is extremely complicated, and for long, it was not clear that the outcome would be indeed a SN explosion. Quite to the contrary, several authors argued that the less massive white dwarf had every chance to get disrupted in the process forming a hot accretion disk around its companion. Depending on the accretion rate, carbon ignition could then be triggered, turning the companion into a O-Ne-Mg white dwarf (Nomoto and Iben, 1985) which would then collapse into a neutron star (Saio and Nomoto, 1985; Nomoto and Kondo, 1991). Recent work (e.g. Pakmor et al., 2012) shows however that violent white dwarf mergers may trigger a detonation of carbon early enough in the process, yielding a SN Ia explosion. Comparison of such models with observations of the very close and very well studied supernova `2011fe` even shows that they reproduce the observed spectra reasonably well (Röpke et al., 2012).

Finally, in the "sub-Chandrasekhar" scenario (Fink et al., 2007, 2010), or "double detonation scenario" C/O white-dwarfs well under the Chandrasekhar limit may be led to thermonuclear disruption by detonating an outer layer of He. This material may be accumulated from a Helium rich donor, or better, synthesized in-situ by burning the hydrogen accreted from the white dwarf companion. The shock initiates a second detonation propagating from the WD center to the outer layers, disrupting the star. This model has several advantages. First, since the white dwarf is less dense than a Chandrasekhar mass object, the detonation produces intermediate mass elements along with iron peak elements, and no deflagration-to-detonation transition is required. The viability of the model essentially depends on the mass of the helium shell that ignites the supernova. If large ($0.2 M_{\odot}$), the helium layer should be burnt almost entirely into ^{56}Ni, and one should see traces of ^{56}Ni in outer SN layers – hence in the early SN spectra – which is not the case. If a thinner layer is enough to initiate the detonation of carbon, then "sub-Chandrasekhar" models also reproduce qualitatively most observables.

Although significant advances have been made on the subject, SN Ia models are not able to deliver quantitative predictions. Hence, the cosmology studies presented below will rely on empirical models, built from training data sets of very well observed supernovae.

1.3.3 SN Ia Variability

SNe Ia are remarkably uniform for astrophysical objects[5]. They exhibit nevertheless some variability from object to object. In particular, their maximum luminosity in the bluer bands exhibit a dispersion of about 40%. The important point however, is that a significant part of this variability correlates with observables that can be measured easily. Hence, it is possible to build a standardized luminosity distance estimator that is significantly less dispersed.

Brighter-slower relations The correlation between the decline rate of SNe Ia and their intrinsic maximum luminosity — the so-called "brighter-slower relation" — relates the peak luminosity of SNe Ia with how fast their luminosity evolves. Slower events tend to be brighter on average, while fast evolving supernovae are dimmer. This relation was popularized by (Phillips, 1993) building on earlier work by Pskovskii (1984, 1977). It was immediately recognized as an essential property of SNe Ia, permitting to turn them into precise cosmological distance indicators. Typically, the dispersion of SNe Ia luminosities is of about 40% in the blue ($\sim$ 450nm), permitting to measure relative distances with a precision of about 20%. Taking into account the brighter-slower correlation permits to build "standardized" distance estimates with a dispersion of $\sim 7-10\%$ around the Hubble law (e.g. Astier et al., 2006; Perlmutter et al., 1999; Riess et al., 1998; Hamuy et al., 1996a,b).

Brighter-bluer relation Another fundamental correlation is the so-called "brighter-bluer" relation: blue supernovae tend to be brighter than their redder counterparts, even for events with similar light curves. The interpretation of this effect has been a subject of considerable debate. For long, it was customary to attribute the color variability of supernovae to variable amounts of dust along the line of sight (e.g. Perlmutter et al., 1999; Riess et al., 1998, 1996), and to consider that intrinsic SN Ia variability could be parametrized with a unique parameter, (e.g. Δm_{15} or stretch). However, the brightness-color slope derived from SN Ia observations is about a factor two lower than what can be expected from reddening by Milky-Way-like dust (e.g. Astier et al., 2006; Tripp, 1998). This suggests that the brighter-bluer relation is, at least in part, due to some intrinsic

[5] They were noted very soon for their remarkable uniformity, hence the early suggestions to use them as standard candles (e.g. Wilson, 1939; Baade, 1938). (The distinction between Type I and Type II had not been made at that time. However, most supernovae in the samples studied by the authors were very certainly of Type Ia).

color variability of SNe Ia. The community does not seem to have reached a consensus on the subject. Some authors treat the color variability as entirely due to dust absorption and treat the intrinsic variability of SNe using a unique shape parameter. Others prefer to give up separating intrinsic color from dust reddening and treat the brighter bluer relation as a purely empirical relation that can be determined from the data (see e.g. Kessler et al., 2009, for a thorough comparison of both techniques).

Correlations with Host Galaxy Properties The Universe today is significantly different from what it was at $z \sim 1$. Star formation has decreased by a factor 8 and the mix between old, evolved, heavy elliptical galaxies, and younger star forming galaxies has changed significantly. If the intrinsic luminosity of SNe Ia correlate with their environment, then one may expect that the average SN properties could change as a function of redshift. Redshift-dependent effects are the worst nightmare of supernova cosmologists. If not mapped and accounted for, they may bias severely the cosmological measurements.

The first hint for an environmental dependency comes from the SN Ia rates. SNe Ia occur about 10 times more frequently in active, star forming galaxies than in evolved, passive galaxies. (e.g. Sullivan et al., 2006). Mannucci et al. (2005) suggested that there could be two different SN Ia populations, namely "prompt" and "delayed" SNe Ia with different progenitors, hence different properties. This is not demonstrated yet, as the O(1000) SN Ia samples available today are too small to constrain the distribution of the time delay between a star burst and subsequent SN Ia explosions.

Also, it has been known for a long time that late type (star forming) galaxies host supernovae that are on average brighter than those that occur in early type (passive, of higher metallicity) galaxies (Hamuy et al., 1996b). Since galaxy population evolves with redshift, one can expect that distant supernovae are, on average, brighter than their nearby counterparts. This has been detected indeed, for example in the SNLS sample: Howell et al. (2007) report a 12 % increase of the average SN luminosity over the $0.03 \lesssim z \lesssim 1.12$ redshift range. However, the same study also shows that this effect is properly corrected for, by the brighter-bluer and brighter-slower relations. Therefore, it has no impact on the average standardized distances to SNe Ia, hence no impact on the cosmological results.

The first detection of a dependency to the environment, not accounted for by the standardization relations, was reported by Sullivan et al. (2010); Lampeitl et al. (2010); Kelly et al. (2010) on recent large supernova samples. They show that *after standardization*, SNe Ia are on average $\sim 10\%$ brighter is massive (passive, high metallicity) galaxies than in less massive (star forming) hosts. The signal is still weak, and several hundreds of well measured supernovae are needed to obtain a 4σ significance on the instrinsic luminosity difference. However, the value of w is sensitive to this brightness difference at the level of $\sim 0.04 - 0.08$.

As a conclusion, one needs at least three parameters to parametrize the diversity of SN Ia: a lightcurve shape parameter (such as a stretch), a restframe color and an observable that correlates with the mass (or metallicity) of the SN host galaxy. This imposes strong constraints on the supernova survey designs, in particular on the quality of the photometric observations.

1.4 Building Hubble Diagrams with SNe Ia

We now present the main steps in building a Hubble diagram. Our goal is not to review in detail the various techniques used by different groups. It is rather to discuss the essential steps, and show where the main systematics enter the measurement.

1.4.1 Observations

Broadband Observations To detect and follow-up supernovae, we rely on broadband photometric measurements, performed in the visible and the infrared with modern wide-field imagers. Broadband filters typically include the standard UBVRI filter set (Bessell, 1990) or the more recent SDSS filters (Fukugita et al., 1996). They cover the 300 nm $<$ λ $<$ 1100 nm range, with $\sim 1000 - 1500$ Å-wide filters placed every $\sim$ 1300 Å (figure 1.4). This is a rather coarse sampling, but this is the price to pay if we want to obtain decent signal-to-noise ratios for $z \sim 1$ SNe Ia with exposure times of $\sim$ 40 minutes on 4-meter telescopes.

In the visible, the detectors are silicon CCDs. Modern chips have a quantum efficiency of about 90%, from the blue ($\sim$ 450 nm) to the near-infrared ($\sim$ 950 nm), and display an excellent linearity over nearly five orders of magnitudes. They are also buttable, allowing to build large composite focal planes, comprising dozens of chips (10^8 to 10^9 pixels) (e.g. Boulade et al., 2003). The size of the supernova samples closely follows the field of view of the imagers that are used to detect them. Clearly, the advent of large focal planes, along with the computing power able to process the huge data-set they deliver are the two key technologies that revolutionized the field. Today, modern wide field imagers (e.g. DECam, Honscheid et al., 2008) are able to cover several square degrees of sky, making it possible to scan volumes large enough to discover thousands of supernovae in a few years.

The band-gap energy of Silicon is of about 1.15 eV, corresponding to wavelengths of $\sim$ 1.1 µm. Hence, CCDs cannot detect light redder than this natural cutoff. Infrared observations are performed with lower band gap sensors, such as HgCdTe devices (Rieke, 2007). The standard passbands which equip infrared imagers are presented on figure (1.4). At those wavelengths the atmospheric transmission presents numerous absorption lines, and filters are designed to take advantage of the rare clear windows. Another difficulty comes from the very high and variable background sky levels, due to atmospheric glow, which increases as a function of wavelength. Both problems are not present when

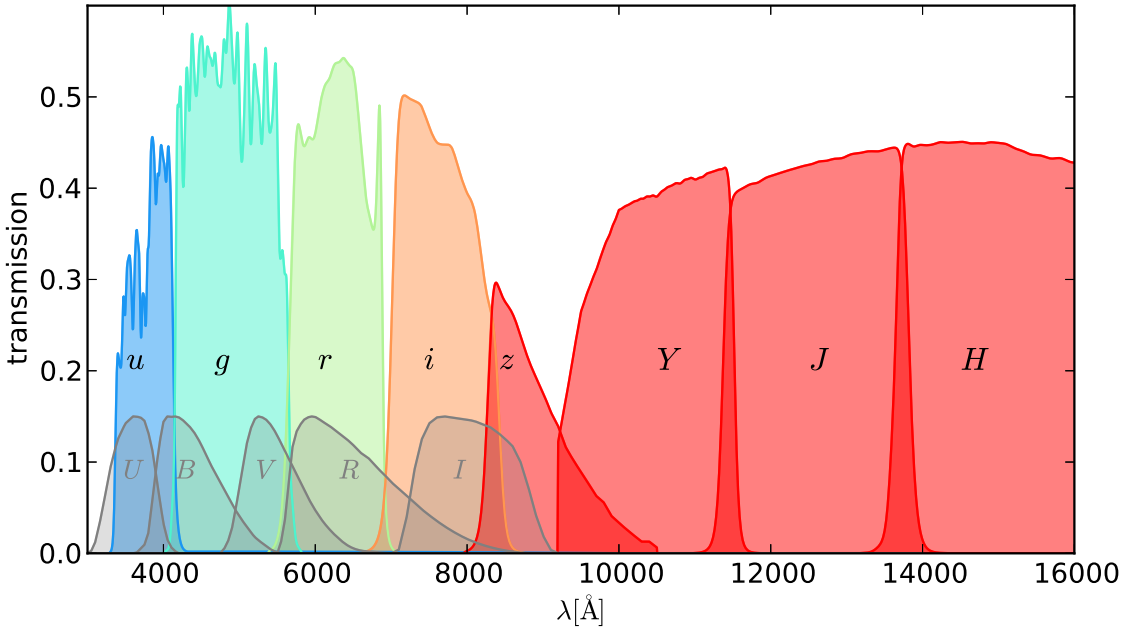

Figure 1.4: Standard passbands in the visible and infrared. We show the standard *ugriz* passbands that equip MegaCam and the IR filters proposed for the space mission Euclid. Note that the H band extends further in the IR, up to 25000Å. As shown of the figure, the transmission of modern imagers is of about 50%. The historical $UBVRI$ filters are also drawn (arbitrary normalization). About one third of the SN sample (mostly nearby supernovae) are measured in this filter system.

observing from space, hence the efforts to place wide field infrared focal planes in orbit for cosmological measurements (see e.g. Euclid (Amendola et al., 2012) and WFIRST (Green et al., 2012)).

Magnitudes and Colors Telescopes are generally not designed to measure absolute fluxes. With care, it is nevertheless possible to measure *relative fluxes* with an excellent precision, from $\sim 0.1\%$ for ground-based observations to almost $\sim 0.01\%$ in space. For this reason, broadband observations are generally reported as magnitudes, which are intrinsically flux ratios. An astronomical imager measures fluxes in *instrumental units*, typically ADC counts per second (ADU/s). The magnitude of an astronomical object is defined as:

$$m = -2.5 \times \log_{10}\left(\frac{\phi_{\mathrm{ADU}}}{\phi_{\mathrm{ADU}}^{\mathrm{ref}}}\right) \tag{1.14}$$

where ϕ_{ADU} is the object's flux, and $\phi_{\mathrm{ADU}}^{\mathrm{ref}}$ is the flux of a conventional reference, observed in similar conditions.

A color is the difference between magnitudes of a same object, in different passbands — e.g. $g-r$, or $B-V$. Again, it is the logarithm of a flux ratio. It is related to the local slope of the object's spectrum, hence, to the object's temperature.

Spectra To identify Type Ia supernovae and measure their redshift, one relies on spectroscopic observations. Characterizing a Type Ia supernova requires moderate resolution spectra ($R = \lambda/\delta\lambda \sim 500 - 1000$) and signal to noise ratios of ~ 1 per 5 Å wavelength bin in the $4000 < \lambda < 8000$ rest-frame region. For a $z \sim 1$ SN Ia, this can be attained with ~ 1 hours of integration, on a 8-m telescope. This is a very significant amount of time, and spectroscopy is today a serious bottleneck for increasing the size of SN Ia samples. As an example, SNLS required about 1200 hours of dark time on 8-m telescopes to identify about 450 supernovae. This represents much more observing time than what was needed to discover and follow up the same SNe Ia[6] (1200 hours, but on a 4-m class telescope only). As a consequence, future surveys will not be able to obtain spectra for more than a small fraction of their discoveries. Hence the efforts currently invested into SN Ia photometric identification techniques relying on broadband flux measurements only (e.g. Kessler et al., 2010, and references therein).

If SN typing is problematic, it is likely that spectroscopic redshifts can be obtained for all supernovae, even with large O(10000) samples. Indeed, redshifts are determined from the spectral features of the SN host galaxy. The observations can therefore be performed later, when the supernova has faded (Lidman et al., 2012). Therefore, the spectroscopic observations may be spread over several years, lifting the pressure on the 8-m class telescopes. Moreover, large numbers of spectra can now be acquired in parallel, using multi-object spectroscopy. Up to recently, most spectrographs could only observe one object at a time, by placing one single slit at the position of the source. The slit is followed by a grating that disperses the light in a direction orthogonal to it. This is extremely inefficient, as the slit size is much smaller than the telescope field of view. Recent multi-object spectrographs (MOS) allow to observe $10^2 - 10^3$ objects simultaneously, by placing multiple fibers into the focal plane, each fiber feeding the spectrograph — AAOmega (Sharp et al., 2006) or the SDSS spectrograph (Newman et al., 2004) and its recent upgrades (Smee et al., 2012) are a few examples of very successful instruments.

1.4.2 Distance Estimates and Cosmological Constraints

The measurement principle is summarized on figure (1.5). We have SNe Ia at various redshifts, and we want to measure their *rest-frame* flux from the magnitudes measured in the observer frame pass-bands (shown as vertical shaded areas on the figure). Given

[6] plus ~ 500 others that could not be observed spectroscopically.

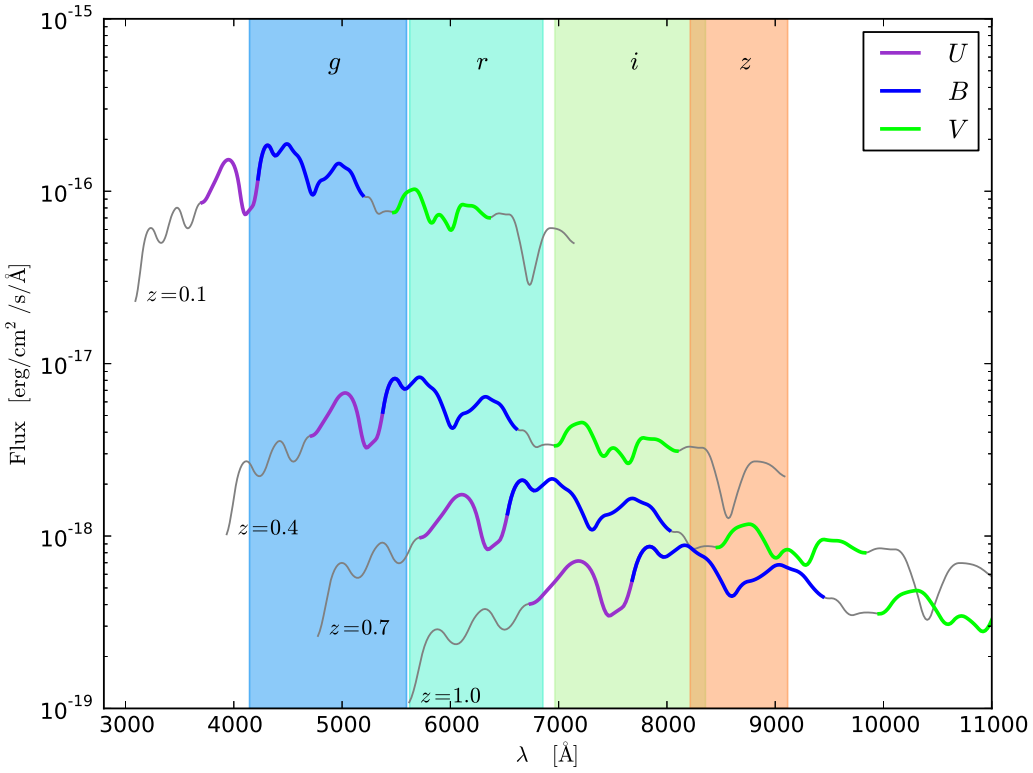

Figure 1.5: SN Ia spectra at various redshifts. The shaded areas represent the imager (observer frame) passbands. The distance estimate is generally chosen as the integral of the SN spectrum in the restframe B-band (blue thick line on the spectra). As we go further in redshift, the SN spectra are redshifted and the B-restframe flux is sensed by different observer-frame bands.

the importance of the brighter-bluer relation, we anticipate that we will have to measure a rest-frame color as well.

The supernova flux is generally defined as the integral of the SN spectrum in some conventional rest-frame pass-band, generally the B-band. This has several advantages. First, this is were the SN Ia luminosity is highest. Second, as we go further in distance, the redshifted SN B-band flux falls in observer frame bands that are redder and redder but still in the visible. Hence, no infrared observations are required up to $z \sim 0.9$, thereby avoiding systematics from the intercalibration of two (very different) imagers.

It is apparent from figure (1.5) above, that SN Ia restframe magnitudes and colors cannot be directly derived from the observations. Instead, they must be inferred from the SN light curves using a spectrophotometric model. Several such SN Ia models have been built and described, in particular MLCS2k2 (Jha et al., 2007), SALT2 (Guy et al., 2007), SiFTO (Conley et al., 2008) to cite a few. All are fully empirical, and trained on

samples of well observed supernovae. MLCS2k2 is trained on a nearby SN sample, while SALT2 and SiFTO both use nearby and distant supernovae, including the SNe Ia that are used to constrain the cosmology. This is perfectly acceptable, as the SN rest frame flux is not used in the training (only the colors are).

It is easy to show from equations (1.12) and (1.13) that the magnitude of the supernova in the restframe B-band ($m_B^\star$) can be written as:

$$m_B^\star = M_B + 5\log_{10}\left(\frac{c}{H_0 \times 10^{-5}\mathrm{Mpc}}\right) + 5\log_{10}\left(\mathcal{D}_L(z;\boldsymbol{\theta})\right) \tag{1.15}$$

where M_B is the B-band absolute magnitude of the supernova, i.e. its apparent magnitude at a distance of 10 parsecs (or 10^{-5} megaparsecs): $M = -2.5\log_{10}\mathcal{L}/4\pi(10pc)^2$. $\mathcal{D}_L(z;\boldsymbol{\theta})$ is the c/H_0 reduced luminosity distance. It depends on the cosmological parameters, e.g. $\boldsymbol{\theta} = (\Omega_m, \Omega_X, w\ldots)$. Since M_B and H_0 are fully degenerate, one generally choose to absorb them into a single parameter: $\mathcal{M}_B = M + 5\log_{10}(c/H_0) + 25$, which is unknown a priori, and has to be determined along with the cosmological parameters. The equation above can then be rewritten as:

$$\mu \equiv m_B^\star - \mathcal{M}_B = 5\log_{10}\left(\mathcal{D}_L(z;\boldsymbol{\theta})\right) \tag{1.16}$$

Hence, constraining cosmological parameters from a Hubble diagram consists in measuring *distance moduli* from the light curves of SNe Ia spread over a (large) redshift range, $\mu = m_B^\star - \mathcal{M}_B$ and in comparing these measurements with the predictions of a cosmological model: $\mu(z) = 5\log_{10}\mathcal{D}_L(z;\boldsymbol{\theta})$. This comparison is performed by minimizing the following χ^2:

$$\chi^2(\boldsymbol{\theta}, \mathcal{M}_B) = \sum_{i\in\mathrm{SNe}} \frac{(\mu_i - \mu(z_i,\boldsymbol{\theta}))^2}{\sigma_{\mathrm{stat}}^2 + \sigma_{\mathrm{int}}^2} \tag{1.17}$$

In the equation above, σ_{stat} is the statistical uncertainties that affect the supernova measurements, while σ_{int} accounts for the dispersion from supernova to supernova. $\mathcal{M}_B$ which is unknown, is treated as a nuisance parameter: it is fitted along with the cosmology and then marginalized over.

Standardized distance estimates SNe Ia B-band luminosities exhibit a dispersion of about 40%. As discussed above, this dispersion may be reduced by taking advantage of the brighter-bluer and brighter-slower relations. A common approach consists in defining a "standadized distance modulus" as:

$$\mu = m_B^\star - \mathcal{M}_B + \alpha\,\mathcal{X} - \beta\,\mathcal{C} \tag{1.18}$$

where $\mathcal{X}$ is a parameter that accounts for the supernova lightcurve width (it can be for example a stretch parameter as in Perlmutter et al. (1999), or the X_1 parameter of Guy et al. (2007)) and $\mathcal{C}$ is a restframe color of the supernova (e.g. $B-V$). Generally,

one considers that α and β are not known. They are treated as additional nuisance parameters, exactly as $\mathcal{M}_B$.

There is no real consensus yet on how to build optimal distances from supernova light-curves. Many authors use the "brighter-bluer" and "brighter-slower" standardization relations as shown above. However, their is still debate on how to interpret the SN color information, e.g. whether the brighter-bluer relation is entirely due to absorption by dust (which fixes the value of β), or whether it incorporates some amount of color variability intrinsic to supernovae (see e.g. Guy et al., 2010; Kessler et al., 2009, for in-depth discussions on the subject). Alternate standardization techniques have been explored, relying on selected spectral features (Bailey et al., 2009) or on the trajectory of SNe Ia in a rest-frame color-magnitude diagram, Wang et al. (2003); Conley et al. (2006) but their use in practice is limited by the amount of additional data they require.

Taking the Host Galaxies into Account With the recent discovery that the Hubble residuals (after standardization) are correlated with host galaxy stellar masses, it appeared necessary to modify the definition of standardized distance moduli (e.g. Suzuki et al. (2012); Sullivan et al. (2011, 2010) and (§1.3.3)). Given the size of the current samples, what has been done so far is to segregate SN Ia into two groups ($M_{\rm stellar} < 10^{10} M_\odot$) and ($M_{\rm stellar} > 10^{10} M_\odot$) and to fit different $\mathcal{M}_B$ parameters for each group. Accounting or not for the host galaxy mass does have a sizeable effect on the value of w. This is not surprising given that the number of low-mass, star-forming galaxies is significantly higher in the early Universe than today. Sullivan et al. (2011) finds $\Delta w \simeq 0.06$, comparable to the total systematic uncertainties on w. With more data, it is will be probably possible (and necessary) to fit different standardization relations for each group. As an example, Sullivan et al. (2011) finds weak evidence that β may differ according to the host galaxy mass.

1.5 Recent and Future Supernova Surveys

1.5.1 The Pioneers

The initiators of the Calán/Tololo Supernova Survey (Hamuy et al., 1993) are indisputably the pioneers in the field. The project was able to find and follow-up about 30 nearby Type Ia supernovae, a tour de force at that time. The high-quality of the photometric follow-up, performed with one of the first cryogenic astronomical CCD cameras, permitted detailed studies of the supernova light curves. In particular, they confirmed the Phillips (1993) relation, and were the first to use it on a large scale to measure luminosity distances precise at the 7-10% level (Hamuy et al., 1996a, 1995).

The Supernova Cosmology Project (SCP) and the High-Z Team (HZT) struggled for almost a decade to discover and follow up a few dozen SNe Ia at redshifts $z \sim 0.5$. Both teams published the analysis of their full samples at about the same time (Perlmutter

et al., 1999; Riess et al., 1998). Both measurements relied on the same nearby events, all drawn from the Calán-Tololo sample, but had distinct sets of distant supernovae. Both teams also made use of the brighter-slower standardization relation. However, the poor quality of the photometric follow-up barred them from determining accurate SN colors. Both analysis find strong evidence for a non-zero cosmological constant and place the first constraints on the Dark Energy Equation of State (assuming a flat Universe).

1.5.2 Second Generation Surveys

At that point, two strategies could be explored to improve the results. The SCP and HZT choose to take advantage of their privileged access to the Hubble Space Telescope to discover more distant SNe Ia and extend the redshift lever arm. The SCP first published a second measurement, using a new distant SN Ia sample, observed with HST (Knop et al., 2003). They later launched the ambitious "SCP Cluster Search" (e.g. Suzuki et al., 2012, and references therein). At the same time, the HZT team carried out the very successful GOODS program (Riess et al., 2007, 2004), that notably discovered the most distant SNe Ia ever found.

An alternative was to build larger SN Ia samples, of much higher quality, at intermediate redshifts. In particular, it was clear that obtaining accurate color measurements for each SN was key to improve the distance estimates. Hence, second generation supernova surveys started gathering the large supernova samples that were necessary to confirm the initial results, and measure w with a precision of $\sim 10\%$. The Supernova Legacy Survey[7] (SNLS, Sullivan et al., 2011; Astier et al., 2006) has detected and followed-up, between 2003 and 2008, about 450 SNe Ia in the redshift range $0.3 < z < 1$. The Sloan Digital Sky Survey[8] (SDSS-II, Kessler et al., 2009; Holtzman et al., 2008) has accumulated a sample of similar size and quality at lower redshift ($0.1 < z < 0.3$). Finally, several low-redshift projects, such as the CfA supernova search[9] (Hicken et al., 2012; Blondin et al., 2012), the Carnegie Supernova Project[10] (Stritzinger et al., 2011; Folatelli et al., 2010) or the Berkeley Supernova Program (Silverman et al., 2012) have increased very significantly the nearby supernova dataset.

Current Constraints on w Today, about 1000 well-sampled, spectroscopically identified, SNe Ia can be used to constrain the distance-redshift relation. For example, figure 1.6 shows the Hubble diagram published recently by the SNLS survey (Conley et al., 2011). It contains 472 well-observed SNe Ia: 123 at low-redshift, 93 at intermediate-redshift, from the SDSS first year sample, 242 SNLS events, and 14 high-redshift HST supernovae.

[7] http://cfht.hawaii.edu/SNLS/
[8] http://www.sdss.org/supernova/aboutsprnova.html
[9] http://www.cfa.harvard.edu/supernova/
[10] http://csp1.lco.cl/~cspuser1/PUB/CSP.html

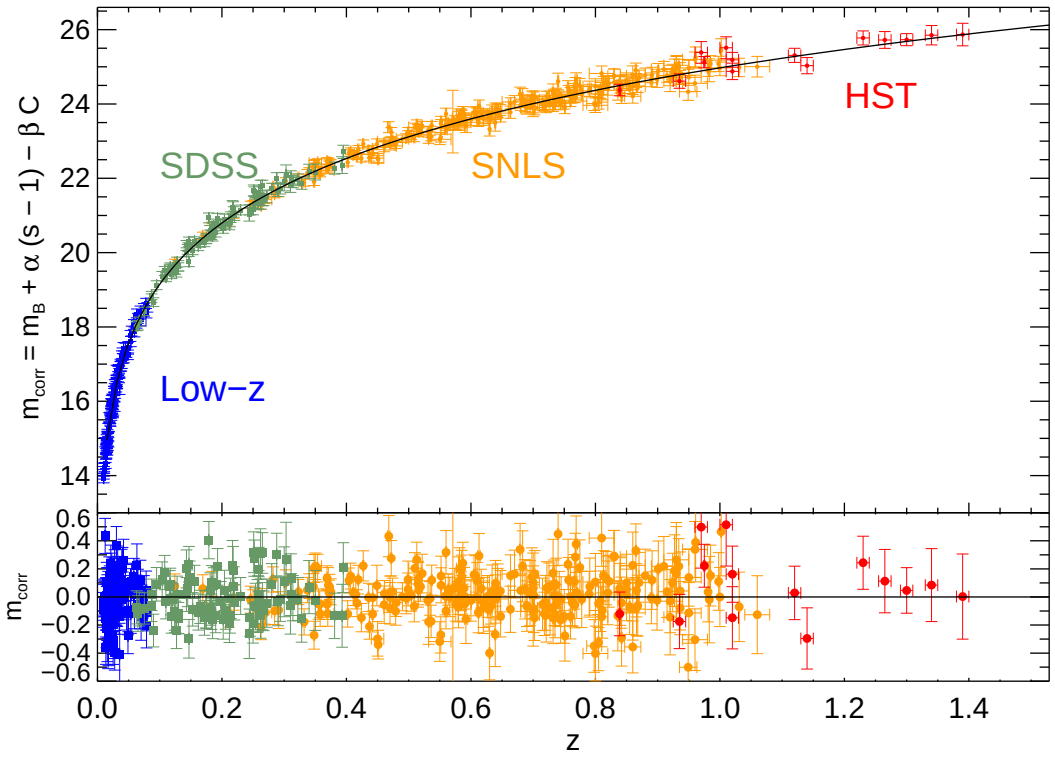

Figure 1.6: SNLS 3-year Hubble diagram (Conley et al., 2011). The bottom panel shows the residuals from the best fit.

The corresponding constraints obtained on w are shown on figures (1.7) and (1.8). Figure (1.7) shows the contours in the $\Omega_m - w$ plane, assuming a flat Universe. As discussed above, supernovae alone yield one single constraint — hence, elongated contours. This quasi-degeneracy can be broken by combining the SN measurements with other probes, e.g. the results from recent BAO and CMB experiments (green contours on figure (1.7). Figure (1.8) shows the contours obtained when relaxing the assumptions on flatness. Supernovae bring significant amounts of information in the combined measurements. In particular, they are essential to constraint the value of w.

For a flat Universe, and a constant equation of state, SNLS 3-year reports: $w = -1.068 \pm 0.08$ (stat + sys) — after folding in the BAO and CMB constraints. If allowing for a variable equation of state, $w(z) = w_0 + w_a z/(1+z)$, one finds $w_a = -0.98 \pm 1.1$, compatible with 0. Hence, today's measurement are compatible with a cosmological constant. However, they are not precise enough to rule out most alternative Dark Energy models.

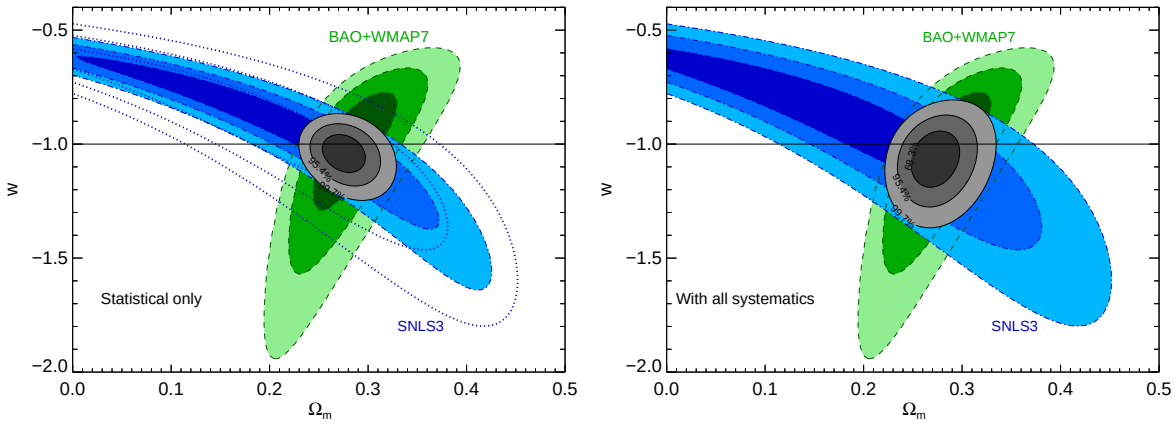

(a) Statistical uncertainties only

(b) With Systematics

Figure 1.7: Confidence contours in the $\Omega_m - w$ plane, assuming a flat Universe and a constant w. The SNLS constraints are shown in blue. The BAO + WMAP7 constraints (Komatsu et al., 2011; Percival et al., 2010) are represented in green. The systematics represent slightly more than half of the total error budget. They are essentially due to photometric calibration.

1.5.3 Future Projects

The efforts towards understanding the nature of dark energy have been reviewed in detail by two committees, the Dark Energy Task Force (DETF) (Albrecht et al., 2006) and the ESA-ESO Working Group on "Fundamental Cosmology" (Peacock et al., 2006). Both panels note that future progress on the subject depends on the ability of surveys to control their systematics. They strongly suggest a multi-probe approach, combining mature proven probes, such as SNe Ia with emerging probes, such as weak-lensing and baryon acoustic oscillations. The DETF defines a metric, to evaluate the impact of each experiment on dark energy. It is called the "DETF Figure of Merit" (FoM) and defined as the inverse of the ellipse area in the plane $w_0 - w_a$. It is used to rank the various proposals in "generations" or "stages" according to their expected performances.

As an example, second generation supernova surveys such as SNLS have reached a FoM of ~ 10. Future third generation surveys such as the Dark Energy Survey (DES) PanSTARRS, SuMIRe (Suto, 2010; Gunn et al., 2012) or BOSS (Anderson et al., 2012; Dawson et al., 2012) should reach a FoM of ~ 30 once combined with the results of Planck. Finally, the goal of fourth generation surveys such as LSST (LSST DESC, 2012), Euclid (Amendola et al., 2012) or WFIRST (Green et al., 2012) should be able to reach a FoM of about 100.

Among the stage-III projects, the Dark Energy Survey is primarily a weak lensing survey, with the objective to cover about 5000 deg^2 of the southern Galactic cap. It has

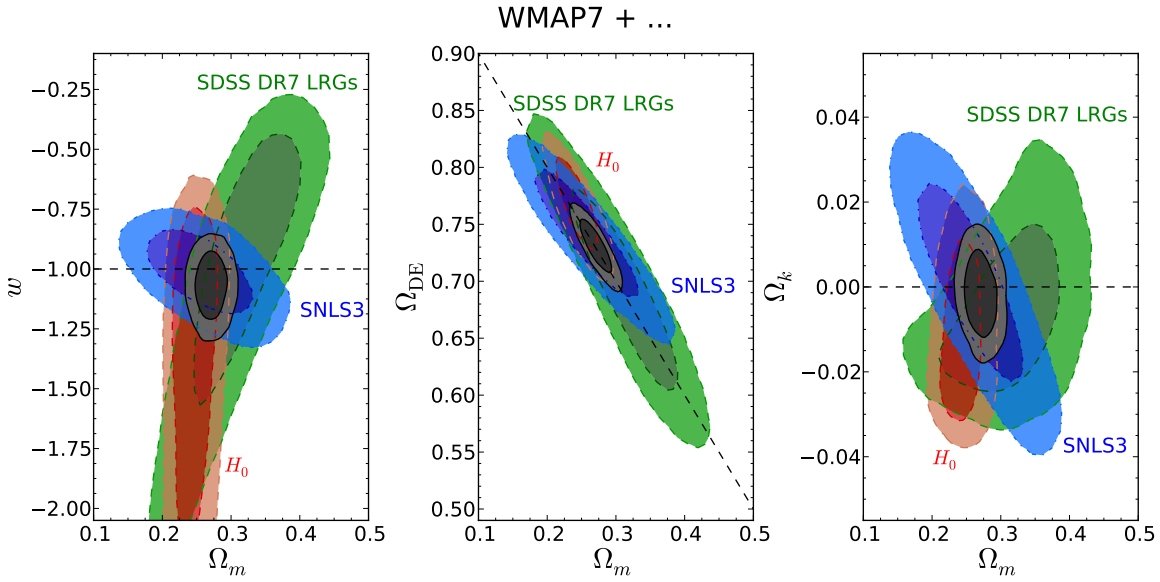

Figure 1.8: Contours in the (Ω_m, w), (Ω_m, Ω_X) and (Ω_m, Ω_k) planes, relaxing the assumptions on flatness. As can be seen on the leftmost panel, the contribution of supernovae is essential to constraint w.

also a very interesting supernova component, designed to detect about 4000 SNe Ia in the redshift range $0.05 < z < 1.2$ (Bernstein et al., 2012). The DES 3 deg^2 DECam imager is equipped with thick high-resistivity CCDs sensitive in the red, allowing to obtain precise flux measurements in the near-infrared, hence, to measure supernovae at higher redshifts. The large SN sample will allow to refine the empirical supernova models used to fit the light curves, and derive the SN rest frame fluxes. The expected precision of DES on w is of about 0.05 (stat + sys), about twice better that what SNLS has delivered. A significant part of this expected improvement comes from improvements of other probes, however.

Stage-IV projects are all planned for 2020 and later. It is relatively difficult to make projections that far in the future. LSST has a supernova program although not well defined yet. In short, it as been suggested that LSST should build O(10000) SN samples with an exquisite follow-up in the visible and the near-infrared, and covering the full $0.01 \lesssim z \lesssim 1$ redshift range, thus avoiding intercalibration between different telescopes. Euclid is primarily a weak-lensing and BAO survey. However, there is an obvious complementarity LSST, which can discover and observe supernovae in the redshift range at $z \lesssim 1$ and Euclid which can follow-up in the infrared a smaller sample of SNe Ia at redshifts well beyond 1. Such options are currently under study within the two collaborations. Current studies indicate that it should be possible to obtain a precision of $\sim 2\%$ on w (with Planck priors).

1.6 Systematics

Recent measurements of w with SNe Ia are dominated by systematics, which account for a little more than half of the total uncertainty (see e.g. both panels of figure 1.7) and table 7 of Conley et al. (2011). Identified systematics include notably:

- photometric calibration, which turned out to be the largest contribution to the total uncertainty budget. The reason why photometric calibration plays such a large role is discussed in (§1.6.2) below.

- statistical uncertainties carried by the empirical lightcurve models such as SALT2 or SiFTO. Indeed, since these models are trained on supernova samples of finite size, they are slightly uncertain. This kind of uncertainties is sometimes mentioned among the systematics. However, it is statistical in nature, and is expected to improve as the size and the quality of the training samples grow.

- uncertainties due to the various assumptions made within the light curve fitters. This contribution can be estimated by comparing the same analysis, performed with two different fitters (SALT2 and SiFTO, see Guy et al. (2010)).

- uncertainties related to the completeness of the SN samples. As one goes further in distance, one gets closer to the survey detection limit, and one starts selecting preferentially brighter (and bluer, slower events). This induces a selection bias, that has to be modeled and corrected for using a simulation of the survey (e.g. Perrett et al., 2012).

- systematics of astrophysical origin, such a the correlations of SN properties with their host stellar mass.

The situation on the front of systematics is therefore quite encouraging. The main contributions have either an instrumental origin (photometric calibration) or will necessarily decrease in the future with larger supernova samples (e.g. empirical modeling of SNe Ia). Hence, it is clear that the supernova constraints are going to improve in a near future. Even if first hints of systematics of astrophysical origins have been spotted, it is difficult to predict when SN Ia results will be outperformed by other cosmological probes, more immune to astrophysical uncertainties (e.g. baryon acoustic oscillations).

1.6.1 Accounting for the systematics

Now that they have such a large impact on the measurement uncertainties, the treatment of systematics is more sophisticated than it was ten years ago. In particular, it turned out that it was essential to track and propagate the correlations introduced by the presence of systematics common to all supernovae. A good example are the calibration uncertainties.

If one looks at figure (1.5) it is apparent that a calibration uncertainty on a given band (e.g. r) will affect all supernovae in a given redshift range (e.g. $0.35 \lesssim z \lesssim 0.55$).

Several techniques can be used to propagate such systematics. The technique adopted by SNLS is described in detail in (Conley et al., 2011). It consists in computing explicitly the covariance matrix of the SN distance moduli (including the off-diagonal elements). This covariance matrix is then used in the cosmological fit. We give a brief account of the method below.

Let's rewrite the χ^2 in matrix form:

$$\chi^2(\boldsymbol{\theta}, \mathcal{M}, \alpha, \beta) = \boldsymbol{\Delta\mu}^T \mathbf{C}^{-1} \boldsymbol{\Delta\mu} \tag{1.19}$$

$\boldsymbol{\Delta\mu}$ is the vector of model residuals over the SN sample and $\mathbf{C}$ is the covariance matrix. It is not diagonal. can be decomposed into the sum of several contributions:

$$\mathbf{C} = \mathbf{C}_{\text{stat}} + \mathbf{C}_{\text{sys}} \tag{1.20}$$

where $\mathbf{C}_{\text{stat}}$ accounts for the statistical uncertainties (those which decrease with the number of supernovae, N_{SN}) while $\mathbf{C}_{\text{sys}}$ tracks the systematics (those uncertainties that do not decrease with N_{SN}, e.g. calibration). The elements of $\mathbf{C}_{\text{sys}}$ can be easily determined provided that we know the derivatives of the SN parameters ($m_B^\star$, $\mathcal{X}$, $\mathcal{C}$ quantities) as a function of the systematic uncertainties ΔS_k. These derivatives can be computed by brute force. For example, to compute the sensitivity of the ($m_B^\star$, $\mathcal{X}$ and $\mathcal{C}$) to, say, the calibration in the r band, one (1) alters the $r-band$ data (2) retrain the light curve fitter on the altered light curves (3) refit all the (altered) SNe Ia light curves with the retrained fitter. This is computationnaly intensive, however, it is the exact way to account for all the subtle correlations introduced by the systematics.

1.6.2 Why is Photometric Calibration So Important ?

The reason why photometric calibration has such a large impact for current measurements should be fully apparent from figure 1.5. For nearby supernovae, the restframe B- and V-bands match approximately the telescope g- and r-bands respectively. As we go further in redshift, B and V will match successively r & i ($z \sim 0.4$) and then i & z ($z \sim 0.7$). The nearby and distant SNe are therefore not observed with the same filters. In particular, the distance to the low-z (resp. high-z) SNe Ia are estimated from observations performed with g and r (resp. i and z). As a consequence, the cosmological measurements actually boil down to comparing fluxes measured in the blue and red passbands of the imagers. Hence, any wavelength-dependent calibration error will translate into a redshift-dependent systematics, biasing the cosmological results.

There is a second source of bias also related to photometric calibration. To understand it, let's go back to figure 1.5. Above $z \sim 0.7$, the restframe V-band light of the distant SN cannot be measured with an imager operating in the visible. Hence, most modern

surveys are in a situation where the SN distances are estimated with the restframe B and V bands up to a given redshift (typically $z \sim 0.6$ for SNLS), and progressively with the restframe U and B bands beyond that redshift.

As mentioned in §1.4.2, the estimation of the restframe fluxes relies on an empirical spectrophotometric model, trained using spectra and light curves of well observed supernovae. Relative flux calibration of spectra is not as reliable as photometry, hence, the flux calibration of the empirical SN model relies on the photometry of the supernova. Again, a wavelength-dependent calibration bias of the data will translate into a wavelength-dependent calibration bias affecting the spectrophotometric model. This in turn will generate a redshift-dependant bias affecting the SN distances.

As a conclusion, the performances of future supernova surveys depend on our ability to improve the flux intercalibration of the passbands. The worst case would be correlated (i.e. wavelength dependent) calibration errors. In the next chapter, the review the status of the traditional calibration approach, relying on repeated observations of standard stars.

2 Stellar Calibration

What is meant by "photometric calibration" actually depends on the science that drives the observations. Searches for variable stars, microlensing events or exoplanets will focus on instrument stability and measurement repeatability. As an example, detecting earth size exoplanets by transit requires relative photometry precise at a few 10^{-5}. In other cases, it is the survey uniformity that matters. An example is the study of the Galaxy structure using the photometric properties of different stellar populations, or the study of the clustering properties of matter in the Universe. Both analyses require uniformities of 1-2% over thousands of square degrees. Supernova cosmology for its part, mainly relies on our ability to secure a precise flux calibration of the survey: we need to convert broadband supernova flux measurements (in ADU/s) into units that are homogeneous to physical irradiances (ergs/cm^2/s). As discussed in the previous chapter, the cosmological measurements are insensitive to the absolute flux scale; what matters instead is the *relative* calibration of all passbands.

To anchor photometric observations on a given flux scale, one usually relies on observations of *primary standards*, i.e. stable spectrophotometric standard stars, with a spectral energy distribution (SED) that is known in physical units. Establishing the absolute SED of an astrophysical object is notoriously difficult. The astronomical community has long relied on Vega, whose absolute flux had been characterized using laboratory sources. New sets of calibrators have since emerged, calibrated using *models* of hot white dwarf stellar atmospheres (§2.2). The other fundamental problem of calibration is then to build a robust metrology chain, from the primary standard observations to the survey science images (§2.3). This involves controlling many observational aspects which are discussed in §2.4.

2.1 Flux Calibration

Measurement Model If one observes an object of known SED, $\mathcal{S}(\lambda)$, with a broadband instrument of transmission $T(\lambda)$, the flux measured is given by:

$$\phi_{\rm ADU} = A \times \int \mathcal{S}(\lambda) \frac{\lambda}{hc} T(\lambda) d\lambda \tag{2.1}$$

where A is the total collecting area of the telescope (in cm^2). The object SED, $\mathcal{S}(\lambda)$, is a spectral radiance, and has dimensions of energy per unit area and unit wavelength. The transmission is usually expressed in counts in the detector per incoming photon, hence

the λ/hc factor. The telescope converts the spectral radiance $\mathcal{S}(\lambda)$ that hits the primary mirror into a broadband instrumental flux, expressed in detector counts per second.

Instrument Transmission The instrument throughput, $T(\lambda)$ is the product of many terms, including notably (1) the transmission of the atmosphere (2) the transmission of the optics (3) the quantum efficiency or the sensors and (4) the gains of the electronics. The shape of $T(\lambda)$, in particular the position of the filter fronts is generally obtained from test bench measurements of the different optical components, prior to installation. To account for the effect of atmospheric transmission (Raleigh scattering in the blue, O_2, O_3 and H_20 absorption in the redder bands) one usually uses an average model determined with spectroscopic observations, such as Buton et al. (2012).

The shape of $T(\lambda)$ is not expected to vary over the course of the instrument life (see although the results of Doi et al. (2010) for the SDSS survey). On the other hand, its normalization, i.e. the total throughput of the system, is not known with precision at every time. Some of its constituents such as the reflectivity of the mirror or the CCD quantum efficiency may degrade slowly over time. Also, the transmission of the atmosphere varies significantly over short time scales. As a consequence, a telescope cannot measure precisely absolute fluxes.

Natural magnitudes What a telescope can measure precisely however is the flux of a science object relative to the flux of a standard star, observed shortly before or after the science observations, in similar conditions of airmass and seeing. This ratio is generally reported as a natural magnitude:

$$m = -2.5 \log_{10} \frac{\phi_{\mathrm{ADU}}}{\phi_{\mathrm{ref|ADU}}} \tag{2.2}$$

where $\phi_{\mathrm{ref|ADU}}$ is the flux of the standard. Natural magnitudes can be interpreted as:

$$m = -2.5 \log_{10} \frac{\int \mathcal{S}(\lambda)\lambda T(\lambda) d\lambda}{\int \mathcal{S}_{\mathrm{ref}}(\lambda)\lambda T(\lambda) d\lambda} \tag{2.3}$$

$\mathcal{S}_{\mathrm{ref}}$ being the SED of the standard. Note that the unknown normalization of T cancels out in the ratio.

Calibration chain In practice, there is not always a primary standard close enough to the science target, that can be observed in the same conditions shortly before or after. Hence, calibrating a survey requires at least one indirection. Usually, we proceed in two steps.

In a first time, the measured fluxes are corrected for the spatial non-uniformities of the imager photometric response (flatfielding) and for the variations of the observing

conditions (zero-points and airmass corrections). The measurements are reported as "uniformized natural magnitudes", or "calibrated natural magnitudes":

$$\hat{m} = -2.5 \log_{10} \frac{\phi_{\mathrm{ADU}|\boldsymbol{x},t}}{\mathcal{F}(\boldsymbol{x})} + \mathcal{Z}(\mathrm{t}) \tag{2.4}$$

$\mathcal{F}(\boldsymbol{x})$ describes the uniformity correction applied to the measurements, and $\mathcal{Z}(t)$ accounts at first order for the variations of the instrument response and the variations of the atmospheric transmission. These "uniformized natural magnitudes" are not specifically anchored on a particular flux scale.

From magnitudes to broadband fluxes Now, to interpret calibrated magnitudes as broadband fluxes, one just needs to know the "uniformized magnitudes" of at least one primary standard. Ideally, one should observe it with the science instrument, and estimate its flux using the standard reduction chain that used to process the science and calibration images. Sometimes, this is not possible, as the primary standard is either too bright for the telescope, or simply not observable from the telescope location. In this case, we have to rely on indirect observations to estimate the "uniformized magnitudes" of the primary standard in the survey telescope system.

From equations (2.2) and (2.4), the natural magnitudes we want to report are given by:

$$m = \hat{m} - \hat{m}_{\mathrm{ref}} \tag{2.5}$$

and can be interpreted as:

$$\phi = 10^{-0.4(\hat{m}-\hat{m}_{\mathrm{ref}})} \times \int \mathcal{S}_{\mathrm{ref}}(\lambda) \frac{\lambda}{hc} T(\lambda) d\lambda \tag{2.6}$$

where $\phi \equiv \int \mathcal{S}(\lambda) \frac{\lambda}{hc} T(\lambda) d\lambda$, $\mathcal{S}(\lambda)$ being the SED of the science object. Note again that the normalization of T does not play a role here, as we use the same model of T to compute both synthetic integrals.

When do we need to map calibrated magnitudes into broadband fluxes ? Generally, this is when we have a model of the science object spectral energy distribution, and we need to confront this model to the observations. This is naturally the case in supernova cosmology, as illustrated for example in figure (1.5): the SN observer frame broadband magnitudes must be interpreted as the integral of the SN SED in the survey filters, in order to derive the SN restframe fluxes. Another common use case is the determination of galaxy photometric redshifts.

Inspecting equation (2.6), we see that the survey flux calibration relies on three main ingredients: (1) at least one primary standard, with a well measured SED $\mathcal{S}_{\mathrm{ref}}(\lambda)$ (2) the natural magnitudes of this standard in the survey system ($\hat{m}_{\mathrm{ref}}$) and (3) accurate measurements of the survey passbands ($T(\lambda)$). In the next two sections, we discuss points (1) and (2).

2.2 Primary Standards

2.2.1 Vega

For historical reasons, Vega[1] has been the main primary standard for decades. In the 1960s and 1970s, numerous attempts were made to calibrate its spectrum against laboratory sources (see e.g. Tüg et al., 1977; Hayes et al., 1975; Hayes and Latham, 1975; Oke and Schild, 1970; Hayes, 1970). These sources, such as Tu Lamps, Pt or Cu blackbodies could all be traced to the fundamental standards maintained by the former National Bureau of Standards[2]. Hayes (1985) compiles and combines most of these measurements, and reports an uncertainty of about 1-1.5% on the absolute flux scale. The measurement of cosmological parameters such as Ω_Λ and w are insensitive to global variations of the flux scale. Thus, we generally ignore this uncertainty. What is more important on the other hand, is the uncertainty affecting the slope of the SED; or more exactly, the uncertainty affecting the flux ratios between different photometric bands. These numbers are difficult to derive from the various estimates. From their dispersion, they seem to be lower than 1% in r and i, higher than 1% in g and z.

Unfortunately, Vega (a magnitude 0 star) is extremely bright and cannot be observed by most modern telescopes. For example, it is about 10^6 times brighter than the magnitude 15 stars that are routinely measured in the SNLS science fields close to the detector saturation limit. And still about 10,000 times brighter than the magnitude 10 stars that may be observed only by strongly defocussing the telescope and reducing the exposure time to its minimum recommended value (1 second). Thus, tying photometric observations to the Vega flux scale involves third party observations of fainter photometric standards, as will be discussed in §2.3.

2.2.2 Hot DA White Dwarfs

With the advent of the Hubble Space Telescope, the need for reliable flux standards in the UV and IR became more acute. Since ground-based UV observations are impossible below the atmospheric cutoff, while near-IR flux measurements are made extremely difficult by the strong H_2O absorption lines, new methods had to be devised to establish these standards. Following a suggestion of Finley and Koester (1991), a new technique was explored, based on model atmospheres of hot pure hydrogen white dwarfs (also called DA white dwarfs in the literature). This approach, which can be used from the far UV to the infrared has been actively developed, over the last decade.

Model Atmospheres The computation of model atmospheres has made dramatic progress since the late 1970s. It is now possible to predict quantitatively with an accuracy of a few percents, the SED of a wide variety of stars, once one knows its fundamental

[1] also known as α Lyrae, HR7001, HD 172167 or BD+38°3238.
[2] now the National Institute of Standards and Technologies (NIST)

basic parameters such as its effective temperature ($T_{\rm eff}$), surface gravity ($\log g$) and metallicity. Stellar atmospheres are described as a plasma of ionized atoms and free electrons, heated from below by radiation. One usually assumes that the atmosphere is globally in hydrostatic equilibrium, which connects temperature, pressure and density. The distribution of atom ionization states depends on temperature and plasma density, and is described by the so-called Saha equation. For any given ionization state, the population of excitation levels is distributed according to the Boltzmann law. Finally, the radiation transport equation describes the interaction between light going through the atmosphere and the atoms in various ionization and excitation levels.

Model atmosphere codes solve iteratively the coupled equations described above and predict the density, temperature, chemical composition and population levels as a function of some depth parameter. They are generally coupled to a spectrum synthesis code such as SYNTHE (Kurucz, 1993) or SYNSPEC (Hubeny and Lanz, 2011) which computes the emergent spectrum from (1) the stellar atmosphere description and (2) a line database which may contain millions of lines if heavy elements are present in the atmosphere.

A classic approximation is to assume Local Thermodynamic Equilibrium (LTE). This means that the stellar atmosphere parameters vary slowly enough within the star to consider each cell in thermal equilibrium with its closest neighbors, the distribution of the atom ionization states and of excitation levels following the Saha-Boltzmann law. In reality, LTE conditions are indeed fulfilled when the rate of net photon absorptions or emissions is indeed much smaller than the collisions between the matter particles, and breaks down otherwise, in particular at high temperatures and low densities – for example, near the surface of a star. NLTE calculations are more computer intensive, as one has to take into account much more couplings between radiation and transitions levels.

For all stars however, one also has to account to some extent, for the non-thermal components of the gas velocity. Convection is generally treated with the so-called "mixing length model", where a typical distance scale, tuned by hand, describes the mean-free path of bubbles of matter. Shorter scale non-thermal motion of matter is often described with a "microturbulent velocity" parameter (ξ) added to the thermal mean velocity of particles (whose individual velocities still follow a Maxwell distribution). Mixing length and micro-turbulence are both tuned by hand, following complex heuristics. While researching for this work, we have tried to quantify the impact on the predicted SEDs, of different mixing length and micro-turbulent velocity assumptions, but we have not succeeded yet.

Three main stellar atmosphere codes currently dominate the landscape: ATLAS (Kurucz, 1993) calculates a 1D, plane-parallel, horizontally homogeneous stellar atmospheres, in radiative and hydrostatic equilibrium, assuming LTE. TLUSTY (Hubeny and Lanz, 1995) makes essentially identical assumptions, but allows for departures from LTE for a certain number of species. PHOENIX (Hauschildt et al., 1995) is a multi-purpose stellar atmosphere code, developed initially for modeling novae and supernovae ejecta.

It computes plane-parallel and spherically symmetric atmospheres, also allowing for departures from LTE.

Many other NLTE models have been developed to describe specific stars. For example TMAP[3] (Werner et al., 2003; Rauch and Deetjen, 2003) is widely used to model stellar atmospheres of compact stars. Another code has been specifically developed within the Montreal group lead by P. Bergeron to model white dwarfs atmospheres of various kinds (see e.g. Tremblay and Bergeron, 2009; Bergeron et al., 1995, and references therein).

Hot DA White Dwarfs The remarkable feature of stellar models is that, at least for simple H and He atmospheres, they depend on a very small number of parameters ($\log g$, $T_{\rm eff}$ and metallicity) which are enough to describe the spectrum at all scales, spectral features and continuum. Hence, one can play the game which consists in (1) estimating the stellar parameters from high-resolution spectra of the local features (for example, the Balmer line profiles), and then, (2) computing from this the spectral energy distribution at all wavelengths. If reddening by interstellar dust is negligible, the model should predict accurately the slope of the spectrum, which is exactly what we expect from a primary spectrophotometric standard.

The spectra of hot pure-hydrogen white dwarfs are essentially featureless, apart from hydrogen Balmer lines in the visible, and Lyman lines in the UV. It is generally admitted that the SED of such objects depends only on the physics of the hydrogen atom. With no metals[4] in the atmosphere, one is not dependent on the quality of the spectral line libraries. Thus, this corresponds to the simplest situation possible, and we can expect that the modeling uncertainties will be minimal. White dwarfs present another advantage: they are intrinsically faint. Hence, a, say $V \sim 13$ white dwarf is necessarily a close object, not affected by interstellar extinction.

The CALSPEC Project One of the goals of the CALSPEC project[5] (CALSPEC, 2011), is to establish fundamental flux standards for the calibration of the HST instruments. Unextincted, hot DA white dwarfs were selected as primary standard candidates (see table 2.1) and observed spectroscopically from the ground and from space. The stellar parameters $T_{\rm eff}$ and $\log g$ are determined from model fits to the Balmer line profiles, generally $H\beta$ to $H\epsilon$. Another approach consists in fitting the Lyman lines visible is the UV. Barstow et al. (2001) compare both techniques and detect significant discrepancies, but attribute them to systematics affecting the measurements.

Over the course of the project, the synthetic spectra of the CALSPEC primary standards have been re-computed several times, using increasingly sophisticated codes. The first iterations relied on D. Koester's LTE white dwarf model atmosphere code (Koester et al., 1979). This code was used in a consistent way to determine the temperatures

[3] http://astro.uni-tuebingen.de/~TMAP

[4] In astronomy "metal" generally means "beyond Helium".

[5] http://www.stsci.edu/hst/observatory/cdbs/calspec.html

	V	$B-V$	$T_{\rm eff}$ $[K]$	$\log g$	spectral type
G191-B2B	11.781	−0.33	61193 (241)[a]	7.492 (0.012)[a]	DA0
			60929 (993)[b]	7.55 (0.05)[b]	
GD 153	13.346	−0.29	38686 (152)[a]	7.662 (0.024)[a]	DA1
			40320 (626)[b]	7.93 (0.05)[b]	
GD 71	13.032	−0.25	32747 (92)[a]	7.683 (0.023)[a]	DA1
			33590 (483)[b]	7.93 (0.05)[b]	

[a] (Finley et al., 1997)
[b] (Gianninas et al., 2011)

Table 2.1: CALSPEC fundamental flux standards. We report the "official" CALSPEC temperatures and surface gravities, taken from Finley et al. (1997), along with the new determinations reported by Gianninas et al. (2011). The differences between both should not be taken at face value, since they are parameters of two very difference codes. HZ43 which used to be among the fundamental flux standards, was recently discarded due to the presence of a bright cool companion.

and surface gravities of the stars (Finley et al., 1997; Bohlin et al., 1995), and to predict their SEDs. Later in the project, it was decided to use instead the TLUSTY NLTE code (Bohlin, 2007, 2003; Bohlin et al., 2001; Bohlin, 2000, and references therein), but for technical reasons that are unclear, the stellar parameters were not re-evaluated using the same code, and the project continued to use the old LTE determinations of Finley et al. (1997). CALSPEC is now considering using the Montreal NLTE white dwarf simulations (Tremblay and Bergeron, 2009) that incorporate more realistic atomic physics, along with the temperature determinations of Gianninas et al. (2011, hereafter G11) performed with the same code. This long history caused a series of small, percentish re-evaluations of the flux scale. The history of these changes can be retraced from the CALSPEC archives, available from their website.

The primary standards listed in table (2.1) set the flux calibration of the HST instruments, notably the *Space Telescope Imaging Spectrograph* (STIS) in the visible, and the *Near Infrared Camera and Multi-Object Spectrometer* (NICMOS) (0.8 – 2.5 μm) in the infrared. These two instruments are then used to expand the HST flux scale to a wider network of standard stars. This network comprises about 60 objects, in the magnitude range $8 < V < 16.5$, and a substantial fraction of it is observable by 4-m class telescopes[6]. Most are hot white dwarfs, but the catalog also comprises redder faint solar analogs ($B - V \sim 0.65$), whose colors are more similar to the apparent colors of

[6]see http://www.stsci.edu/hst/observatory/cdbs/calspec.html

the supernovae.

A special effort was made to re-observe well established standards and include them in the CALSPEC database. Among those is the SDSS primary standard BD+17°4708, a F-subdwarf that defines the SDSS AB flux scale (Bohlin and Gilliland, 2004a). More challenging was the re-observation of Vega (Bohlin and Gilliland, 2004b). This turned out to be feasible, thanks to the fact that the readout amplifier- and ADC-saturation level is greater than the full well capacity. Thus, the excess charge is not lost but bleeds into the adjacent pixels and can be recovered. This work allowed a direct comparison with the measurements of Hayes (1985) anchored to a totally independant metrology chain. It showed a good agreement in the 5000Å $< \lambda <$ 8500Å region, but uncovered problems at the 5-10 percent level (peak-to-peak) outside that range, notably in the regions of the Balmer and Paschen lines respectively.

There are many other spectrophotometric standard libraries around (e.g. MILES[7], NGSL[8]), but none of them seems to have been designed with precision flux calibration in mind. As of today, CALSPEC seems to be the only set of reliable spectrophotometric standards on the sky, with a traceable calibration scheme. As a consequence, an increasing number of dark energy surveys are using it as a calibration reference. It is therefore essential to quantify the systematic uncertainties that may affect the white dwarf flux scale, since these are now shared by virtually all the SN surveys. Since this is almost never discussed in the literature, we take the opportunity to discuss it here, from a CALSPEC user perspective.

2.2.3 Accuracy of the White Dwarf Flux Scale

Let's consider a survey trying to anchor itself on the white dwarf flux scale by observing directly a few CALSPEC standards. What will be the typical uncertainty affecting its calibration ? And, more importantly, can we quantify an uncertainty floor that cannot be beaten by adding more observations ? But first, what do we mean by "calibration uncertainties" ? In order to clarify this, we will define them as: "the relative uncertainties affecting the flux intepretation of the calibrated magnitudes": σ_ϕ/ϕ, were ϕ is defined in equation (2.6). Or equivalently, the uncertainties affecting the quantities: $(-2.5\log_{10}\phi)$.

We expect that a fraction of the error budget will be purely observational and will decrease with the number of calibrators and epochs. Another contribution is related to the stellar atmosphere models used to predict the SED of the CALSPEC primary calibrators. This contribution is much more difficult to estimate, and is not expected to decrease with the number of objects. In what follows, we examine this uncertainty budget in detail and we try to quantify it.

[7] http://miles.iac.es/
[8] http://archive.stsci.edu/prepds/stisngsl/

Uncertainty Model Several sources of uncertainties are likely to affect the CALSPEC spectral energy distributions at all wavelengths. An example are the uncertainties carried by the white dwarf models, or the uncertainties in the determination of the star effective temperatures, which affects primarily the slope of the predicted spectrum. Hence, we expect the calibration uncertainties to be correlated from band to band.

We therefore describe them with a (non-diagonal) $N \times N$ covariance matrix $\mathbf{C}$, where N is the number of survey passbands. Inspecting equation (2.6) we see that $\mathbf{C}$ must be the sum of three contributions: (1) uncertainties related to the WD observations using the survey instrument, (2) uncertainties internal to CALSPEC (related to the transfer of the white dwarf flux scale from the primary standards to the secondaries) and finally, (3) modeling uncertainties, which are common to all CALSPEC stars:

$$\mathbf{C} = \mathbf{C}_{\text{survey}} + \mathbf{C}_{\text{CALSPEC}} + \mathbf{C}_{\text{model}} \tag{2.7}$$

$\mathbf{C}_{\text{survey}}$ is the covariance matrix of the uncertainties that affect the average magnitudes of the CALSPEC calibrators, determined with the survey telescope ($\hat{m}_{\text{ref}}$ with the notations of equation 2.6). The sum ($\mathbf{C}_{\text{CALSPEC}} + \mathbf{C}_{\text{model}}$) describes the uncertainties on the synthetic magnitudes computed from the SEDs released by the CALSPEC project and the survey instrument passbands (see again equation 2.6). $\mathbf{C}_{\text{CALSPEC}}$ describes the flux scale transfer uncertainties between primary and secondary standards. It is expected to decrease with the number of HST observations of the primary and secondary standards. $\mathbf{C}_{\text{model}}$ describe the modeling uncertainties. It may improve with the number of modeled primary white dwarfs, although most of the modeling uncertainties should be common to all stars. Let's now assess the importance of each of these three contributions to the total error budget.

Survey Instrument As shown for example in (Betoule et al., 2012, hereafter B12), survey uncertainties can be made as small as 3 to 5 mmag provided that enough observing time is allocated to the calibration program. The authors identify small correlations between bands, that we neglect here. We have typically:

$$\mathbf{C}_{\text{survey}} = \frac{\sigma^2}{N_{\text{stars}}} \times \mathbf{I} \quad \text{with } \sigma \sim 0.003 \text{ mag} \tag{2.8}$$

Actually, there is an additional contribution due to the potentially limited knowledge of the survey filters. Indeed, uncertainties on the survey passbands (e.g. the wavelength positioning of the passbands) impact the synthetic magnitudes of the CALSPEC standards. This problem is discussed in §2.2.4. In what follows, we will omit the survey uncertainties, as they are in fact of statistical nature.

HST (STIS & NICMOS) The repeatability of an instrument such as STIS can be estimated from the many spectra of star AGK+81 266 that are taken on a regular basis, to monitor the stability of the HST instruments. Following e.g. B12 and R09 one may

determine a repeatability covariance matrix, (e.g. $\mathbf{C}_{\mathrm{STIS}}$), by integrating the spectra of AGK+81 266 in the survey passbands and computing the empirical covariance of these synthetic magnitudes (see for example table E.1 of B12). One typically finds a repeatability of 4, 5, 6 and 11 mmag in *griz*, with significant correlations between neighboring bands. How this contribution applies to the measurements depends on the cause of the measurement-to-measurement dispersion, and also on the CALSPEC observing strategy. In what follows, we assume that the dispersion is independant from measurement to measurement, and is due, for example, to uncertainties in the positioning of the slit with respect to the star. In this case, we have:

$$\mathbf{C}_{\mathrm{CALSPEC}} = \frac{\mathbf{C}_{\mathrm{STIS}}}{N_{\mathrm{STIS}}} \sim \frac{10^{-6}}{N_{\mathrm{STIS}}} \times \begin{pmatrix} 15.5 & 3.9 & -4.4 & -15.6 \\ & 26.0 & 21.0 & 26.0 \\ & & 35.5 & 58.6 \\ & & & 119.1 \end{pmatrix} \begin{matrix} g \\ r \\ i \\ z \end{matrix} \tag{2.9}$$

where N_{STIS} is the number of STIS visits to the standard. We expect this contribution to decrease with the number of STIS visits to a given standard. It will also decrease with the total number of CALSPEC stars used in the calibration:

$$\mathbf{C}_{\mathrm{CALSPEC}} = \frac{1}{N_{\mathrm{stars}}^2} \left(\sum_{s \in \mathrm{stars}} \frac{1}{N_{\mathrm{STIS},s}} \right) \times \mathbf{C}_{\mathrm{STIS}} \tag{2.10}$$

A good way to quantify the uncertainty affecting the passband intercalibration is to evaluate the color uncertainty $\sigma(g-z)$ from the matrix above. If one uses one single star, the uncertainty on $g-z$ due to the repeatability of STIS will be of about $\sigma_{g-z} \sim 0.013$ mag. If, following B12, we anchor the calibration of the survey on 4 CALSPEC standards: `BD +17 4708` (3 visits), and the solar analogs `P330E`, `P177D` and `SNAP2` (one visit each), σ_{g-z} decreases down to ~ 0.006.

Model uncertainties We now turn to the difficult part, which is the estimation of the white dwarf modeling uncertainties. We do not expect this contribution to decrease as the number of primary calibrators. Indeed, it incorporates modeling assumptions that are the same for all stars.

Let's recall the procedure used to determine the HST white dwarf flux scale. It involves four main steps: (1) choose a model atmosphere code and precalculate a grid, indexed by the WD stellar parameters (T_{eff}, $\log g$ and possibly metallicity) (2) take a high resolution spectrum of the WD, and estimate its T_{eff} and $\log g$ by comparing the grid line profiles with the observed line profiles (3) predict a synthetic SED for these parameters (4) observe the object with HST and derive from this a transmission curve. Then, repeat this procedure for as many objects as possible.

Ideally, to estimate the accuracy of the white dwarf flux scale one should repeat the entire procedure above with at least two different model atmospheres, in order to assess the impact of the modeling assumptions. As of today, the full procedure has

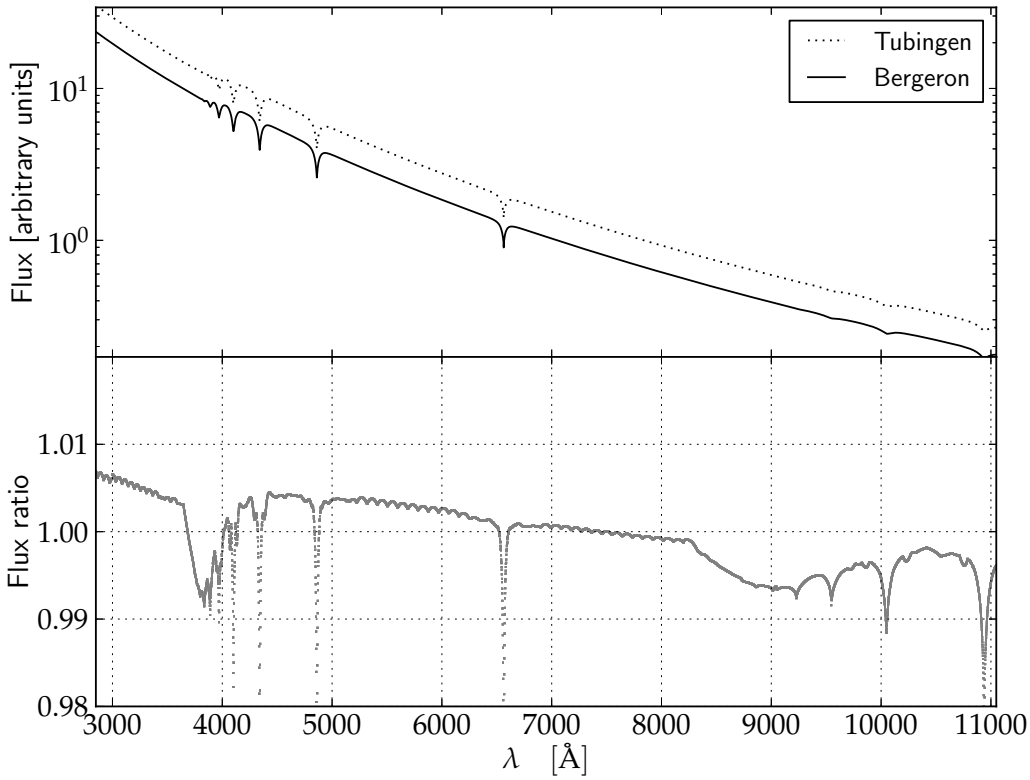

Figure 2.1: Comparison between the Tübingen model (TMAW) and the Bergeron model for star `GD 71`. Both models were computed for pure hydrogen atmosphere, with $T_{\rm eff} = 33590K$ and $\log g = 7.93$. Upper panel: model spectra (shifted, to distinguish them). Lower panel: ratio.

been implemented only twice: once with the Koester (LTE) model atmospheres and the FKB97 LTE temperatures, and a second time with the Bergeron (NLTE) model and the G11 NLTE temperatures. It would be extremely instructive to repeat it again with the (NLTE) Tübingen atmospheres as this would yield a direct comparison of two similar NLTE models, incorporating similar physics. However, this has not been done yet.

Instead, we can estimate $\mathbf{C}_{\rm model}$ by comparing the Bergeron and Tübingen models of the same WD primary calibrators, at the same temperatures. This may be slightly pessimistic, since nothing guarantees that fitting the WD Balmer line profiles with the Tübingen models would yield the same temperature and surface gravity as those determined in G11. However, this is the best we can do so far. The Bergeron models of the three primary calibrators listed in table 2.1 (Gianninas, private communication) were integrated into the SNLS/MegaCam passbands. The same was done for the Tübingen

models of the same stars at the same temperatures and surface gravities[9]. Since we are only interested in the color differences, both models have been rescaled to the same flux in the 7000 Å $\lesssim \lambda \lesssim$ 8000 Å wavelength region, where no Balmer line is present. Then, we take the difference between both sets of synthetic magnitudes as an estimate of a $\sim 1\sigma$ uncertainty.

$$\mathbf{C}_{\text{model}} = \mathbf{\Delta m} \cdot \mathbf{\Delta m}^T \tag{2.11}$$

Again, model uncertainties are at first order independent of the number of CALSPEC objects used as calibrators. They reflect the model assumptions. Conservatively, we pick the star that exhibits the largest differences, and

$$\mathbf{C}_{\text{model}} = \mathbf{\Delta m}_{\text{GD71}} \cdot \mathbf{\Delta m}_{\text{GD71}}^T = 10^{-6} \times \begin{pmatrix} 9.2 & 5.2 & -0.8 & -14.0 \\ & 2.9 & -0.4 & -8.1 \\ & & 0.1 & 1.2 \\ & & & 22.3 \end{pmatrix} \begin{matrix} g \\ r \\ i \\ z \end{matrix} \tag{2.12}$$

As can be seen, the modeling is the largest contribution to the total uncertainty budget, with $\sigma_{g-z} \sim 8$ mmag.

Stellar parameters The question arises of whether we should account for the impact of the uncertainties affecting the stellar parameter determinations. We choose to be conservative and consider that similar models, making similar physical assumptions are likely to be affected by similar biases. We find that surface gravity has essentially no impact on the slope of the primary calibrator spectrum. On the other hand, temperature has a sizable effect. Its contribution can be estimated from the derivatives of the WD synthetic magnitudes with respect to temperature, and the temperature uncertainties reported by G11 (see table 2.1):

$$\mathbf{C}_T = \sigma_T^2 \times \left(\frac{\partial \mathbf{m}}{\partial T_{\text{eff}}}\right) \left(\frac{\partial \mathbf{m}}{\partial T_{\text{eff}}}\right)^T \tag{2.13}$$

The size of the derivatives seem to depend slightly on temperature: they seem to be larger for colder stars. It is not clear whether these uncertainties should average or with the stars. We choose to average them, since the primary WD temperatures differ significantly. We find:

$$\mathbf{C}_T = 10^{-6} \times \begin{pmatrix} 2.1 & 0.9 & -0.1 & -1.1 \\ & 0.5 & -0.1 & -0.7 \\ & & 0.0 & 0.1 \\ & & & 1.1 \end{pmatrix} \begin{matrix} g \\ r \\ i \\ z \end{matrix} \tag{2.14}$$

Temperature uncertainties are not a major contribution to the overall uncertainties: $\sigma_{g-z} \sim 0.002$ mag.

[9] obtained from http://dc.g-vo.org/theossa

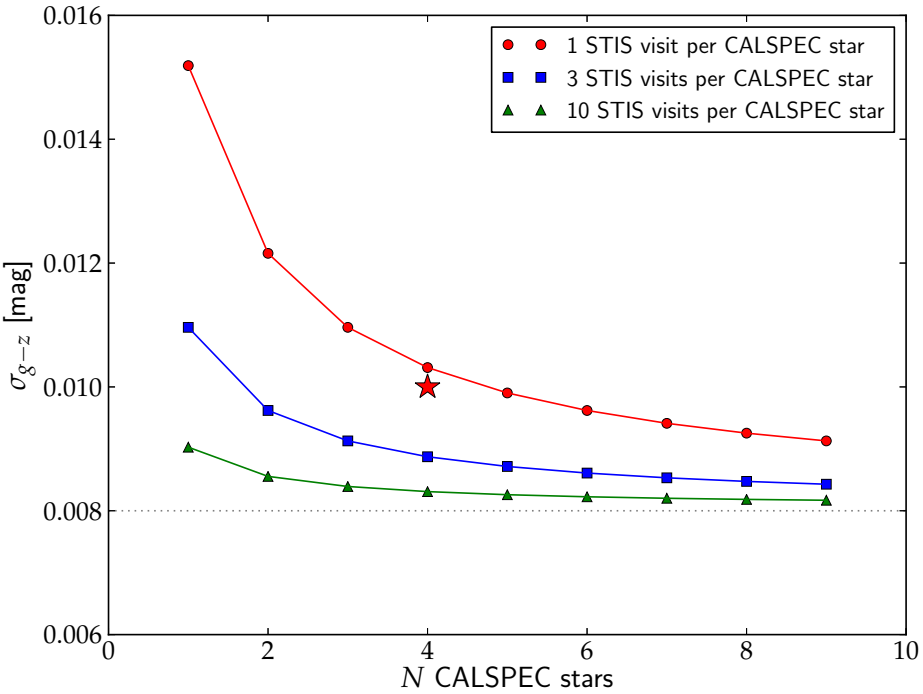

Figure 2.2: Precision on the $g - z$ relative calibration, depending on the number of CALSPEC stars used in the survey, and the number of STIS visits. The dotted line shows the model related uncertainties. The star shows where SNLS currently stands, with observations of `BD +17 4728` and the three solar analogs listed in table (2.2).

Putting Everything Together Now that we have estimates of all the contributions to the calibration uncertainties, let's combine them together. We leave out the survey uncertainties, as they can be made as small as we want. We obtain (using 4 CALSPEC stars totalling 6 visits):

$$\mathbf{C}_{\text{CALSPEC}} + \mathbf{C}_{\text{model}} + \mathbf{C}_T = 10^{-6} \times \begin{pmatrix} 14.5 & 6.9 & -1.8 & -18.35 \\ & 8.8 & 3.9 & -3.38 \\ & & 7.5 & 13.5 \\ & & & 48.2 \end{pmatrix} \begin{matrix} g \\ r \\ i \\ z \end{matrix} \tag{2.15}$$

So, a realistic CALSPEC calibration would carry a color uncertainty: $\sigma_{g-z} \sim 0.01$ mag (1%). In figure (2.2), we show how σ_{g-z} decrease as a function of (1) the number of CALSPEC stars used to calibrate the survey and (2) the number of STIS visits for each CALSPEC stars. As can be seen, significant gains in precision may be obtained by increasing the number of STIS visits to each standard.

Now that we have quantified the uncertainties carried by CALSPEC, the question

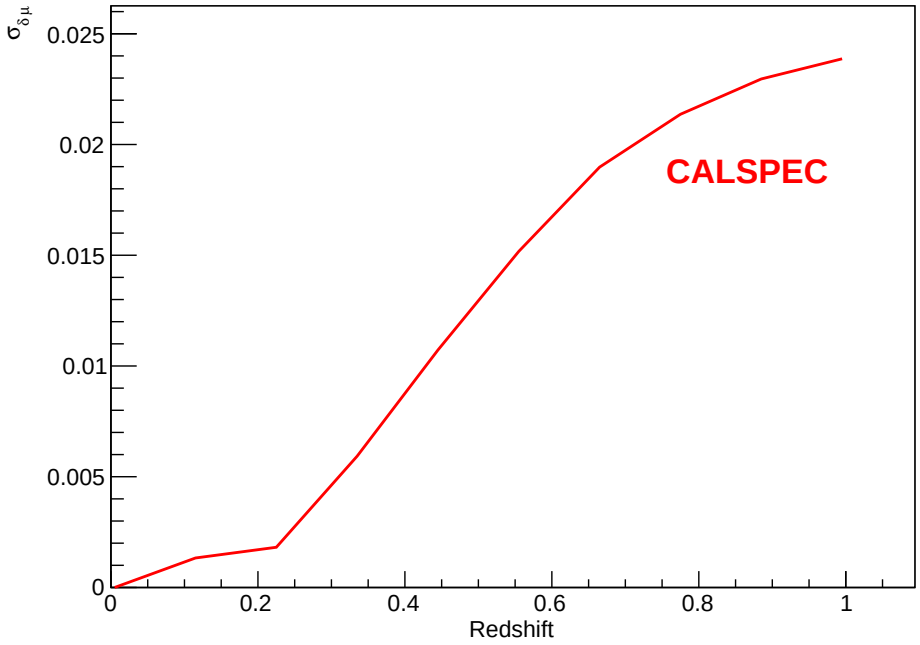

Figure 2.3: Systematic uncertainties affecting the relative variations of the SNLS SN Ia distance moduli, as a function of z.

that matters is: what is the impact of these uncertainties on the supernova luminosity distances ? To quantify this, we have propagated the CALSPEC calibration uncertainties throught the SNLS-3 year analysis, and computed how they impact the supernova distance moduli. The result is shown on figure (2.3) and should be compared with figure (1.2). As can be seen, the uncertainties carried by the CALSPEC SEDs (assuming the survey is perfect) amounts to about 0.02 mag at a redshift of 0.8. This corresponds to an uncertainty on d_L of about 1% at a redshift of $\sim$ 0.8, and an uncertainty on w of 0.05.

2.2.4 White Dwarfs or Solar Analogs ?

The CALSPEC project has extended the white dwarf flux scale to a wider network of stellar calibrators, in particular objects that are redder than the very blue hot DA white dwarfs used as primary calibrators. The question is then whether to observe primarily the primary calibrators or the redder secondary calibrators.

In the first case, one would avoid the uncertainties related to the repeatability of STIS, at the price of calibrating the survey with objects that are extremely different from the science objects (much bluer in particular). In the second case, one would have to include

	V	$B-V$	$E(B-V)$	$T_{\rm eff}$ $[K]$	$\log g$	spectral type
P041C	12.00	+0.62	0.027	5960	3.95	G0V
P177D	13.47	+0.66	0.031	5780	3.60	G0V
P330E	13.00	+0.64	0.035	5820	4.00	G0V
SNAP-2	16.20	$\sim XX^a$	0.036	5740	4.10	G
BD+17 4708	9.47	+0.44				sdF8

[a] Synthetic color estimate.

Table 2.2: CALSPEC redder secondary standards.

the STIS repeatability in the error budget, but one would benefit from the fact that the calibrators have colors which are closer to those of supernovae.

The first option would be optimal if we knew perfectly the survey passbands. However, any uncertainty on the passband model is going to impact the interpretation of the calibrated magnitudes (equation 2.6) via the factor:

$$\kappa(\lambda) = \frac{\int \mathcal{S}(\lambda)\lambda T(\lambda) d\lambda}{\int \mathcal{S}_{\rm ref}(\lambda)\lambda T(\lambda) d\lambda} \tag{2.16}$$

It is obvious from the equation above that if the calibrator spectrum is exactly similar to that of the science objects, then $\kappa(\lambda)$ should be insensitive to uncertainties in the filter wavelength position. Conversely, the more the calibrator spectrum differs from that of the science objects, the larger this impact will be.

So, what is the best option for a supernova survey ? Actually, supernovae are complicated objects. Their observer frame colors vary significantly as a function of time and redshift. Hence, to decide on the optimal stategy, the best option is to use real data (e.g. the SNLS 3 year dataset), to compute the effect of a filter shift in wavelength, on the SN Ia distance moduli:

$$\delta\mu = \frac{\partial\mu}{\partial\lambda}(z) \times \delta\lambda \tag{2.17}$$

depending on whether one uses a blue or red fundamental standard to interpret the calibrated magnitudes. As already discussed in §1.6.1 the derivatives of the SNLS distance moduli have been computed as a function of all identified sources of systematics, the calibration systematics in particular. Hence, it is relatively easy to compute the quantities $\delta\mu$ above for all SNLS supernovae.

Figure (2.4) shows the impact of a 1-nm filter shift, on the distance moduli, as a function of z. The computation has been performed using two different calibrators: SNAP-2 a red solar analog, and GD 153 one of the CALSPEC blue white dwarfs. The first thing that is clearly apparent on the figure, is that if we get the survey passbands wrong (especially in the g and r band), we end up with a redshift-dependent bias affecting

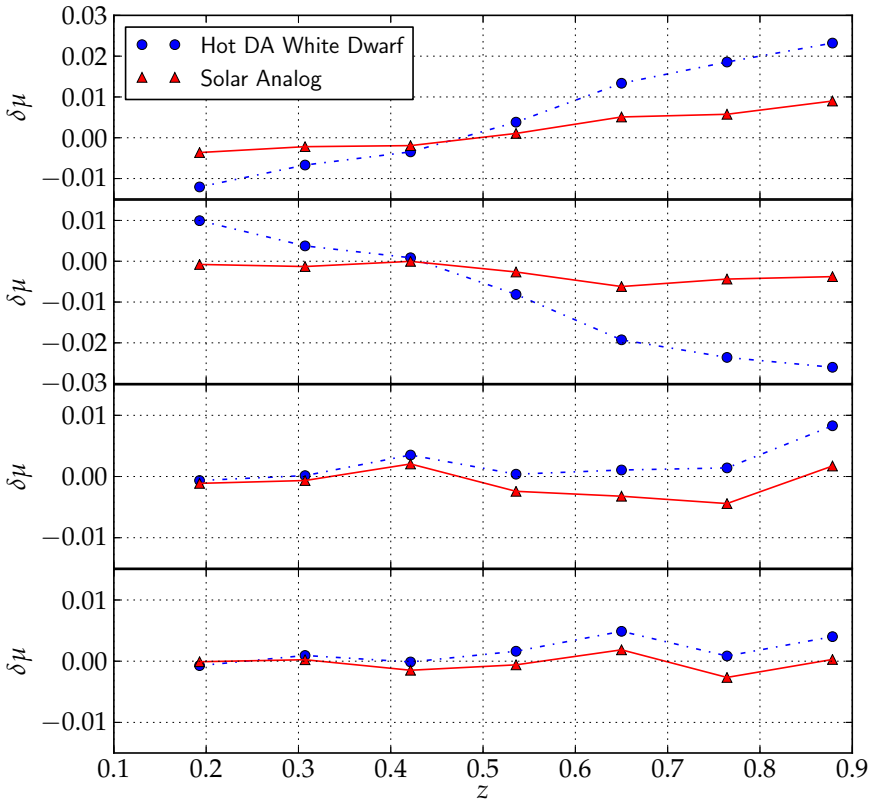

Figure 2.4: Sensitivity of the SNLS3 SN Ia distance moduli to a $\delta\lambda = 1$ nm filter shift, depending on whether one uses a blue or a red fundamental standard. (upper panel: g, middle panels r and i, lower panel: z).

the supernova distances. The second conclusion is that the effect is much larger if we use a blue standard than if we use a red standard. Simply because the SEDs of redder standards are more similar to the SED of SNe Ia in the observer frame. Hence, there is no alternative but use red standards to calibrate a supernova survey.

2.3 Going Down the Flux Ladder

In the previous section, we have dealt with the choice of the optimal primary standard(s). We have considered two options: Vega, the historical primary calibrator and the newer HST white dwarf flux scale. We now turn to the second fundamental problem of photometric calibration, which is the establishement of a robust metrology chain between

the flux calibrators and the sciences images. In other words, we want to measure the magnitudes of the primary standard(s) in the survey photometric system. This poses a series of problems, as most standards are significantly brighter than the science objects.

2.3.1 From Vega to the science images

Until recently, supernova surveys had no alternative, but use Vega as a fundamental flux calibrator. The historical low-z supernova magnitudes were all tied to the $UBVRI$ system defined by the faint equatorial standards established by Landolt (1992). Calibrating the distant supernovae against a different photometric system would introduce additional systematic errors affecting the comparison of nearby and distant supernova fluxes.

As discussed above, Vega is $\sim 10^5$ times brighter than the brightest sources that can be routinely measured with a 4-m class telescope, and about 10^8 to 10^{10} brighter than the typical science targets (SNe Ia in the $0.3 \lesssim z \lesssim 1$ redshift range). None of the Landolt papers report magnitudes for Vega, which was probably too bright for his own instrumentation. A quick bibliographic search reveals that tying a modern survey to the Vega flux scale actually requires going through an undetermined number of indirections, as illustrated on figure (2.5). Each step of this long chain involves brigher standards, observed with smaller telescopes, operated by different teams, and equipped with different generations of photometers and filters.

Furthermore, it is not possible to infer the magnitudes of Vega in the Landolt system, since none of the authors on this long calibration path does report natural magnitudes. Indeed, until recently, it was customary to publish magnitudes in a "standard" photometric system whose passbands could differ significantly from those of the telescope actually performing the measurements. Hence, large (generally unpublished) color corrections had to be applied to the measured magnitudes to put them in accordance with the "standard" system (e.g. Landolt, 2007). This was considered good practice, as it allowed one to compare easily measurements made by various authors, at the price of breaking the relation between magnitude and flux (equation 2.3). Note that using color regressions to compare measurements in slightly different filters is usually acceptable for main sequence stars, but works poorly for more exotic sources, such as supernovae and galaxies.

Finally, a quick look at figure (2.5) shows that Landolt's magnitudes in the bluer UBV passbands ($3500\text{Å} < \lambda < 5500\text{Å}$) and the magnitudes in the R and I passbands ($5500\text{Å} < \lambda < 8500\text{Å}$) have a different filiation. This increases the risk of introducing uncertainties in the reconstructed colors of Vega, which would be nearly impossible to assess.

The net consequence of this, is that the standard calibration chain, from Vega to the catalogs of faint standards in use today should be considered broken. Until 2007 however, all supernova surveys had to rely on it, since no better alternative was available. Quite fortunately, the situation changed when Landolt and Uomoto (2007) published

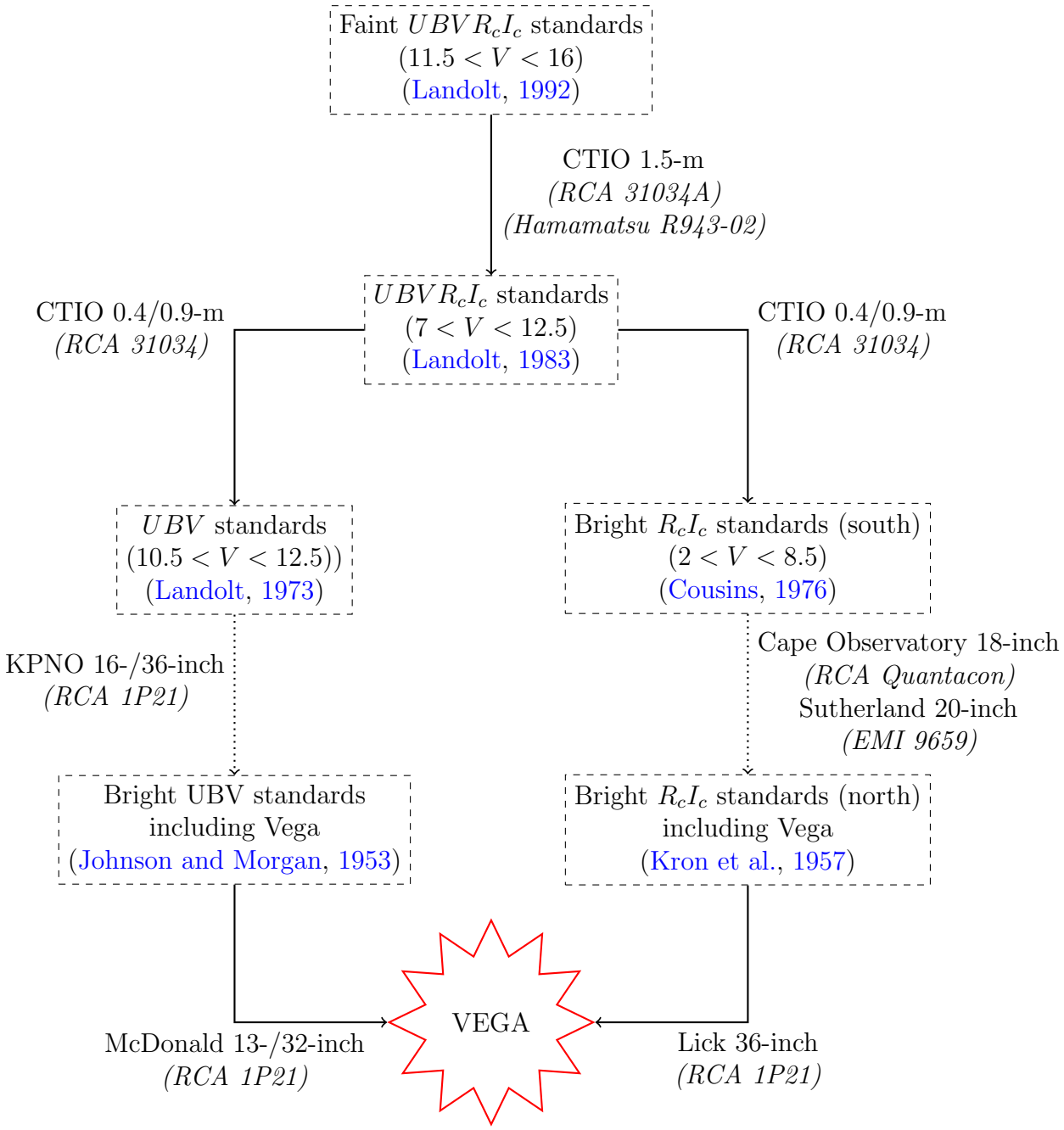

Figure 2.5: Overview of the calibration path, from the Landolt (1992) standard star catalog to the original observations of Vega. Arrows link each given catalog to the catalog that was used to calibrate it. Dotted arrows signal that there might be additional indirections between the two catalogs. The telescopes used to perform the observations are reported, as well as the photometer types. Note that all observers used slightly different filters, and has to apply color-dependant corrections to their measurements to "place them in the original standard systems" defined by Johnson and Kron.

magnitudes for a series of spectrophotometric standard stars observed with HST, allowing to anchor the Landolt system on the HST flux scale. Also, with the publication of the CALSPEC (2011) database of faint spectrophotometric standards tied to the HST flux scale, it became possible to build much shorter calibration paths from the flux standards to the science images.

2.3.2 From CALSPEC to the science images

Most of the work discussed in this section has been done within the SNLS and SDSS-II supernova surveys. Both projects have identified that photometric calibration is a major source of systematics. Therefore, significant efforts have been invested into building a robust calibration chain. The alternate, shorter calibration paths explored independently by SNLS and SDSS-II are drawn in black on figure (2.13).

The SNLS way Regnault et al. (2009) took advantage of the work of Landolt and Uomoto (2007) who publish magnitudes for a subset of the CALSPEC spectrophotometric standards. Among those, only one star was sufficiently red, the F-subdwarf `BD +17 4708`. It is about $\sim 10^4$ fainter than Vega ($V \sim 9.5$), but still too bright to be observed directly with MegaCam.

What could be done however was to *infer* its calibrated MegaCam magnitudes from the Landolt observations (see e.g. figure 2.6). Indeed, the relations between two sets of magnitudes are essentially linear as a function of the color:

$$\begin{aligned} \hat{g} &= V_L + \alpha_g \times (B-V)_L + \Delta g \\ &\dots \\ \hat{z} &= I_L + \alpha_z \times (R-I)_L + \Delta z \end{aligned}$$

The slopes $\alpha_g \dots \alpha_z$ of the color transformations are fitted to MegaCam observations of Landolt stars. Those do not span a large color range, hence, the slopes are affected by non-negligible uncertainties. Fortunately, the colors of `BD +17 4708` are very close to the average colors of the Landolt stars. The contribution of the slope uncertainties to the inferred magnitudes is therefore very small.

The quantities $\Delta g \dots \Delta z$ quantify how far `BD +17 4708` lies from the pure linear transformations. The dispersion around the Landolt-to-MegaCam color relations is of about 2% (figure 2.6). This sets the size of the uncertainties affecting the magnitudes of `BD +17 4708` inferred with the linear transformations only. Hence, not estimating these offsets would degrade very significantly the quality of the calibration. They are evaluated from the extinction, surface gravity, effective temperature and metallicity of `BD +17 4708` (estimated by various authors in the literature) using a grid of spectral models, integrated in the MegaCam and Landolt passbands. The complete discussion can be found in §10.2 of Regnault et al. (2009) and is not reproduced here. It suffices to say that these offsets are not negligible and contribute significantly to the calibration

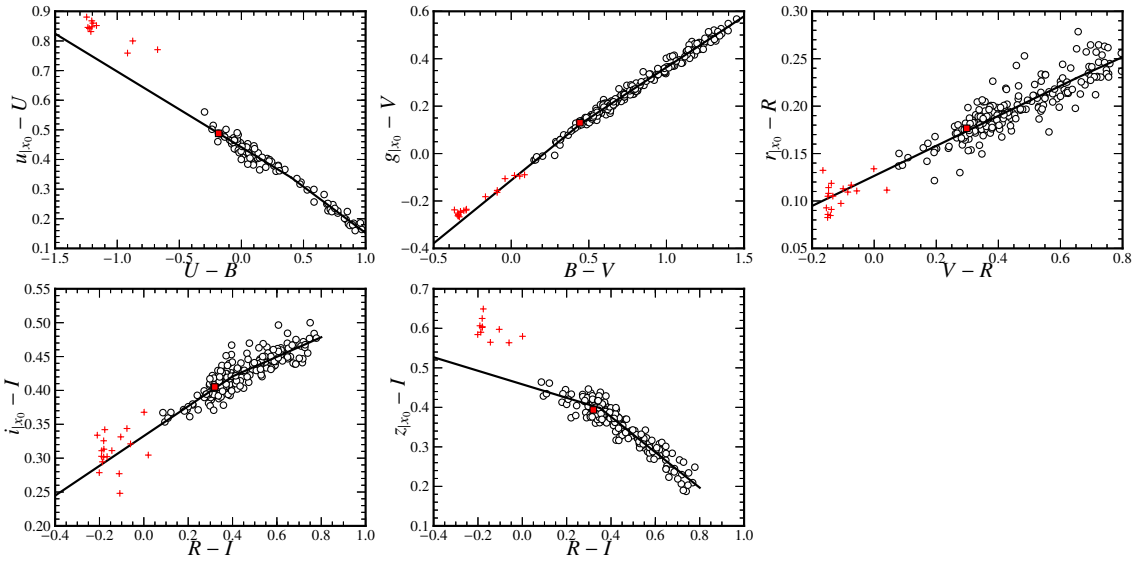

Figure 2.6: Landolt to MegaCam color transformations.

uncertainties. The final error budget reported in R09 is dominated by the uncertainties affecting the inferred MegaCam magnitudes of the fundamental standard.

The SDSS way The SDSS took a slightly different route to CALSPEC (Holtzman et al., 2008). The 2.5-m SDSS telescope is supplemented by a smaller 0.5-m photometric telescope (PT) that monitors the atmospheric variations along the line of sight of the 2.5-m. The PT was able to observe directly the three CALSPEC "solar analogs" `P041C`, `P177D` and `P330E`, whose colors are very similar to the average colors of the stars used to transfer the PT calibration to the main survey, and determine the small PT-to-SDSS2.5 m color transformations. These solar analogs are a slightly better choice than `BD +17 4708`, their colors being closer to those of SNe Ia (§2.2.4). SNLS could not rely on these stars, for the good reason that they had no published Landolt magnitudes. SDSS could, because they had full control of a smaller calibration telescope and could observe them directly.

Holtzman et al. (2008) did not attempt to estimate offsets to the linear color transformations. Since they had three primary calibrators, they instead combined their three calibrations, which also gave a calibration uncertainty. It is of about 0.5% in all bands, except in z where is reaches 1.5%. These uncertainties are comparable to those reported by Regnault et al. (2009). As for SNLS, the magnitudes of the primary flux standards dominate the SDSS-II calibration systematics.

Joint SNLS - SDSS Calibration In 2007, SNLS started observing the red CALSPEC objects listed in table (2.2), in conjunction with its own supernova fields. The goal

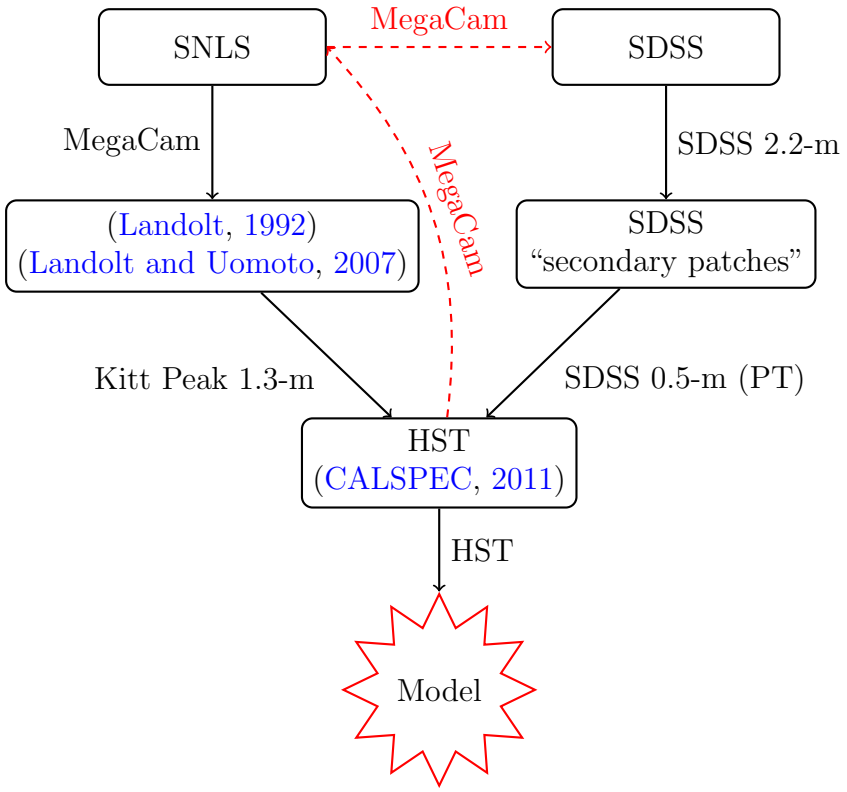

Figure 2.7: Redundant calibration chains explored by the SNLS and SDSS-II suveys. The black arrows draw the paths initially set by (Regnault et al., 2009) (SNLS) and (Holtzman et al., 2008) (SDSS-II). The red dashed arrows shows the paths opened by Betoule et al. (2012).

was to shorten drastically the calibration path by anchoring the survey directly to the HST flux scale. Observations of a fraction of the SDSS-II supernova fields were included into the calibration program, in order to compare directly the flux calibration of both surveys. Two years later, SNLS and SDSS-II launched a joint effort to re-analyze their respective dataset with similar methods. This included a joint recalibration of both surveys, described in Betoule et al. (2012).

The new paths opened by the SNLS supplementary observations are shown in dashed red on figure (2.13). They allow to tie the SNLS survey to the HST flux scale through several different routes: the older one that goes through Landolt, a new indirect path, through the SDSS calibration chain, and a new short route through direct observations of the CALSPEC faint standards. Actually, SDSS-II itself offers two distinct calibrations: through observations of `BD +17 4708` (their historical standard), or with specific observations the three CALSPEC solar analogs (SA). As a consequence, SNLS was able to anchor the SNLS survey to CALSPEC through four different, almost independent paths, allowing it to build a very robust and redundant calibration chain.

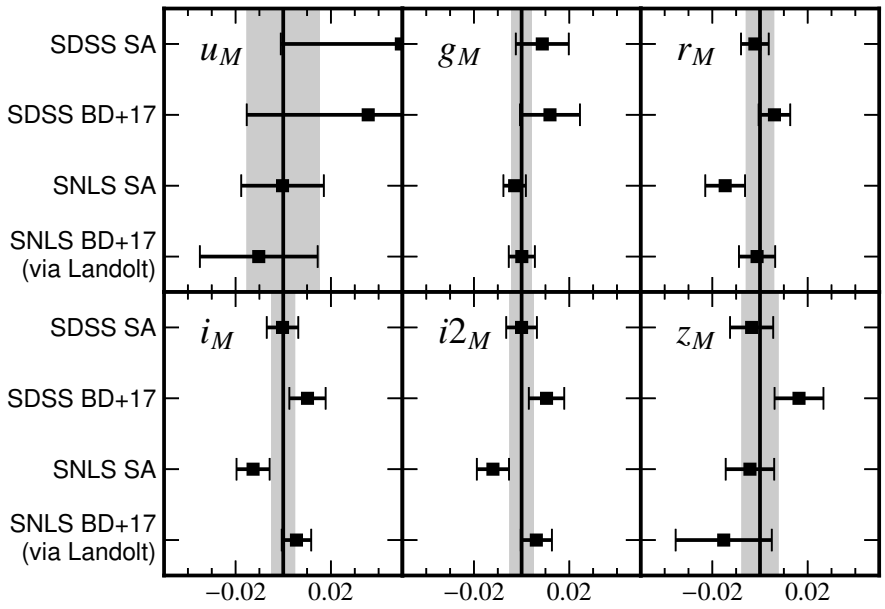

Figure 2.8: Consistency of the four calibration paths in the SNLS bands: (1) SDSS to the CALSPEC solar analogs (SDSS SA) (2) SDSS to `BD +17 4708` (SDSS BD+17) (3) SNLS to the CALSPEC solar analogs (SNLS SA) (4) SNLS to `BD +17 4708` (SNLS BD+17). We represent the difference (in magnitude) between each calibration and the average calibration obtained by combining all four paths (0.01 mag $\sim$ 1%).

Direct observation of the HST standards with MegaCam are still difficult. For the two brightest sources listed in table (2.2), it was necessary to use short exposure times (3 seconds) and to defocus the telescope in order to avoid saturation. Alternate in-focus / out-of-focus exposures of the same fields had to be taken, in order to compare the flux estimates in both configurations. The problem was then to estimate systematic differences between (1) long in focus exposures of the science fields (2) short in focus exposures of the calibration fields and (3) short out of focus exposures of the same calibration fields. The associated uncertainties were estimated to be of about 0.2% at most.

The consistency between the four calibration routes is shown on figure (2.8) which shows the dispersion of the calibration solutions with respect to their average values, for all four different paths. The agreement between the different calibrations is of the order of 1% in the $gri-$ and $z-$bands. The SNLS and SDSS combined AB offsets, along with their uncertainties are reported in table 24 of Betoule et al. (2012), which is reproduced in table (2.3). For the first time, the total uncertainty affecting the relative

	σ_{u_M}	σ_{g_M}	σ_{r_M}	σ_{i_M}	σ_{i2_M}	σ_{z_M}
(Regnault et al., 2009)	—	0.003	0.005	0.007	—	0.019
(Betoule et al., 2012)	0.0145	0.0035	0.0051	0.0042	0.0043	0.0069

Table 2.3: SNLS-3yr and SNLS 5-yr calibration uncertainties (CALSPEC not included).

flux calibration is below 1%, in all bands (but u). More importantly, the uncertainties affecting the magnitudes of the primary standards is of the same order as the effect of the CALSPEC SED uncertainties, or the uncertainties induced by our imperfect knowledge of the survey passbands. Inspecting carefully figure (2.8) one may even detect a small tension between `BD +17 4708` and the CALSPEC solar analogs. This tension is probably due to systematics internal to CALSPEC.

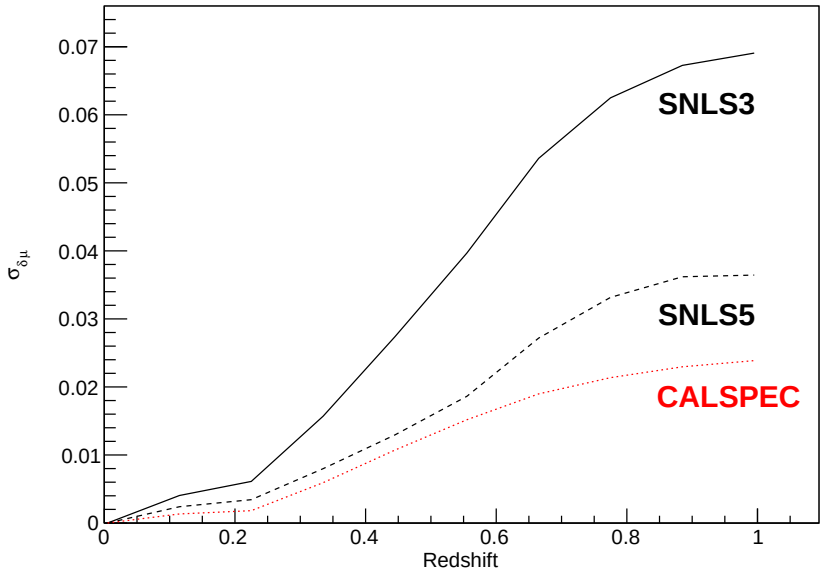

Figure 2.9: Calibration related systematics affecting the relative variations of the SNLS SN Ia distance moduli, as a function of z. SNLS3 propagates the calibration described in Regnault et al. (2009), SNLS5, corresponds to the work presented in Betoule et al. (2012), and CALSPEC represents the CALSPEC related systematics described in this work.

What does this mean for the supernova distance measurements ? We summarize the situation on figure (2.9). The improvement resulting from the much shorter and redun-

dant calibration routes explored in the SNLS-5yr analysis is clearly apparent. SNLS is now very close to being limited by the CALSPEC uncertainties. Furthermore, we have seen previously that these latter uncertainties may be decreased with more HST visits to the standard stars.

2.4 Observational Challenges

Up to now, we have concentrated on what we think is the fundamental problem of photometric calibration today: establishing a set of primary flux standards and obtaining magnitudes for each of them with the survey instrument. Of course, precision photometric calibration involves other challenges, most of them observational.

In this section, we briefly discuss some of the difficulties that have to be overcome in order to deliver measurements at the per-mil level. They should not be underestimated, and actually absorb most of the time and efforts of calibrators over the world. Recent work shows however that the limitations of future surveys will probably not be observational. For example, (Betoule et al., 2012) have demonstrated that with some care and with an appropriate observing strategy, it is possible to obtain night-to-night repeatabilities as small as a few mmags for bright stars. Furthermore, they have shown that with O(100) epochs per band on a selected fields, many observational uncertainties average out very well, hence the mmag-level calibration uncertainties at the end of the survey.

2.4.1 Imager & Survey Uniformity

Imager Uniformity The uniformity of the survey depends primarily on how one controls the instrument photometric response. This response has no reason to be uniform itself. The focal plane is a mosaic of a few dozen CCDs, read out by O(100) different amplifiers (more on recent imagers). The CCD quantum efficiencies differ slightly from chip to chip, while the gain of the readout electronics varies from amplifier to amplifier. Furthermore, the characteristics of the readout electronics fluctuates over time, primarily as a function of temperature. These effects yield small ($\sim 1-2\%$) discontinuities of the photometric response.

Early tests with the MegaCam imager revealed that the response of the instrument was affected by non-uniformities as large as 10% from center to corner. This effect was actually anticipated, as it had already been encountered with previous generation instruments (see Manfroid et al., 2001; Manfroid, 1995). On most wide field imagers, the solid angle subtended by a pixel varies over the focal plane. On MegaCam, it is about 4% larger at the center than on the corners. Flat fields are generally determined by accumulating light from extended isotropic sources, such as the sky at dusk or dawn. Hence, the flat-field maps applied to the science images integrate less light on the corner than at the center, *regardless of the instrument transmission*. Since point sources are

not affected, science exposures should display 4% center-to-corner non uniformities after flat-fielding.

However, the predicted effect is much smaller than what is measured on real MegaCam images (4% versus 10%). The cause of the additional non-uniformities was pin-pointed later in the course of the survey: flat-fields are contaminated by indirect light that coming from internal reflections in the wide-field corrector optics. This contamination varies slowly over time as a function of the relative positions of the wide-field corrector lenses, and of the reflectivities of the optical surfaces.

As a consequence, corrections to the average flat fields have to be measured and applied to the pixels (or to the measured stellar fluxes). Following the approach described in (Manfroid et al., 2001), a method was developed to measure the relative variations of the measured fluxes of a great number of stars, as a function of their focal plane positions (see details in Betoule et al., 2012; Regnault et al., 2009; Magnier and Cuillandre, 2004). The method is based on dithered observations of dense stellar fields and works as follows.

The instrumental magnitude of a star observed at location $\boldsymbol{x}$ on the focal plane ($m_{|\boldsymbol{x}}$) may be parametrized as:

$$m_{|\boldsymbol{x}} = m_{|\boldsymbol{x}_0} + \delta\mathrm{zp}(\boldsymbol{x}) + \delta k(\boldsymbol{x}) \times \mathrm{color} \tag{2.18}$$

where $m_{|\boldsymbol{x}_0}$ is the instrumental magnitude of the star at an arbitrary reference location $\boldsymbol{x}_0$ (for example, at the center of the focal plane). $\delta\mathrm{zp}(\boldsymbol{x})$ and $\delta k(\boldsymbol{x})$ are maps that describe the relative variations of the instrumental response, with respect to the reference position ($\delta\mathrm{zp}(\boldsymbol{x}_0) = \delta k(\boldsymbol{x}_0) = 0$). If the filter transmission functions are perfectly uniform, one expects that $\delta k(\boldsymbol{x}) = 0$ everywhere on the focal plane.

Only a fraction of the field stars are actually observed at the reference location. Hence, most star magnitudes $m_{|\boldsymbol{x}_0}$ are unknowns, and must be determined along with the δzp and δk maps. This adds about 100,000 unknowns to the fit, turning it into a very high dimensionality problem. However, it is a also linear problem, with a very sparse jacobian matrix, and it is possible to take advantage of this, to obtain the exact least-square solution (see details in appendix A of Regnault et al., 2009). One can therefore show that for series of observations taken with a well chosen dithering pattern, it is possible to determine simultaneously the δzp and δk maps and the star magnitudes (up to a global constant). Figure (2.10) shows an example of $\delta\mathrm{zp}(\boldsymbol{x})$ maps obtained with this procedure.

Since the $\delta\mathrm{zp}(\boldsymbol{x})$ and $\delta k(\boldsymbol{x})$ maps must be determined on a regular basis, the technique turns out to be expensive. It requires about 13 dithered exposures per band, taken hence a little more than 2 hours of photometric time. As the solution is very sensitive to drifts in the observing conditions, photometricity and PSF stability are two strong requirements. It may be possible to find dithering patterns that are more immune to variations in the observing conditions, however, this has not been done yet.

Within the CFHTLS survey, maps were re-determined every 6 months. This is non-optimal, as the imager reponse can develop 1-2% variations over shorter time scales.

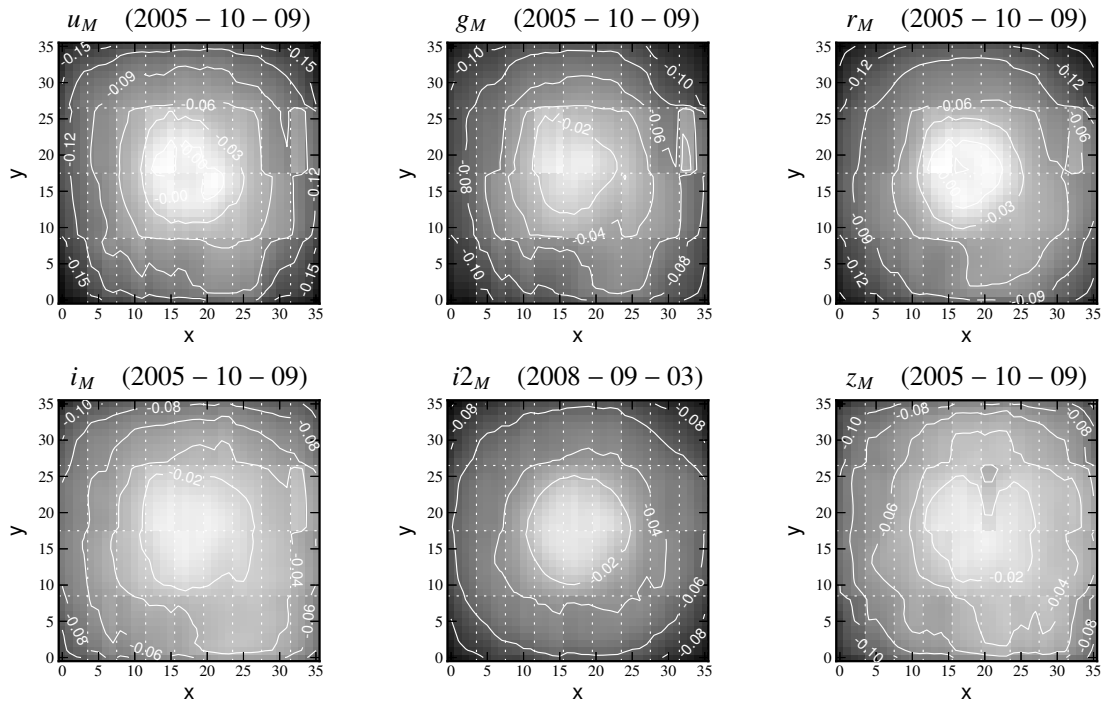

Figure 2.10: Map of the photometric corrections relative to the twilight flat fields using dithered observations of dense stellar fields. Each panel represents the $\delta\mathrm{zp}(\boldsymbol{x})$ map for the entire focal plane (`CCD#0` up left, `#35` down right). The corrections are large, typically 10% from center to corner (figure taken from Betoule et al., 2012)

Clearly, any technique that would allow to monitor the imager uniformity at a lesser expense would be welcome.

Filter Uniformity A very common feature of the large interference filters that equip most modern imagers is that their transmission is not uniform, but varies significantly as a function of position. For example, for some MegaCam passbands (notably r and i), the position of the filter cutoffs vary by up to 5-nm from center to corner. This is much more than what is expected from the fact that the transmission of interference filters depends slightly on the average angle of the beam with respect to a normal to the filter surface.

These non-uniformities generally exhibit a radial pattern which is well explained by the coating deposition technique. They slightly complicate the analyses, as the instrument photometric system depends on the focal plane position. This is not really a problem for main sequence stars, whose magnitudes can be transported from one location to another

using linear color transformations (i.e. the $\delta k(\boldsymbol{x})$ maps presented above). However, when working with supernovae or galaxies, one has to know the effective instrument passbands at every focal plane location. How to deal with such situations is discussed in detail in B12 and R09.

Survey Uniformity Future wide field surveys such as DES or LSST plan to rely on similar dithering schemes, applied on survey scale, to "auto-calibrate" their catalog. These techniques are actively tested using simulations. It is clear already that approaches seeking to derive a global survey calibration from the intercalibration of neighboring fields are likely to be affected by significant biases that are variable as a function of position on the sky. Rather, the key to control the uniformity of a large survey, seems to intercalibrate fields that are distant, by repeatedly observing them, over short timescales, preferably at similar airmasses. For example, Padmanabhan et al. (2008) was able to improve significantly the uniformity of the SDSS survey, with additional large strips, orthogonal to the direction of the "regular" SDSS observing strips, and connecting distant survey areas, hence "rigidifying" the uniformity solution.

2.4.2 Survey passbands

We have seen in this chapter that controlling the passband shape of the survey imager is essential to interpret the measured magnitudes as broadband fluxes (§2.2.4). We can reduce the sensitivity to survey passbands uncertainties by choosing a primary calibrator as similar as possible to the science targets. However, the impact on $\sigma_{\mu(z)}$ is still strong.

Unfortunately, stars are not ideal objects to test passbands. At first order, they exhibit nearly flat and featureless spectral energy distributions, with essentially no feature large enough to have an impact on broadband fluxes. Hence, it is nearly impossible to determine the position of individual filter fronts just from observations of spectrophotometric standards.

The SDSS project anticipated this problem and built an apparatus to measure *in situ* the filter fronts (see Doi et al. (2010) and chapter 3). They were able to re-determine the survey passbands with a wavelength precision of a few Å, at various stages of the survey, hence nearly eliminating the passband related uncertainties. In contrast, SNLS is still limited by uncertainties of $\sim 10-20$ Å on the position of the r_M and i_M filter fronts. In the next chapter, we will detail how we may constraint the MegaCam passbands using a dedicated calibration instrument.

2.4.3 Atmospheric transmission

The last point that should be discussed is absorption of stellar light by the atmosphere. Several physical processes participate in atmospheric extinction (see e.g. Stubbs et al., 2007a, for a brief review). In the blue, molecular (Rayleigh) scattering dominates, with a typical cross-section that varies like $\sigma \propto \lambda^{-4}$. This effect essentially depends on

pressure, and airmass, both being measured and reported by telescope control systems. Scattering by aerosols and small particles (generated by pollution, dust from volcano eruptions, forest fires etc.) also contribute to the total extinction. The cross-section varies like $\sigma \propto \lambda^{-k}$, where k depends on the typical size of the aerosol particles. The concentration and distribution of aerosols in the atmosphere changes, depending on the winds and aerosols producing events. Therefore, the aerosol transmission should vary with azimuth and time. It is routinely mapped during daytime by networks that publish the aerosol optical depth at various wavelengths.

Molecular absorption by O_2, O_3 and H_2O also contributes to atmospheric absorption, in the form of strong saturated lines. Saturated lines block most of the incoming light, and their contribution to broad band absorption is independent from elevation. Oxygen is responsible for two features at 699-nm and 760-nm. However, this effect is extremely stable — only slightly pressure dependent. Ozone is totally opaque to UV below 300-nm, and also generates weak absoption (a few percents) between 500-nm and 700-nm. Ozone concentration varies as a function of time, but it is routinely measured by dedicated earth observation satellites, since it has such a strong impact on earth climate. Finally, water is omnipresent in the atmosphere, under many different forms. Precipitable water is responsible for very strong and variable absorption features in the NIR and IR. Water droplets and ice crystals (clouds) seem to be gray scatterers (e.g. Buton et al., 2012). The concentration of water is highly variable as a function of time and direction. Also, cloud layers may form and evaporate very quickly, water absorption going from "gray" to "band distributed" over time scales of a few minutes.

Radiative transfer codes, such as MODTRAN[10] are more and more widely used to predict the transmission of the atmosphere, knowing its molecular and aerosol contents. Recent work by Buton et al. (2012) or Burke et al. (2010) has shown that, by measuring locally absoption features from standard star spectra taken in various conditions, and comparing them with precomputed MODTRAN absorption components, it is possible to infer the atmospheric absorption along the line of sight with a very good accuracy. Clearly, the most problematic component is water. Dedicated instruments are being designed and built to measure the precipitable water and the thin cloud coverage over the observatory as a function of time and direction. This is done either in emission (from GHz to IR, especially at 10µm) or in absorption (spectrograph, narrow band wide field imagers). Clouds may also be detected in reflection with LIDARS.

As said above, atmospheric transmission may vary by percents on timescales of minutes, and these variations are generally invoked to explain the difficulty to obtain photometric repeatabilities lower than 1% from ground based observations. Future surveys such as LSST have issued very strong repeatability requirements[11] (below 1% for bright sources, not dominated by photon statistics). The main motivation is to be able to associate a passband to each single observations. However, for non-transient sources,

[10] http://www.modtran.org

[11] see e.g. the LSST Science requirements: http://www.lsst.org/files/docs/SRD.pdf

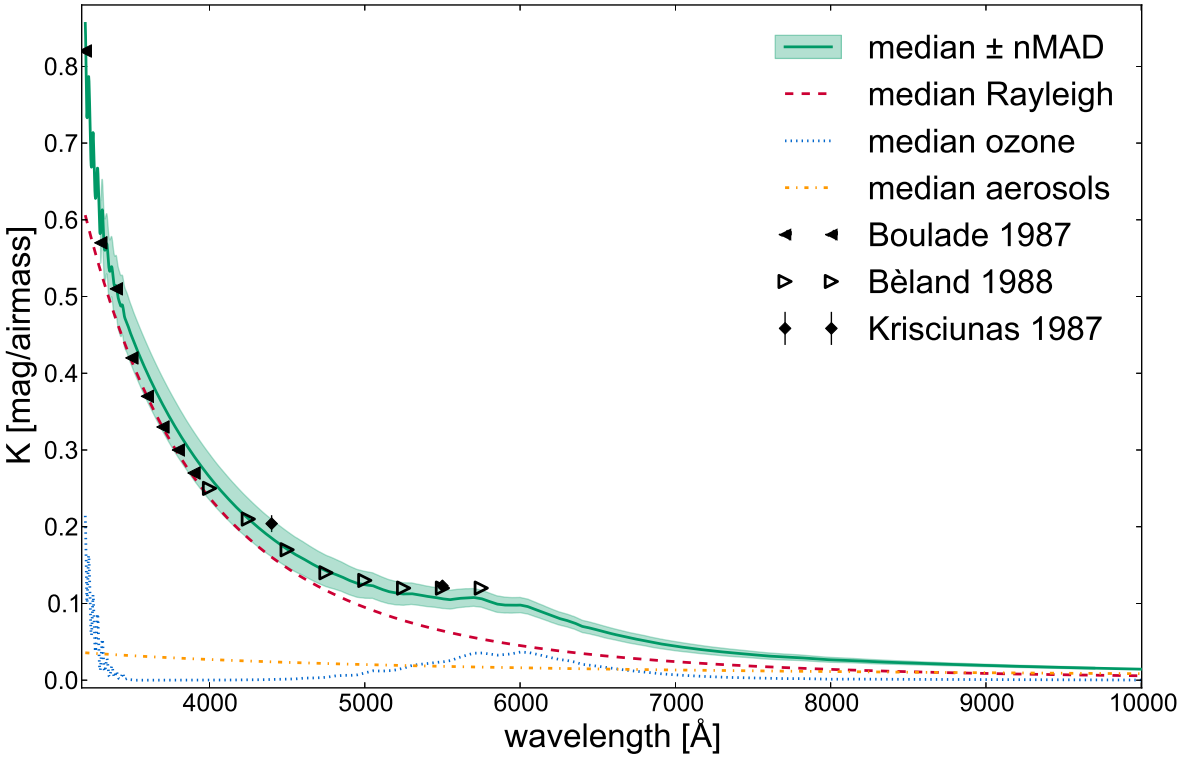

Figure 2.11: Average extinction law fitted on spectrophotometric standard stars observed with the SNfactory SNIFS Integral Field Spectrograph (Buton et al., 2012). The model is constructed from a series of transmission functions (rayleigh & aerosol scattering, O_2, O_3 and H_2O absorption) precomputed using the MODTRAN atmosphere simulation code (http://www.modtran.org).

the very large number of survey epochs per field should allow one to average out most of the atmospheric effects.

What is the effect of atmospheric absorption on broad band surveys with 100+ epochs per field ? More exactly, what are the effects that cannot be corrected using broad band dataset itself ? Actually, there are not many. At first order, the net effect of the atmosphere is to change the effective transmission by a passband-dependent amount. However, these variations are fully absorbed in the instrument zero-points (the $\mathcal{Z}(t)$ term in equation 2.4). Those can be determined at a higher frequency, and their uncertainties average out well. Another effect of the atmospheric transmission is to distort the shape of the effective passbands, especially in the near-UV. However, the effect seems barely visible in the current datasets (e.g. SNLS), taken over a reasonable range of airmass

($X \lesssim 2$).

One atmospheric component has to be accounted for however. The clouds, especially the light cirrus, seem to display postentially large (0.02 mag to 0.1 mag) spatial inhomogeneities over typical scales of 1° (Ivezic et al, 2007). These scales are now smaller than the field of view of modern imagers. These inhomogeneities have to be disantangled from the inhomogeneities of the instrument response. They may perturbate significantly the techniques that seek to obtain photometric flatfields from dithered observations, as well as the autocalibration strategies discussed above. A possible parade would be to image the cloud coverage in emission, using a wide field infrared camera, observing at $\lambda \sim 10\mu$m. Another approach is control the imager response with a very good precision, for example using a uniform calibrated light source such as those described in the next chapter.

Finally, knowing the *average* shape of atmospheric transmission is essential in the scheme where one tries to propagate to the sky an instrumental calibration obtained from calibrated sources places in the telescope enclosure. As discussed above, techniques exist to determine it combining MODTRAN and spectroscopic observations.

2.5 Conclusion

In this chapter we have given an overview of the standard calibration approaches that are in use today in most Dark Energy projects. We have focussed on calibration strategies, and barely covered the observational aspects, which are essential to obtain the required precision, but seem well under control.

The situation on the stellar calibration front is summarized on figure (2.12). Most calibrators are still at least two orders of magnitudes brighter than the brightest SNe Ia used in the cosmological studies. However, the situation has significantly improved with the release of faint CALSPEC standards a few years ago. The magnitude of these standards is indeed comparable to the magnitude of the Landolt stars, which can be easily observed with the large survey telescopes in use today.

All recent Dark Energy Surveys have been anchored on the HST white dwarf flux scale, through direct or indirect observations of CALSPEC standards. This is a much safer approach than relying on the older Vega systems. However the SEDs released by CALSPEC carry uncertainties that are not negligible, and will ultimately limit the measurements of w. Some of these uncertainties are related to the repeatability of the HST instruments. Their impact may decrease with more HST observations of the CALSPEC standards. However, a significant fraction of the CALSPEC error budget comes from the white-dwarf models used to predict the spectral energy distribution of the primary standards. These uncertainties are difficult to estimate, since they are essentially due the (in)adequacy of various assumptions made in complex stellar modeling codes. For this reason, it seems absolutely necessary to add redundancy in the system, and build a parallel and totally independent calibration path, relying this time on laboratory

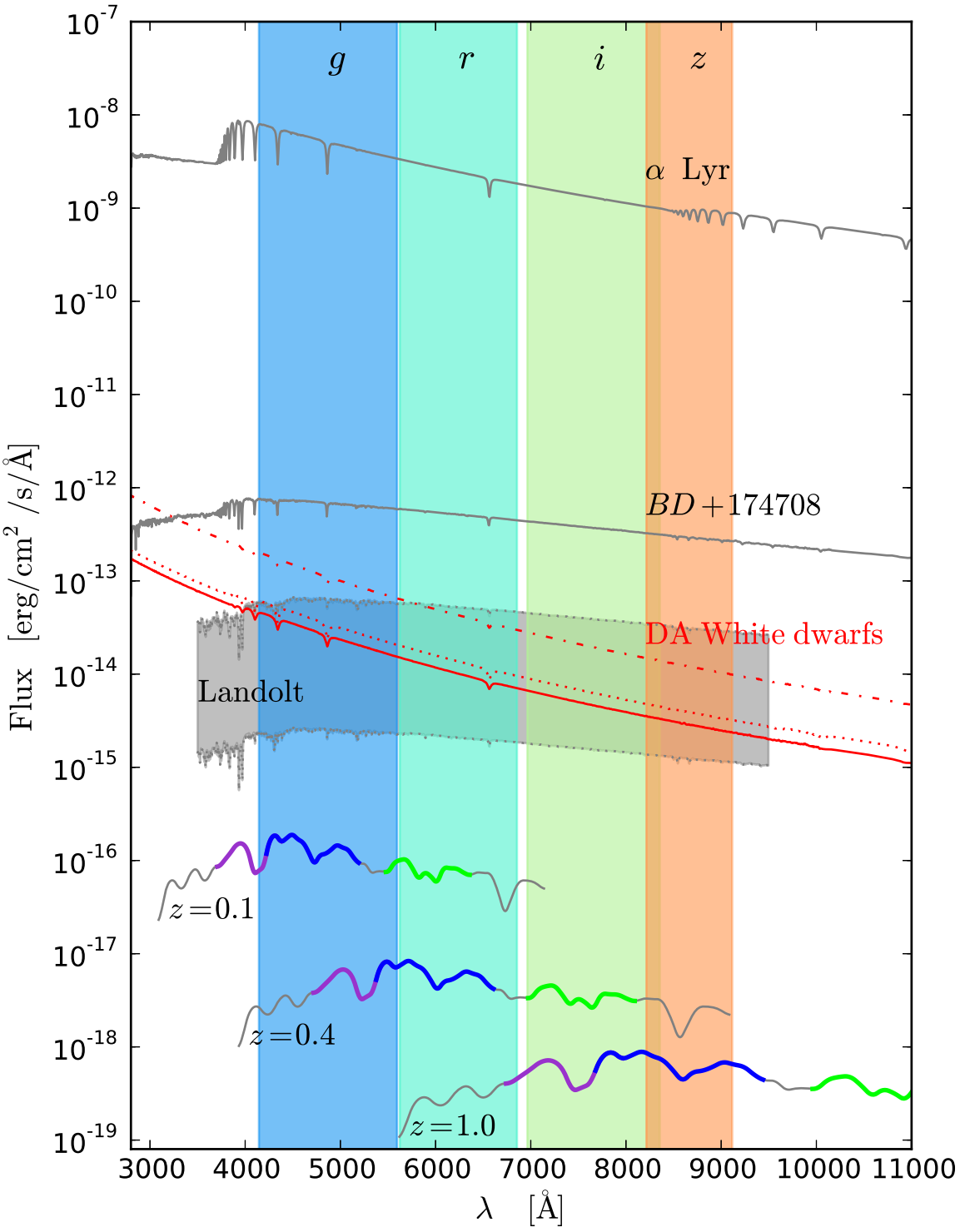

Figure 2.12: Standard stars and supernovae. The magnitude of the fainter CALSPEC standards are comparable to those of the Landolt stars.

standards. This is the subject of the next chapter.

A last crucial point, that has been mentioned several times in this chapter, is the control of the survey passbands. We have discussed their impact on the supernova distances, and we have seen, using real data, that a 1-nm error in the wavelength position of some passbands (g notably), may induce a $\sim 1\%$, redshift dependent bias on the SN distance moduli. It is therefore essential to determine the position survey passbands with typical accuracies of $1 \sim$ Å, and then, to monitor the survey passbands, using dedicated instrumentation.

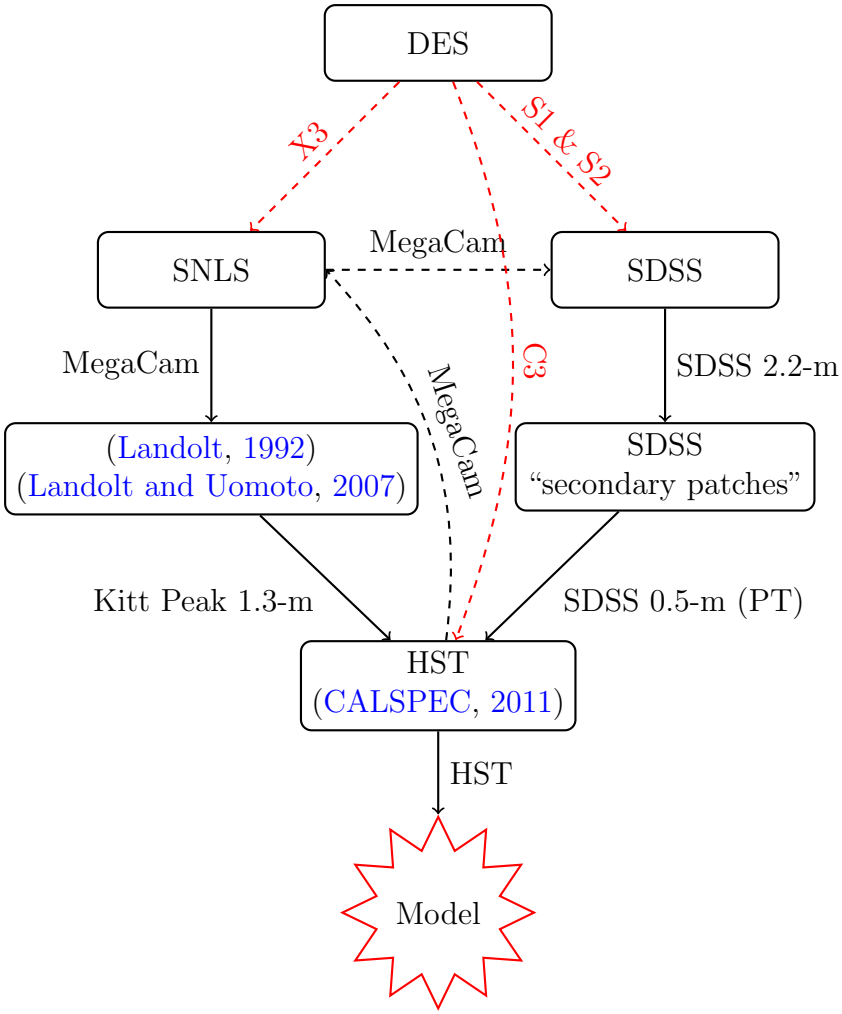

Figure 2.13: Redundant calibration chains explored by the SNLS and SDSS-II suveys. The black arrows draw the paths initially set by (Regnault et al., 2009) (SNLS) and (Holtzman et al., 2008) (SDSS-II). The red dashed arrows shows the paths opened by Betoule et al. (2012).

3 Instrumental Calibration

The idea of using laboratory sources to calibrate astrophysical measurements has been around for decades, as illustrated by the early attempts in the 70s to calibrate the SED of Vega, using Pt and Cu ovens as calibrators (see Hayes, 1985, and references therein). Since then, the situation has considerably changed. Emerging fields such as supernova cosmology have issued stringent requirements on photometric calibration. On the detector side, the advent of CCD sensors delivering a 0.1% linearity over five orders of magnitude, and repeatabilities of a few 10^{-4} over short time scales has revolutionized photometric measurements. New calibrated photometers, such as Si photodiodes, make it possible to perform absolute flux measurements with an accuracy of 1-2 per-mil (in the visible) — to be compared with the 2-3% delivered by the laboratory sources used in the 70s. This situation has triggered new efforts to tie photometric measurements to the flux scale maintained by the Institutes of Standards.

Most of these new projects share the same metrology chain, as they all rely on Si photodiodes calibrated at the National Institute of Science and Technology (NIST)[1] or similar institutes (§3.1). The projects described in this chapter can be divided into two categories. Some projects attempt to replicate the pioneering work of Hayes, using small purpose-built telescopes, calibrated using NIST standards and facilities (§3.2). These efforts are extremely welcome, as they will permit to compare directly the white dwarf flux scale, with the laboratory standards maintained by NIST. However, as discussed in the previous chapter, establishing absolute flux standards on the sky is not enough. One must also characterize and monitor the passbands of the survey instruments that perform the science observations. The last few years have seen a flurry of instrumental designs, seeking to measure *in situ* the throughput of the survey telescopes currently in activity (§3.3). Some of these projects aim principally at controlling the position of the filter fronts over the life of the survey. Others are more ambitious and seek to directly measure the throughput of the instrument, and then project this calibration on the sky.

DICE[2] is a calibrated light source design, proposed by a team of instrumentalists and members of the SNLS collaboration. The design of the source differs in many ways from its competitors. We discuss in (§3.4) the main design principles. The instrument itself is described in §3.5. Prior to its installation on site the apparatus is characterized spectrophotometrically at various temperatures, on a precision test bench (§3.6). We finally give a short overview of the analysis of the MegaCam/ SnDICE calibration exposures.

[1] http://www.nist.gov
[2] Direct Illumination Calibration Experiment

3.1 Metrology chain

The metrology chain maintained by NIST is represented on figure (3.1). The primary flux standard is an electrical substitution cryogenic radiometer, called the *Primary Optical Watt Reference*[3] (POWR) (Houston and Rice, 2006). An electrical substitution radiometer measures optical power (optical watts) in terms of electrical power. It consists in an almost perfectly absorbing cavity connected to a constant temperature heat sink, with a thermal conductor of known conductance. The cavity is equipped with a temperature sensor, and heated with an electrical heater. When illuminated by an optical beam, its temperature rises, and the heater current is decreased to keep the temperature constant. The beam flux is then equal to $R \times (i^2_{\text{beam}} - i^2_{\text{no beam}})$, where R is the heating resistor and i the current. The system is operated at a stable cryogenic temperature (4.2 K) which increases its sensitivity. Of course, corrections have to be applied, to account for imperfect absorption by the cavity and losses, for example in the cryostat window. According to NIST, POWR measures optical power with typical uncertainties of $\sim 0.01\%$ over three orders of magnitudes in flux (µwatts to milliwatts).

POWR is used to maintain the calibration of a set of tunable lasers called SIRCUS[4] (Brown et al., 2006, 2000). SIRCUS covers a large wavelength range, from the UV ($\sim$ 210 nm) to the IR ($\sim$ 11µm). The SIRCUS calibration is then transferred to a Trap Detector, i.e. a tunnel of photodiodes, arranged so that each photodiode can detect the light reflected by the photodiode placed immediately before it. Such a detector has an effective quantum efficiency of nearly 1 over a large wavelength range. The calibration carried by the Trap Detector is then disseminated over a larger set of so-called "working standards", i.e. Si photodiodes in the visible and near-infrared. This transfer is performed at much lower intensities ($\sim$ µW), using lamps and monochromators, at another NIST facility called Spectral Comparator Facility[5] (SCF). The client photodiodes (the ones that can be purchased from NIST) are finally calibrated against these working standards — chosen at random for each client photodiode, in order to minimize systematic biases.

The calibration transfer is performed with so-called "substitution method". This means that the device being calibrated and the calibrator are alternatively placed in front of the source being used to realize the transfer (either SIRCUS or SCF). This implies that the source must be extremely stable in time. The intensity of lasers may display variations over time, at the level of a few percents. Hence, the SIRCUS lasers are equipped with feedback systems to stabilize them. Lamps are also intrinsically unstable. The SCF sources are therefore monitored in real time to measure the relative variations of the intensity actually being delivered by the source.

The metrology chain described in this section may seem overly complicated for our needs. It has been designed indeed to perform *absolute* spectrophotometry over a large

[3] http://www.nist.gov/pml/div685/grp06/powr.cfm
[4] http://www.nist.gov/pml/div685/grp06/sircus.cfm
[5] http://www.nist.gov/pml/div685/grp03/spectral_facilities.cfm

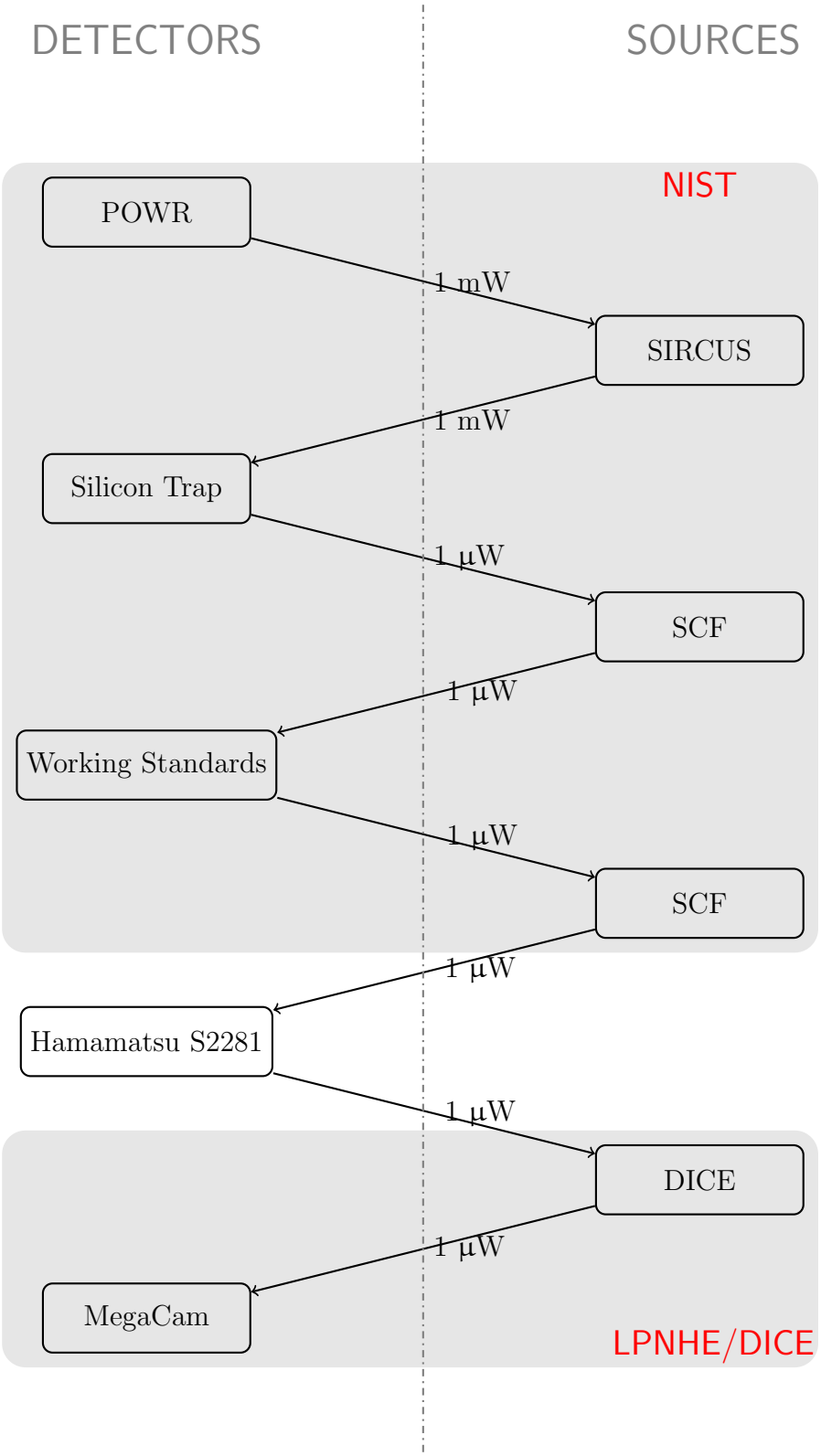

Figure 3.1: NIST and DICE metrology chain.

range of fluxes, and to disseminate it efficiently. On our side, we only need *relative* spectrophotometry at low flux, for a very small number of calibrated sources. However complicated, the NIST chain is operated and monitored daily. It delivers routinely measurements that are precise at a level of $\sim 0.2\%$ in the visible and 1% in the UV and near-infrared. Given the precisions attained by the calibration projects described in this chapter, it is probably too early to question its accuracy.

We may have to do so in the future however, and this for two reasons. First, the uncertainties in the infrared may be a limitation when future space-based infrared imagers start delivering large numbers of high-redshift SNe Ia. Second, we do not know yet how the uncertainties reported by NIST are correlated. As discussed earlier, the precision on w depends on the structure of the full correlation matrix. If one day the flux calibration of a Dark Energy survey depends on NIST, it will be important to obtain this information.

3.2 Dedicated Calibration Telescopes

Over the last two decades, flux metrology has moved from 1-2% source standards to detector standards, that are accurate at the 0.1% level. These dramatic improvements, combined with a much better control of atmospheric transmission, justifies revisiting the historical experiments of Hayes and collaborators. Several teams pursue precisely this goal.

ACCESS The ACCESS collaboration (e.g. Kaiser et al., 2010a,b) is building a small rocket borne ⌀40-cm telescope, equipped with a low-resolution ($R = 500$) spectrograph. The sensor is a HgCdTe device, operated at $\sim$ 140K, and tailored to be sensitive enough ($20\% < \mathrm{QE} < 60\%$) from 350-nm to 1.7µm. The ensemble telescope+instrument is being built, and will be calibrated at NIST, directly on the SIRCUS infrastructure. The goal is to measure the *relative* variations of the instrument transmission at the 1%-level or better from the near-UV to the IR.

The main motivation for a rocket borne experiment is to avoid the absorption lines from the OH radicals, that are formed at high altitude, between 70-km and 89-km. Indeed, these lines strongly affect observations in the near-IR, between 0.85µm and 2.25µm. It also permits to avoid total absorption of UV-rays by ozone — although the ozone layer is at much lower altitude, and can be avoided with balloon flights.

ACCESS will observe a selection of bright standard stars during a series of sub-orbital missions, thus being able to transfer the NIST flux scale to the stars. The type of the mission unfortunately imposes very severe constraints on the telescope size and observing time, hence, on the brightness of the stars that can be observed. The flight time above 100 km will be of about 400 seconds. Typically, one may spend a few seconds observing a very bright standard (such as Vega or Sirius), and devote the rest of the mission to a

unique fainter standard ($6 < V < 8$), the goal being to obtain a S/N of ~ 200 for both targets, in a single rocket flight.

As a consequence, ACCESS will only be able to explore the flux zone between Vega and BD +17 4728 (see figure 2.12), inaccessible to most modern survey telescopes (besides HST). It is a little surprising that ACCESS has selected Vega and Sirius among its standards, since those stars are difficult to model, and not observable by any modern telescope. It is also surprising that they have not chosen to concentrate on a few bright DA white dwarfs, which would have yielded a direct check of the white dwarf flux scale. However, if the ACCESS stars are re-observed by HST, this will nevertheless provide a direct comparison between the HST and NIST flux scales, with the atmosphere factored out.

NIST Standard Stars A similar approach may be followed from the ground, at least in the 350 nm $\lesssim \lambda \lesssim$ 1000 nm wavelength range, where the atmosphere is reasonably transparent. NIST plans to operate a NIST-calibrated spectrophotometer (AESoP) mounted on a $\varnothing$10-cm telescope, and to establish with this instrument a catalog of absolutely calibrated standards (e.g. McGraw et al., 2012). There are detailed plans to perform an exquisite calibration of the telescope+instrument assembly, and to monitor it during the observations. There are also plans to model and monitor the atmospheric transmission in real time. However, once again, the selected stellar calibrators are bright, in the magnitude range $0 < V < 5$. Hence, this calibration effort will heavily rely on HST observations to bridge the gap between the $V \sim 5$ calibrators and the objects usually observed by survey telescopes.

As a summary, dedicated calibration projects are currently underway to transfer the NIST flux scale on stellar objects. Obtaining the sub-percent precision necessary to be competitive with the white-dwarf flux scale is extremely challenging though. ACCESS may be limited by the small number of observations gathered for each star, while the NIST team will have to rely on a very accurate modeling of the atmospheric transmission. However, with the help of additional HST observations, they will both provide independent checks of the white dwarf flux scale, which is a very good thing to do.

Will this fulfill the calibration requirements of future Dark Energy surveys? Unfortunately no. While it is clear that improved networks of standard stars, anchored on a more accurate flux scale will undoubtely help, it does not relieve survey calibrators from monitoring their passbands throughout the life of the survey, as SDSS did (see again the discussion in §2.2.4).

Filter fronts cannot be monitored with a good precision just using stellar observations. As a consequence, future survey instruments will have to be characterized using dedicated monochromatic, or quasi-monochromatic calibration sources. This problem has been well identified in the broadband astronomy community, and a flurry of calibration source designs have been proposed over the last decade. Some have as a unique objective

the characterization of the filter passbands (Doi et al., 2010), in particular the position of the filter fronts. Others seek to determine routinely the absolute flux transmission of the telescope, (Stubbs et al., 2010). In what follows, we will give a brief overview of a selection of these calibrations projects.

3.3 Instrumental Calibration of the Survey Telescopes

Flat field screens Calibration systems such as dome flat screens have been in operation for decades at many telescope facilities. At the difference of the devices described in the remaining of this section, flat field screens are not build to characterize the passbands, but to map the uniformity of the imager focal plane. We have seen in §2.4.1 that determining the response of a wide field imager is not a trivial problem, and groups are thinking about deriving the response map of wide field imagers from such artificial sources.

A recent implementation of a flat field dome screen is described in (Marshall and DePoy, 2005). The apparatus is installed in the enclosure of the McGraw-Hill 1.3 m telescope at the MDM Observatory. It is made of a series of narrow spectrum LEDs of various colors, mounted on the telescope spider, and illuminating a high uniformity screen that injects the light into the telescope pupil. The main purpose of this system is to generate high signal to noise flat fields that nearly match the colors of the science objects, and not to perform a flux calibration of the telescope passbands. Interestingly, the authors note many effects that will be discussed below. They observe diffraction patterns in their flat-fields, probably due to dust or optical defects. Also they observe that the response of their instrument after flat-fielding is not uniform, probably due to flatfield pollution by ghosts.

The Response functions of the SDSS The system described by Doi et al. (2010) and installed on the SDSS 2.5-m telescope at the Apache Point Observatory (New Mexico) is more ambitious. Its main purpose is to measure *in situ* the imager passbands, and to monitor them over the life of the survey. The light source is a lamp, coupled to a monochromator and an integrating sphere. It generates a nearly flat, quasi monochromatic calibration beam that can cover almost entirely one of the imager CCD. The flux delivered by the source is monitored in real time by a Hamamatsu S2281 photodiode, calibrated at a Japanese Institute of Standards (*Japan Quality Insurance*). The light source does not illuminate the primary mirror of the telescope. It is rather inserted into the optics, as close a possible to the cryostat window. Several measurement campaigns were carried out, to measure the SDSS passbands, as well as the passbands of the auxiliary Photometric Telescope (PT) used to calibrate the main survey. In wavelength, the uncertainty is dominated by the monochromator repeatability (± 3Å which averages out well) and by uncertainties related to the fact that the system does not reproduce the exact beam geometry and incident angle distribution ($\lesssim 5$Å).

The system allowed the detection of significant variations of the passband fronts, affecting the PT, as a function of temperature and hygrometry, as well as a slow degradation of the main imager response in the u-band. As shown above, such response drifts are difficult to detect with standard star observations, and can bias significantly the supernova luminosity distances. The work of Doi et al. (2010) demonstrates that telescope passbands are not as stable as one may thing and can be affected by significant ageing. Hence, a regular *in situ* precision monitoring of the telescope response must be implemented if one seeks to do precision cosmology with the instrument.

Flux calibration of ESSENCE and PanSTARRS Stubbs et al. (2010, 2007b) describe another design whose goal is not only to measure precisely the passband fronts, but also to measure the full-aperture system throughput. The apparatus comprises a large transmissive flat field screen, fed by a tunable laser, monitored in real time by a Hamamatsu 2281 Si photodiode, calibrated at NIST. The (monochromatic) calibration light illuminates the full aperture of the telescope, generating a nearly flat illumination on the focal plane. The comparison of the photodiode current and the flux registered on the focal plane should in principle yield a precise measurement of the normalized instrument transmissions.

Demonstrators were installed first at the Blanco 4-m telescope (Cerro-Tololo Inter American Observatory) to calibrate the 0.36 deg^2 Mosaic-II imager, and then at the PanSTARRS telescope (Haleakala, Maui, Hawaii) to calibrate the 3-deg^2 Gigapixel imager. The authors are able to obtain normalized transmission functions. The wavelength uncertainties affecting the filter fronts are of about 2Å, which is well within the specifications for current Dark Energy studies (see figure 2.4). In flux, however they note significant discrepancies ($\sim 5\%$, wavelength-dependent) between their instrumental flux calibration (folding in the atmosphere) and the calibration they could derive from observations of spectrophotometric standards. They attribute this to several effects that dominate their systematics error budget. Among those, the screen non-uniformities ($\sim 5\%$) and the pollution of the calibration frames by stray light (another 5%).

The number of photometric calibration projects underway is quite long. The field is relatively new, and many groups are coming up with innovative design ideas. One could mention for example the DECCal system (Rheault et al., 2010) built for the Dark Energy Camera (screen illuminated by a monochromatic LED source), the ALTAIR project (Albert et al., 2012) (balloon borne source, to emulate an artificial star) and many others. Although one can be sure that the next generation telescopes contributing to Dark Energy Science will all be equipped with at least one calibration system, it is relatively difficult to predict the system that will emerge from this design competition.

3.4 DICE: Design Considerations

We now turn to the description of the DICE system. DICE (Direct Illumination Calibration Experiment) was proposed a few years ago by a team of LPNHE scientists and engineers (Barrelet and Juramy, 2008). A first demonstrator (SnDICE) was built and installed in the enclosure of the Canada-France-Hawaii Telescope (CFHT). The main goal was to identify the difficulties that inevitably arise when testing a new design. We also had the objective of quantifying the accuracy of the calibration that may be obtained, and demonstrate the technique on real data. Two years later, a second generation instrument, codenamed SkyDICE, was built and installed at Siding Springs Observatory (NSW, Australia) to calibrate the 5.7 deg^2 SkyMapper imager (Keller et al., 2007). We design was slightly updated, building on the lessons learned with the first demonstrator.

The DICE system was designed with several potential applications in mind. One objective was to build a very stable source, that could be used to monitor the imager characteristics over various time scales. Among the things to monitor are the hourly imager gain variations, and potential secular variations of the imager passbands. Another potential application was flat-fielding of wide field imagers. The last, long term project was flux calibration, the question being: how accurately can we transfer the calibration carried by a NIST photodiode to a wide field imager ?

3.4.1 Calibration beam

Ideally, a photometric calibration device should mimic as much as possible the science objects under study. Since a supernova survey is dealing primarily with point sources (supernovae and field stars), we should try and generate quasi-parallel beams, covering the entirety of the primary mirror (see figure 3.2). Such a beam would result in a spot on the focal plane, and we could use the photometry code in production in the survey photometry pipeline to estimate its flux, thereby avoiding the systematic errors that arise from using different flux estimators.

Unfortunately, building a good artificial star turns out to be difficult. For SnDICE, we deliberately opted for a different design, (figure 3.2). SnDICE is a point source, located in the dome, a few meters away from the telescope primary mirror, close to the object plane. The source generates a conical, quasi-lambertian beam, of aperture $\sim 2^o$, slightly larger than the telescope angular acceptance. Such an illumination results in an almost uniform focal plane illumination.

As shown on figure (3.2), the calibration beam is radically different from the science beam. In particular, the angular distribution of the light rays that hit the various optical surfaces (e.g. the interference filters) is not comparable. However, this specific calibration beam has at least one very nice property: it is much simpler than the science beam, in the sense that each pixel sees photons that came through a unique path. In other terms, there is a one-to-one relationship between the focal plane elementary surface elements and the calibration beam elementary solid angles. As we will see, such

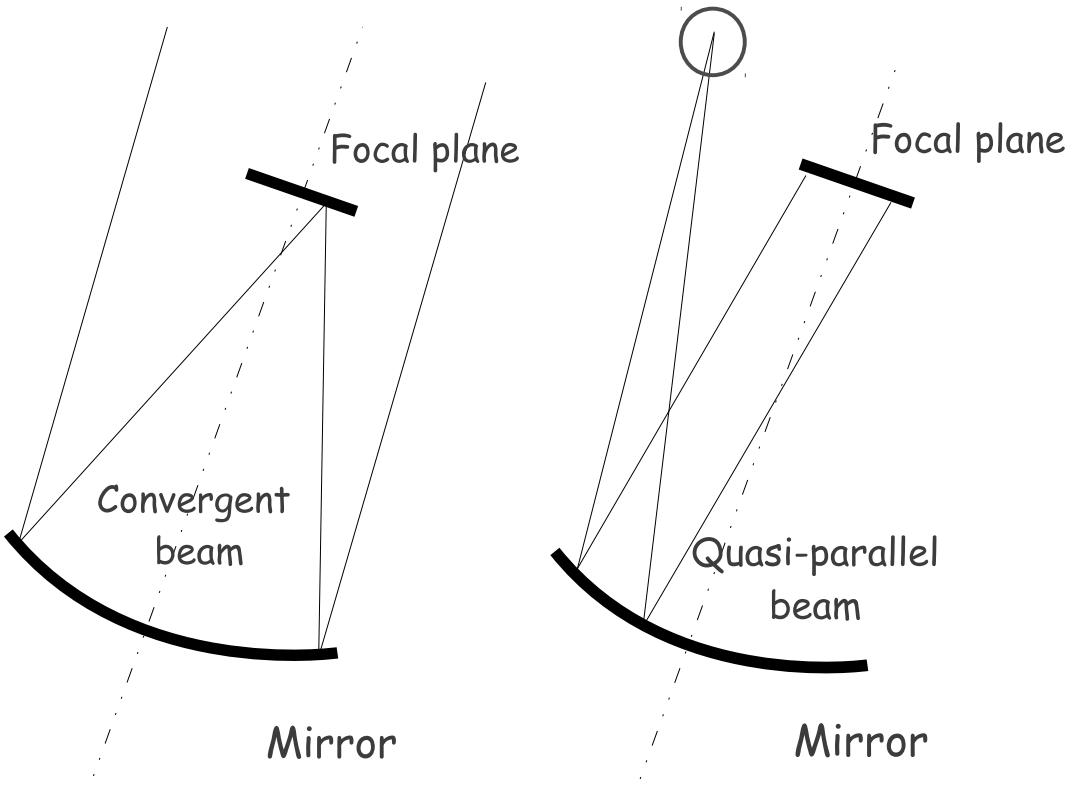

(a) science beam (b) DICE beam

Figure 3.2: Left: telescope illumination by a point source ("science beam"). Right: SnDICE calibration beam.

a property makes it very simple to predict the focal plane illumination, once one knows the beam radiant intensity map. Another advantage of this kind of illumination pattern is that it should allow in principle to derive photometric flat fields.

Unfortunately, these two nice properties come at a price. First, with a point source emitter, we expect to see diffraction patterns, generated by dust and optical defects in the telescope optics. This is the case, as seen on the three SnDICE calibration frames shown on figure (3.3). On every single calibration frame, every single pixel is affected by the effect. However, these patterns average well on scales of $\sim$ 100 pixels. Hence, diffraction patterns do not keep us from determining a calibration solution at those scales.

There is a second problem, that affects not only DICE, but in fact all the calibration systems that illuminate directly the primary mirror. This problem is the pollution of the calibration frames by internal reflections (ghosts). The intensity of ghosts depends on the reflectivity of the optical surfaces along the light path. In a modern telescope, there are at least two surfaces which are quite reflective at some wavelengths: the filters,

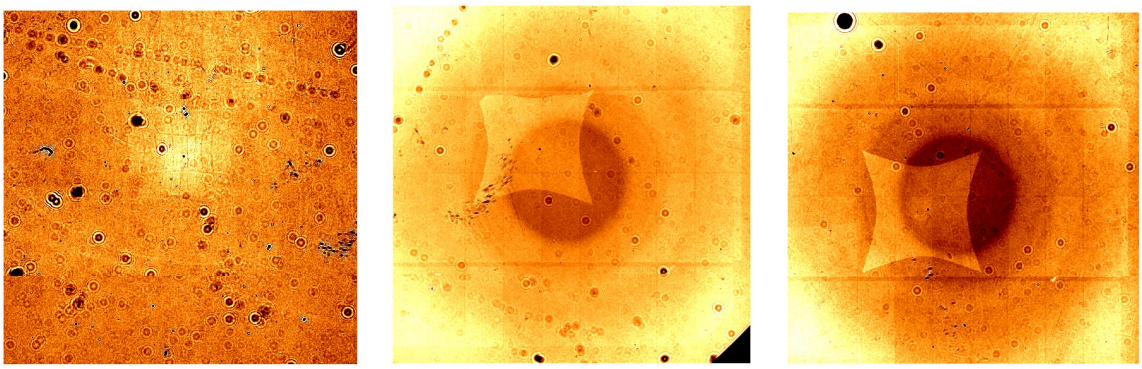

(a) LED GD8 No filter (b) LED GD8 (r band) (c) LED GD4 (r band)

Figure 3.3: SnDICE/MegaCam calibration frames, with and without filters, at two different wavelengths.

generally implemented as interference filters, and the CCDs. The CCD reflectivity is of 5-10% at least. The filter reflectivity may be much higher, in particular in the cut-off regions.

In addition, wide field imagers are all equipped with a wide-field-corrector (WFC) comprising three to four lenses. This is necessary because on most telescopes, the mirror alone cannot deliver a uniform image quality on the entire field of view. All these lenses have been coated in order to minimize their reflectivity. They nevertheless display residual reflectivities of the order of 1-2%. The net result is that we expect to see a complicated ghosting pattern on the calibration frames. Figure (3.3) shows examples of these ghosts. Their relative intensity depends on the wavelength and on the focal plane position. It is of a few percents when the filter transmission is maximal (or when no filter is inserted in the optical path), and it can reach $\sim 20\%$ in the filter cut-off regions.

We must insist on the fact that ghosts affect all calibration experiments. Ghosts will not cause discontinuities in the image if one uses an extended source, a flat field screen for example, but the pollution will still be there. Our bet is that since the ghosts are clearly visible with our beam geometry, their intensity can be modeled with a simulation of the imager optics and accounted for.

3.4.2 Light emitters

Another important design element is the choice of narrow-spectrum light emitting diodes (LED) as light emitters. LEDs are known to be extremely stable, as long as they are fed with stable currents. It it is relatively easy today to build current sources stable at a few 10^{-5} over a temperature range of a few degrees. Hence, with some care, it is relatively easy to build a light source that can deliver very stable beams over long durations. The

diversity of narrow-spectrum LEDs available on the market permits to cover the entire spectral range of silicon imagers, from the near UV to the near infrared (see figure **??**).

LED do not emit monochromatic light. The width of typical LED spectra is of about $\delta\lambda/\lambda \sim 5-7\%$. Hence, as always, there is a trade-off, as we chose to sacrifice wavelength precision in favor of high-quality and high-stability illumination. This makes sense, since what one actually needs is a *follow-up* more than a *measurement* of the filter cutoff positions. The filter transmissions are indeed well measured prior to installation.

LEDs come with just one caveat: their emission properties vary with temperature. As temperature increases, the LED emission efficiency drops by up to 0.5% / ° C, and the mean wavelength of the emitted light shifts redwards by about 0.1 Å/ ° C. These variations are generally linear and always extremely reproducible. As a consequence, once each emitter has been well characterized, one only needs to implement a real time follow-up of the source temperature to account for these effects.

3.4.3 Direct Illumination

A last very important design point is that a calibration source should be as simple as possible. In particular, we have deliberately avoided to introduce intermediate optical surfaces between the light emitters and the primary mirror, such as optical fibers, folding mirrors and the like. Indeed, any additional optical element is subject to ageing, hence, has to be characterized and monitored. Of course, it is always possible to monitor the beam in real time, and measure with a photodiode, for each calibration exposure, the total illumination delivered to the instrument. We have decided instead to build an instrument that is intrinsically stable, and to rely on monitoring only to detect potential (unexpected) variations of the calibration source.

The DICE sources are direct illumination systems: there is nothing but free space between the light emitters and the telescope primary mirror. As a consequence, if the beam is known at a certain distance from the source, the illumination on the primary mirror can be safely extrapolated with elementary geometry. One just needs to know precisely the relative positions of the source and the telescope.

3.5 The DICE System

3.5.1 Light Source

The SnDICE light source is a 130mm×130mm×300mm box, pierced with 25 asymmetric holes. It contains 24 calibration LEDs mounted on a radiator, located on the back of the device, approximately 260 mm from the front face (figures 3.4 & 3.5(a)). The light beams exit through circular apertures of diameter 9-mm. The beams are carefully shaped using a series of masks designed to kill most of the stray light. Off-axis control photodiodes[6],

[6] 5.8 mm × 5.8 mm Centronic4 OSD35-7

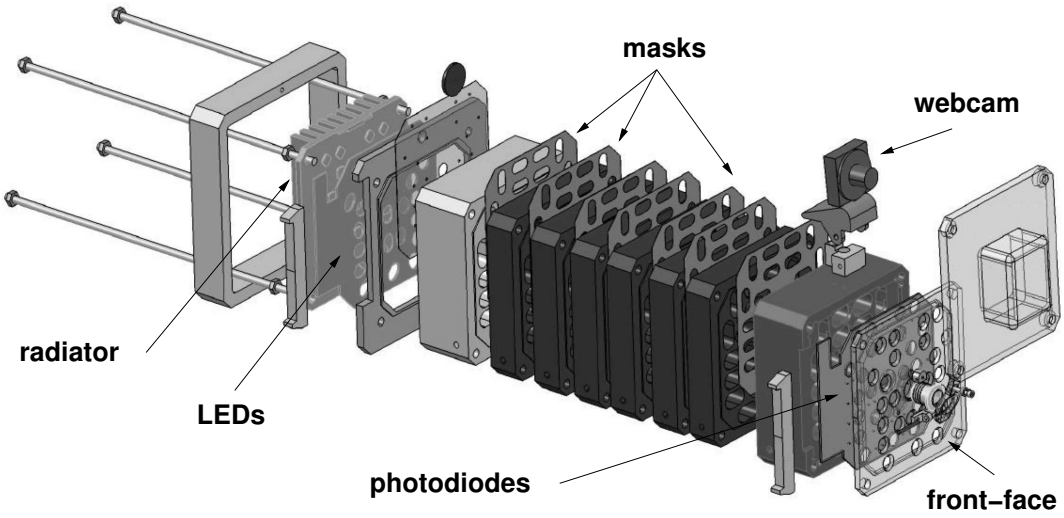

Figure 3.4: Sketch of the DICE light source. It consists in a modular box, made of 8 (almost) identical aluminum pieces. pierced with holes to let the light through. The LEDs are mounted on a radiator, on the back of the device. Close to the front face, control photodiodes (one for each calibration channel) monitor the light delivered by the LEDs.

located close to the front face, monitor in real time the light delivered by each LED. The mechanical design of SkyDICE, the demonstrator installed in the SkyMapper enclosure, is almost identical, except that the LED head is shorter, in order to generate wider (3 degree) conical beams.

Figures 3.5(b) & 3.6 show the quality of the spectral coverage obtained for SnDICE and SkyDICE. The LEDs have been chosen so that each filter is sampled by at least three LEDs: one close to the maximum, and two covering the filter cutoffs. The diversity of LEDs available in 2007, at the time SnDICE was designed, does allow to sample well the red cutoff of the MegaCam r filter, as well as the blue cutoff of the i-filter. Also, few LEDs were available in the infrared. Two years later, the diversity of LEDs had dramatically improved, and the spectral coverage provided by SkyDICE is excellent.

The DICE system is designed to deliver very stable beams over long durations. The LEDs are operated at very low currents and should not be subject to significant evolution. Also, there are no intermediate optical surfaces between the emitters and the telescope primary mirror –besides the LED encapsulant. This limits the effect of optical surface ageing. Finally, a set of redundant controls has been implemented: the LED currents and temperatures are monitored in real time, the LED flux is also measured by control photodiodes. Finally, cooled, large area control photodiodes, designed to sense the typical low focal plane illuminations, of a fraction of nW / cm^{-2}, are placed on the telescope, and provide and additional, independant measurement of the calibration flux

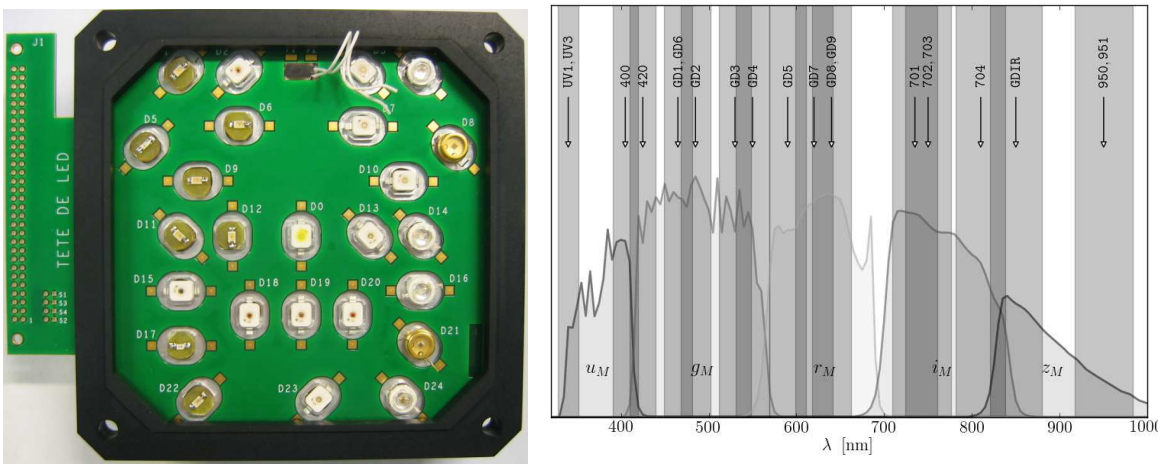

(a) SnDICE LED board

(b) Filter coverage

Figure 3.5: The SNDice LEDs mounted on their front-end board. The characteristics of all LEDs are summarized in table 3.1. The central LED is used to generate the planet beam. Most LEDs are flat top, hence almost perfect lambertian emitters. The flat-top LEDs mounted in a white packaging are the high-intensity OSRAM Golden Dragon®, which cover the wavelength range 450 nm $< \lambda <$ 750 nm. The remaining slots host lower intensity LEDs purchased from OSRAM and Marubeni. They cover the redder wavelength range.

delivered by the source.

3.5.2 Backend Electronics

The intensity of the light emitted by each LED is a linear function of the current injected into it, with a precision of 10^{-5}. The LED currents are generated (and monitored in real time) by a custom made backend board connected to the illumination system with an analog link. We have attempted to build a current source that achieves an electric stability of a few 10^{-4} over a temperature range of a few degrees. It is is classically implemented as a transistor current source driven by a programmable voltage level, and stabilized with a negative feedback loop. For redundancy, the feedback voltage level is also sampled at a rate of a few kHz by a LTC1608 16 bit ADC, and registered for offline checks.

3.5.3 Alignment Beam

The source can be oriented using an altitude and an azimuth motor. By moving simultaneously the LED head and the telescope, one is able to scan various locations

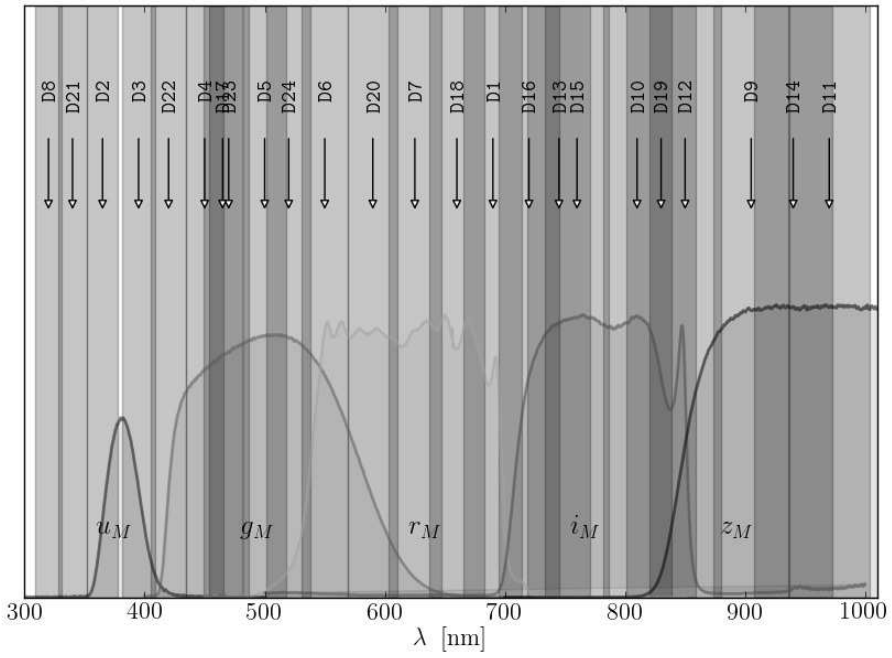

Figure 3.6: Coverage of the SkyMapper passbands by SkyDICE.

of the primary mirror, keeping both instruments aligned. A 25th LED called the *artificial planet* is used to control the relative alignment of SnDICE with the telescope. This channel is equipped with a convergent lens that reshapes the light into a (quasi) pencil-beam. In order to reduce the spatial extension of the LED emission zone, and improve the quality of the pencil beam, a 50µm hole is placed in front of the LED.. Planet exposures display a bright ($\sim$ 100 pixel wide) spot, along with a series of *ghosts* generated by reflexions within the telescope optics. The position of the main spot is a direct measurement of the relative orientation of the planet beam and the telescope optical axis. The relative positions of the ghosts encode information on (1) the distance between the planet beam and the telescope optical axis and (2) the alignment of the telescope optics –the WFC lenses, in particular.

3.5.4 Operations

The CFHT enclosure in sufficiently light-tight to permit SnDICE operations during day time. During a typical data taking session, the dome aperture tracking system is disconnected and the telescope points inside the dome towards the source. At CFHT, the source is mounted on the rotating part of the dome. Since the dome orientation accuracy is of a few 0.1° only, the relative alignment and positions of both instruments are first controlled with a series of alignment exposures taken with the *planet* beam.

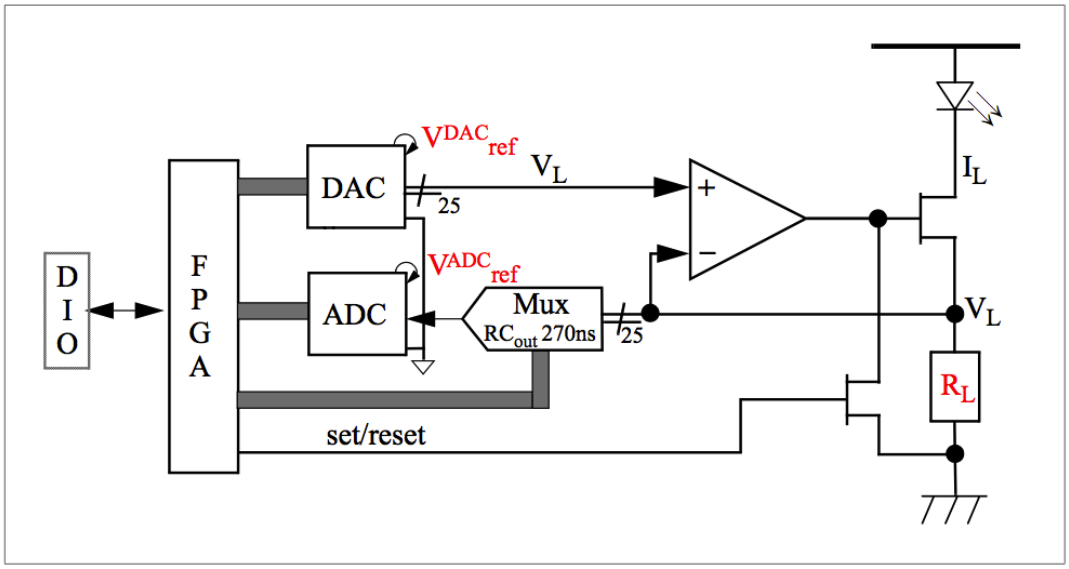

Figure 3.7: LED current generation and monitoring.

Then, sequences of calibration exposures are taken. The source and the telescope are then moved, in order to cover a different mirror area, and the same calibration sequence is repeated. Some calibration sequences are designed to test the repeatability of the readout electronics. They consists in up to 50 exposures taken with the same LED, at regular intervals. The source itself being very stable –and monitored– this allows one to study potential variations of the imager gains over time. Other calibration sequences consists in series of exposures taken with different LEDs, with and without filter. Such a dataset permits to monitor the telescope transmissions – filter normalization and filter cutoffs.

3.6 Test Bench Studies

Prior to installation, the light source must be characterized on a spectrophotometric test bench. The goal is (1) to measure the spectral energy distribution of each LED, as a fonction of temperature and (2) to map the beam radiant intensity (in W / sr) – also at various temperatures. All measurements are performed for several values of the LED currents, although, in operations, we try not to vary the LED currents. Instead, we adapt the total illumination delivered to the focal plane by varying the exposure time. The nominal current was adapted for each LED, in order to yield a few thousand photoelectrons per pixel and per second on the focal plane.

The test bench studies are described in detail in (Guyonnet, 2012) and in a forthcoming paper. In what follows, we present the main points. The test bench is placed in a

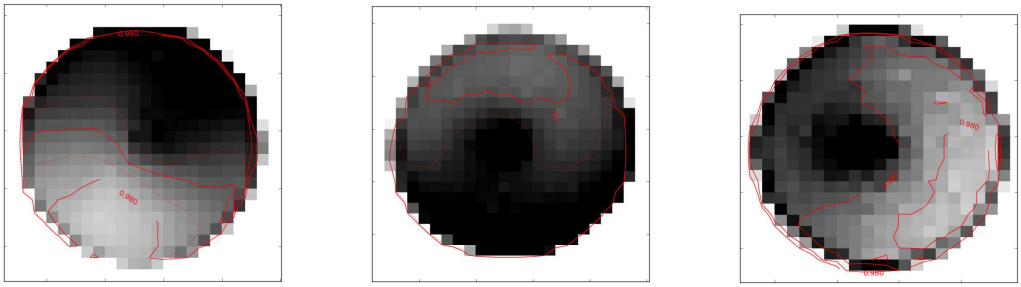

(a) (b) (c)

Figure 3.8: Map of the radiant intensity delivered by three different LEDs, in the blue, green and near UV. The diameter of each beam is of 2 degrees. The non-uniformities shown on the map are of about 1% (peak-to-trough)

2m × 2m × 3.5m dark enclosure. The enclosure walls are thermally insulated, and its temperature can be regulated from 0°C (typical temperature on site) to 25° C. The bench is not strictly speaking thermalized, as significant temperature gradients can still be measured after a few hours of operations. However, the temperature of all bench elements is monitored using PT1000 thermistors.

The flux measurements are all performed with a calibrated photodiode, purchased from an institute of standards. A very common choice is the 1 cm^2 Hamamatsu 2281, calibrated at the National Institute of Standards and Technology (NIST). Following the recommandations of NIST, it is operated at ambiant temperature, in photoeletric mode (not polarized in reverse) and read out using a Keithley 6514 feedback picoammeter. The fluxes measured by the photodiode are of a few nanowatts, yielding photodiode currents of a few nanoamperes (the fluxes recorded by the imager focal plane are about 50 times lower).

The bench operations are fully automated. The LED head and the calibrated photodiode are both mounted on computer controlled linear tables.

3.6.1 Photometric characterization: beam maps

By moving the photodiode in a plane orthogonal to the head $Z-$axis one can map the beam radiant intensities. Figure 3.8 shows three different maps. The beams are not perfectly lambertian, but display small non-uniformities at the level of about 1%. The origin of those non-uniformities, in particular of the central "bump" is unknown. However, they are extremely well measured, with a relative precision of a few 0.01% and do not seem to vary. The average radiant intensity emitted by each LED at nominal current is summarized in table 3.1.

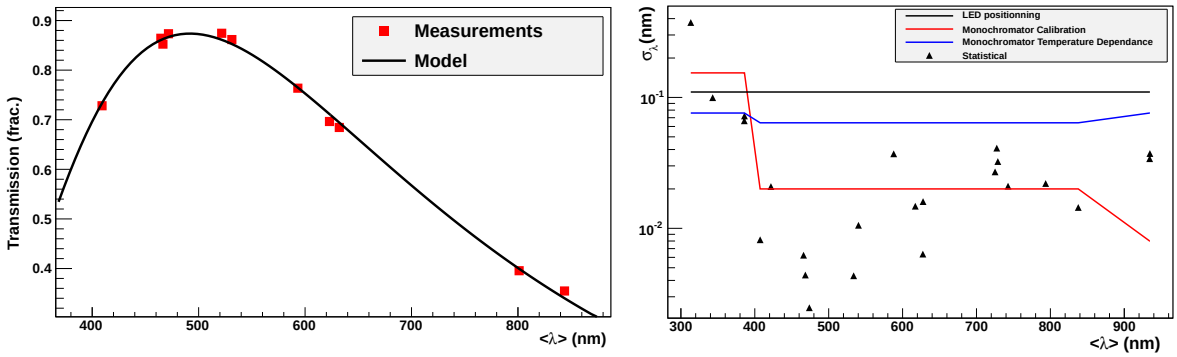

(a) Monochromator transmission

(b) Uncertainties in wavelength

Figure 3.9: Spectral test bench. Left: re-determination of the monochromator transmission (measurements + fitted model). Right: Uncertainties in wavelength. The dominant contribution ($\sim$ 1Å) comes from the uncertain positioning of the calibration source with respect to the monochromator entry slit.

The variations of the intensity delivered by each SnDICE LEDs as a function of temperature have been measured over the 0°C $< T <$ 25°C range (see coefficients in table 3.1). They have been found extremely reproducible over time. For all LEDs except one, the flux *decreases* with T. For all LEDs except two, the flux varies linearly as a function of temperature. These temperature effects are significant (from 0.2 to 2% / °C) and must be accounted for. However, they are also extremely well characterized, hence, as long as temperature is measured, they do not induce any significant uncertainty.

3.6.2 Stability

The stability of SnDICE has been studied on the test bench, of typical durations of $\sim$ 2 weeks. Most LEDs display relative stabilities of a few 10^{-4}, except in the near-UV, where two LEDs seem to show a small variability of about 1%. This effect is not well understood yet and is being investigated using a spare device.

The stability of the maps have also been studied. All maps have been found to be extremely stable, with typical variabilities of 10^{-4} or less.

3.6.3 LED spectra

By placing a monochromator (a Digikröm DK240) between the source and the calibrated photodiode one can measure the spectrum of each LED. To do this, the wavelength calibration of the monochromator has to be performed several times over the full temperature range, using Cd and Hg lamps, as small but significant variations of the

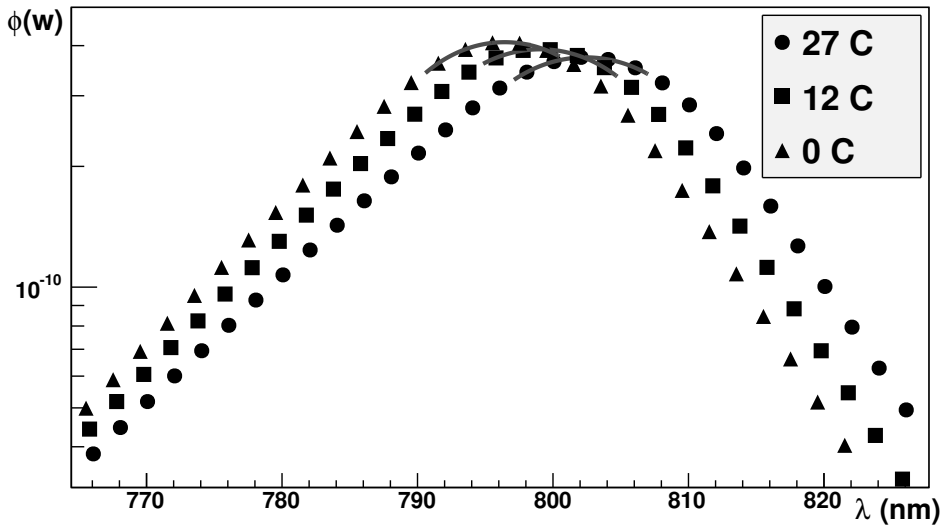

Figure 3.10: Three spectra of the same LED (810 nm), taken at three different temperatures.

instrument response with temperature have been found. Taking this into account, the total wavelength uncertainty is of about 1Å, as illustrated on figure (3.9(b)).

It is essential in these measurements, to control also the transmission of the monochromator, as it has an impact on the shape of the measured LED spectra. As often, the absolute normalization of the transmission does not matter, since the spectra are normalized using the beam maps, measured without monochromator. They are measured using a ⌀0.8-mm pencil beam, narrow enough to be totally enclosed in the monochromator entrance slit. Measuring the beam intensity with and without the monochromator yields a measurement of the transmission, as illustrated in figure (3.9(a)).

Figure 3.10 shows a typical LED spectrum at three different temperatures. The behavior described in §3.4 is clearly apparent: as temperature decreases, the flux increases and the spectrum is blueshifted. Also, the shapes of the spectra seem to change slightly with temperature.

To fix ideas, we have quantified the variations of the each spectrum's average temperature as a function of T. As for the fluxes, these variations were found to be almost linear. Once again, they are significant (up to 1Å/°C) and must be accounted for. However, they were found to be extremely reproducible. Hence, with an appropriate temperature monitoring, the temperature variability of LEDs does not introduce significant additional uncertainties.

model	type	i_{LED} (mA)	i_{max} (mA)	$\langle\lambda\rangle$ (@ 25 °C) (nm)	$d\lambda/dT$ (nm/°C)	radiant intensity (@ 25 °C) (mW/sr)	$d\Phi/(\Phi dT)$ (%/°C)	channel
ZWW5SG‡	flat top	30	500	–				D0
S8D31C⊙	hemispheric	15	20	312.504 ± 0.777	-0.035 ± 0.027	0.02181 ± 0.00021	-2.2129 ± 0.0053	D4
S8D34C⊙	hemispheric	15	20	342.337 ± 0.214	-0.027 ± 0.008	0.01885 ± 0.00003	-2.1448 ± 0.0101	D24
T9F34C⊙	flat top (window)	15	20	387.475 ± 0.150	$+0.059 \pm 0.005$	0.01072 ± 0.00002	-3.0912 ± 0.0166	D21
T9F31C⊙	flat top (window)	15	20	387.96 ± 0.142	$+0.086 \pm 0.005$	0.01539 ± 0.00001	-2.1406 ± 0.0050	D8
S8D40⊙	hemispheric	17.5	350	407.963 ± 0.015	$+0.029 \pm 0.001$	0.49891 ± 0.00018	-0.4522 ± 0.0033	D14
S8D42⊙	hemispheric	17.5	350	422.217 ± 0.048	$+0.015 \pm 0.002$	0.20007 ± 0.00019	0.1983 ± 0.0025	D16
LBW5SG‡	flat top	25	500	466.417 ± 0.013	$+0.017 \pm 0.0005$	0.23207 ± 0.00012	-0.2156 ± 0.0005	D10
LBW5SG‡	flat top	25	500	468.669 ± 0.012	$+0.010 \pm 0.0004$	0.33045 ± 0.00016	-0.2153 ± 0.0016	D23
LBW5SM‡	flat top	25	500	474.258 ± 0.005	$+0.018 \pm 0.0002$	0.65071 ± 0.00055	-0.2241 ± 0.0007	D3
LTW5SG‡	flat top	25	500	533.471 ± 0.010	-0.012 ± 0.0004	0.12352 ± 0.00003	-0.1301 ± 0.0005	D13
LTW5SM‡	flat top	25	500	540.637 ± 0.026	$+0.014 \pm 0.001$	0.31282 ± 0.00023	-0.5900 ± 0.0013	D7
LYW5SM‡	flat top	25	500	590.588 ± 0.086	$+0.105 \pm 0.003$	0.05893 ± 0.00006	-0.3915 ± 0.0022	D20
LAW5SM‡	flat top	25	500	620.216 ± 0.033	$+0.121 \pm 0.001$	–	-0.4485 ± 0.011	D19
LRW5SM‡	flat top	25	500	630.289 ± 0.013	$+0.114 \pm 0.0005$	0.38592 ± 0.00029	-0.2303 ± 0.0005	D2
LRW5SM‡	flat top	25	500	630.632 ± 0.027	$+0.117 \pm 0.001$	0.36542 ± 0.00017	-0.3644 ± 0.0021	D18
SMC750⋆	flat top	30	50	729.395 ± 0.059	$+0.170 \pm 0.002$	0.23181 ± 0.00018	-0.8754 ± 0.0013	D22
SMC735⋆	flat top	30	50	731.755 ± 0.090	$+0.172 \pm 0.003$	0.23947 ± 0.00028	-0.4147 ± 0.0008	D12
SMC735⋆	flat top	25	500	733.087 ± 0.070	$+0.168 \pm 0.003$	–	-0.4489 ± 0.0007	D6†
SMC750⋆	flat top	30	50	746.792 ± 0.047	$+0.163 \pm 0.002$	0.29190 ± 0.00003	-0.2369 ± 0.0009	D9
SMC810⋆	flat top	30	50	798.414 ± 0.048	$+0.192 \pm 0.002$	–	-0.2404 ± 0.0019	D1
SMC810⋆	flat top	30	50	–	–	–	–	D11†
SFH 4230‡	flat top	25	1000	843.315 ± 0.029	$+0.223 \pm 0.001$	0.37082 ± 0.00037	-0.1613 ± 0.0008	D15
SFH 4203⋈	flat top	75	100	942.371 ± 0.080	$+0.308 \pm 0.003$	0.69169 ± 0.00091	-0.2485 ± 0.0050	D17
SFH 4203⋈	flat top	75	100	941.399 ± 0.073	$+0.282 \pm 0.003$	0.74315 ± 0.00118	-0.5340 ± 0.0020	D5

Table 3.1: Summary of the SNDice LED characteristics.

⊙ Seoul Semiconductor Co., Ltd – `http://www.acriche.com`

‡ Golden Dragon® LED, OSRAM Opto Semiconductors GmbH – `http://www.osram-os.com/osram_os`

⋆ Marubeni – `http://tech-led.com`

⋈ OSRAM Opto Semiconductors GmbH – `http://www.osram-os.com/osram_os`

† dead channel

3.7 Analysis of the DICE calibration frames

The analysis of the SnDICE dataset is detailed in (Guyonnet, 2012; Villa, 2012). It is very well advanced, however it has not been finalized yet. The main difficulty is the modeling of the ghost contamination, which is still too uncertain for our accuracy goals. As described above, ghosts generate a complicated contamination pattern whose intensity varies as a function of wavelength. In particular, this contamination is highest for the LEDs which coincide with the filter fronts. This is problematic, since we are precisely trying to measure these fronts.

After a series of unsuccessful attempts, we have decided to model the ghost contamination by building a simulation of the optical system (see figure 3.11). As there are slight uncertainties on the geometrical position of the source with respect to the telescope, the simulation is tuned on the alignment data: for each alignment image, taken by illuminating the telescope with the DICE *planet* beam, we compare the actual position of the ghosts with the positions of the same ghosts predicted by the model. The exact orientation and position of the telescope and source are determined from these data with a least square fit.

Direct Light Once this is done, we are in a situation to predict the positions and intensities of all the ghosts, for any given exposure. This is not even computer intensive, thanks to the very specific geometry of the beam. Indeed, since there is a one-to-one relationship between the elementary solid angles on the beam, and the focal plane surface elements, one can show that the irradiance $\mathcal{I}$ at position $\boldsymbol{x}$ on the focal plane is given by:

$$\mathcal{I}(\boldsymbol{x}) = \int T(\lambda; \boldsymbol{x}, \boldsymbol{v})\ \mathcal{S}(\lambda; \boldsymbol{u})\ \left|\frac{\partial \boldsymbol{u}}{\partial \boldsymbol{x}}\right|\ d\lambda \tag{3.1}$$

where $\mathcal{S}(\lambda; \boldsymbol{v})$ is the LED spectrum along direction $\boldsymbol{u}$, $T(\lambda, \boldsymbol{x}, \boldsymbol{v})$ is the instrument transmission for pixel $\boldsymbol{x}$ and orientation $\boldsymbol{v}$ with respect to the filter normal. Note that $\boldsymbol{v}$ is a function of $\boldsymbol{u}$ and of the relative position of DICE and the telescope. Finally, the jacobian $|\partial \boldsymbol{u}/\partial \boldsymbol{x}|$ accounts for the variations of the solid angle subtended by each pixel. We may neglect the chromaticity of the optics over the extension of the LED spectrum. This is a reasonable approximation, since we are only interested in large scale effects. This allows us to move the jacobian out of the integral. We may also define the average transmission of the instrument, $\hat{T}(\boldsymbol{x})$ as:

$$\int T(\lambda; \boldsymbol{x}, \boldsymbol{v})\ \mathcal{S}(\lambda; \boldsymbol{u})\ d\lambda = \hat{T}(\boldsymbol{x}) \times \mathcal{B}(\boldsymbol{u}) \tag{3.2}$$

where $\mathcal{B}(\boldsymbol{u})$ is the beam radiant intensity emitted in direction $\boldsymbol{u}$. Equation (3.1) then becomes:

$$\mathcal{I}(\boldsymbol{x}) = \hat{T}(\boldsymbol{x}, \boldsymbol{v})\ \mathcal{B}(\boldsymbol{u}) \left|\frac{\partial \boldsymbol{u}}{\partial \boldsymbol{x}}\right| \tag{3.3}$$

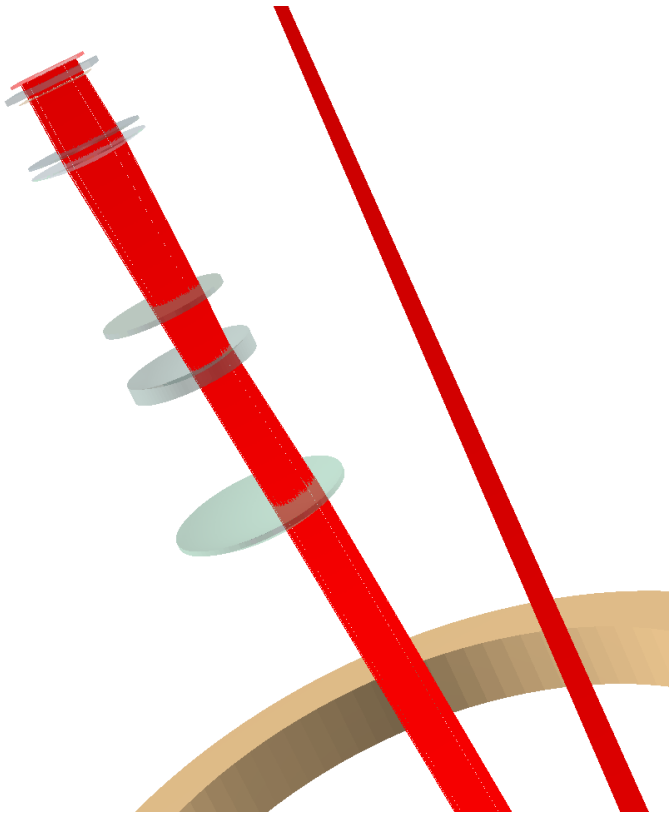

Figure 3.11: Optical simulation of MegaPrime optical system (zoom on the wide field corrector).

The flux recorded at position $\boldsymbol{x}$ can be expressed as the product of three components: the average transmission of the instrument (which is what we want to measure), the beam radiant intensity in direction $\boldsymbol{u}$ which corresponds to position $\boldsymbol{x}$, and finally, a jacobian term that accounts for the solid angle subtended by the pixel.

Ghosts The equation above only holds for direct light. Let's consider instead a path, labeled p, and involving two or more reflections within the optics. For example, the light that bounces off the filter, and then off the L4 lens before hitting the focal plane. One finds that for this path also, there is a one-to-one function $\mathcal{R}_p$ mapping the emission directions $\boldsymbol{u}$ to the resulting focal plane coordinates $\boldsymbol{x}_{|p}$:

$$\mathcal{R}_p : \boldsymbol{u} \mapsto \boldsymbol{x}_{|p} \qquad \mathcal{R}_p^{-1} : \boldsymbol{x} \mapsto \boldsymbol{u}_{|p} \tag{3.4}$$

Equation 3.3 must be modified as follows:

$$\mathcal{I}_p(\boldsymbol{x}) = \hat{T}_p(\boldsymbol{x}, \boldsymbol{v})\ \mathcal{B}(\boldsymbol{u}_{|p}) \left| \frac{\partial \boldsymbol{u}_{|p}}{\partial \boldsymbol{x}} \right| \tag{3.5}$$

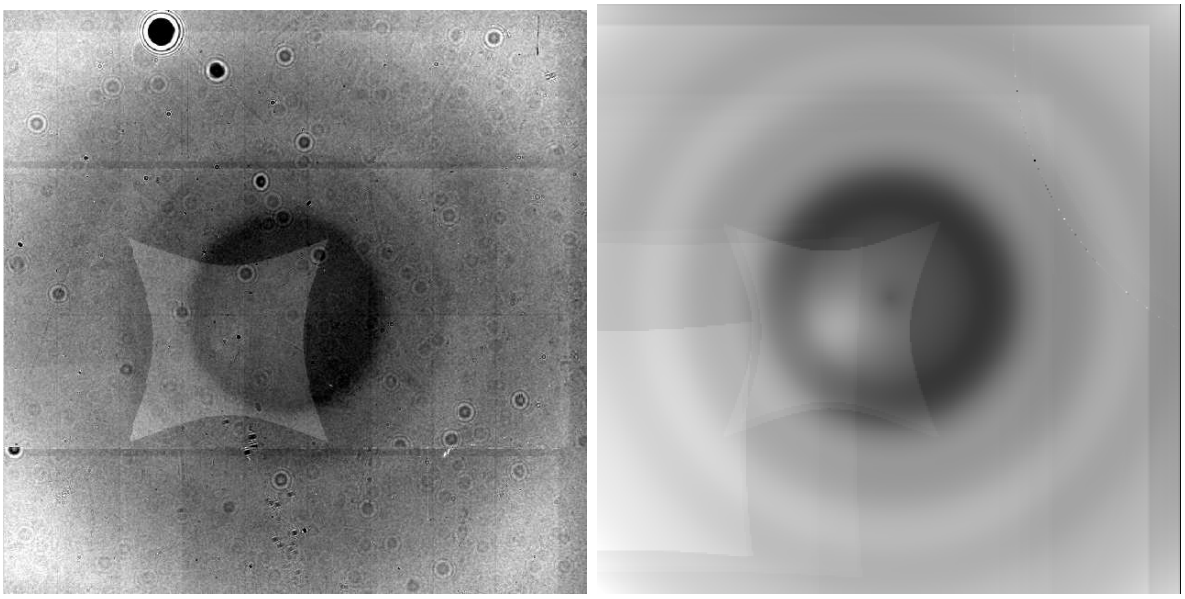

(a) r band image (b) image model (direct light + ghosts)

Figure 3.12: Left: MegaCam/SnDICE calibration frame, taken in the r band, with a LED that covers the filter front. The ghosts are clearly apparent. In particular, we clearly see the reflection of the focal plane CCDs on the filter and the cryostat window. Right: model of the same exposure, computed with the MegaCam optical simulation. The reflectivity of some lenses has been slighly increased, so that the fainter ghosts can be clearly seen.

$\hat{T}_p(\boldsymbol{x}, \boldsymbol{v})$ is the effective transmission of the instrument for path p: it is simply the product of the transmission and/or reflectivities of the optical surfaces located along this same p-th path.

Finally, the total flux recorded on the focal plane is obtained by summing over all the contributions, with the convention that $p = 0$ for the direct light:

$$\mathcal{I}(\boldsymbol{x}) = \sum_p \hat{T}_p(\boldsymbol{x}, \boldsymbol{v})\ \mathcal{B}(\boldsymbol{u}_{|p})\ \left|\frac{\partial \boldsymbol{u}_{|p}}{\partial \boldsymbol{x}}\right| \tag{3.6}$$

The radiant intensities $\mathcal{B}$ of all beams are already known from test bench measurements. The functions $\boldsymbol{x} \mapsto \boldsymbol{u}_{|p}$ and their jacobians can be computed with the simple optical model of the instrument. Finally, the transmissions T_p (our unknowns) are not independant: they are the products of the transmissions and reflectivities of about ten optical elements. We know that the filter transmissions and reflectivities exhibit a radial pattern. This allows us to parametrize them as 2D functions (one variable for the radius w.r.t. the focal plane center, and another variable for the beam angle w.r.t. the filter

normal).

An example is shown on figure (3.12). The agreement between the calibration frame and the model is quite good, and all the ghosts are predicted at the correct location. This means that the optics of the imager is well understood, and that the position and orientation of the source relative to the telescope is well controlled, for each exposure.

The large scale extraction of direct light has proved difficult to automate, however. We are still working on a robust direct light extraction technique, that would be immune to the small alignment uncertainties that affect the predicted position of ghosts by a few pixels. With such a technique in hand, we expect to be able to model the contamination with an accuracy of a few percents, hence, to determine the direct illumination at the per-mil level. This will allow us to maps the filters and also to determine photometric flat fields, free from indirect light contamination.

Conclusion

Modern precision cosmology, such as the measurement of the Dark Energy equation of state with type Ia supernovae (SNe Ia) sets very tight constraints on the accuracy of the flux calibration of the dark energy surveys. Indeed, the measurement of the luminosity distance of high-redshift (resp. low-redshift) supernovae is primarily performed with the redder (resp. bluer) bands of the imagers. Hence, measuring cosmological parameters with SNe Ia ultimately boils down to comparing fluxes measured either with red and blue passbands and it is fundamental to control the intercalibration of the imager passbands. Taking full advantage of statistics and quality of SN Ia measurements requires to control this intercalibration with an accuracy of a fraction of a percent.

The wavelength positioning of the survey passbands has also a sizeable impact on the cosmological parameter measurements. The required wavelength accuracy on the filter cut-offs is as low as a fraction of a nanometer. Passband models are usually derived from pre-installation test-bench measurements of the imager optical components. This is not entirely satisfactory, as filters may evolve over time time as shown by previous studies, and it seems necessary to be able to measure and follow up *in situ* the instrument passbands.

The current photometric calibration techniques rely on observations of spectrophotometric stellar calibrators. Establishing such primary standards is notoriously difficult, as one has to anchor astronomical observations to a physical flux scale. One of the best efforts so far is the work of the CALSPEC team. The CALSPEC flux scale relies on NLTE *models* of three pure hydrogen white dwarfs. These stars are the primary standards used to calibrate the flux response of the HST instruments, in particular STIS and NICMOS, which are used in turn to extend the CALSPEC library by adding secondary spectrophotometric standards. Modern supernova surveys have chosen to anchor their flux calibration on this so-called HST white dwarf flux scale. The uncertainty that affects the spectrum of the primary standards is however difficult to assess. As the precision of the calibration efforts improves, it seems increasingly important to check these stellar calibrators using laboratory standards.

Instrumental calibration is today a very active subject. Many different light source projects have been proposed and it is quite difficult to predict which design is going to prevail in future surveys. DICE is one of those attempts. It consists in a compact, versatile, inexpensive LED based calibrated light source, that can be placed in the dome of virtually any telescope. As a point like source placed at a finite distance, it generates a conical beam that yields a quasi-uniform focal plane illumination. This is complemented by a pencil beam that allows (1) to control the relative positions and

orientations of the source and the telescope and (2) to study in detail the ghost contamination. The stability of the light source, permits to carry out a daily monitoring of the telescope and imager response. The simplicity of the calibration beams, combined with the complementarity pencil beam / conical beam allows to derive an accurate estimate of the telescope throughput, taking into account the contamination by ghosts.

The largely unanticipated impact of ghost contamination reminds us that broadband imagers have significantly grown in size and complexity. Characterizing such objects now means extracting O(1000) calibration parameters — from the gains of the readout electronics, to the passband transmissions at various focal plane locations. There is no doubt that the calibration of future wide field cameras, such as DECam and LSST will rely on a combination of artificial sources and a model of the instrument such as the one described above. Today's wide field imagers, such as MegaCam offer a unique opportunity to develop these tools and test them on real data.

Bibliography

R. Tripp, A&A **331**, 815 (1998), ADS. 7, 11, 22

P. Astier, J. Guy, N. Regnault, R. Pain, E. Aubourg, D. Balam, S. Basa, R. G. Carlberg, S. Fabbro, D. Fouchez, et al., A&A **447**, 31 (2006), arXiv:astro-ph/0510447. 7, 22, 30

S. Perlmutter, G. Aldering, G. Goldhaber, R. A. Knop, P. Nugent, P. G. Castro, S. Deustua, S. Fabbro, A. Goobar, D. E. Groom, et al., ApJ **517**, 565 (1999), arXiv:astro-ph/9812133. 9, 11, 22, 28, 29

A. G. Riess, A. V. Filippenko, P. Challis, A. Clocchiatti, A. Diercks, P. M. Garnavich, R. L. Gilliland, C. J. Hogan, S. Jha, R. P. Kirshner, et al., AJ **116**, 1009 (1998), arXiv:astro-ph/9805201. 9, 11, 22, 30

G. Efstathiou, W. J. Sutherland, and S. J. Maddox, Nature **348**, 705 (1990), ADS. 9

N. A. Bahcall and X. Fan, ApJ **504**, 1 (1998), arXiv:astro-ph/9803277. 9

S. D. M. White, J. F. Navarro, A. E. Evrard, and C. S. Frenk, Nature **366**, 429 (1993), ADS. 9

B. Chaboyer, P. Demarque, P. J. Kernan, and L. M. Krauss, Science **271**, 957 (1996), arXiv:astro-ph/9509115. 9

A. Sandage, ApJ **133**, 355 (1961), ADS. 9, 17

P. de Bernardis, P. A. R. Ade, J. J. Bock, J. R. Bond, J. Borrill, A. Boscaleri, K. Coble, B. P. Crill, G. De Gasperis, P. C. Farese, et al., Nature **404**, 955 (2000), arXiv:astro-ph/0004404. 9

W. L. Freedman, B. F. Madore, B. K. Gibson, L. Ferrarese, D. D. Kelson, S. Sakai, J. R. Mould, R. C. Kennicutt, Jr., H. C. Ford, J. A. Graham, et al., ApJ **553**, 47 (2001), arXiv:astro-ph/0012376. 9, 11, 15

N. Suzuki, D. Rubin, C. Lidman, G. Aldering, R. Amanullah, K. Barbary, L. F. Barrientos, J. Botyanszki, M. Brodwin, N. Connolly, et al., ApJ **746**, 85 (2012), arXiv:1105.3470. 9, 29, 30

E. Komatsu, K. M. Smith, J. Dunkley, C. L. Bennett, B. Gold, G. Hinshaw, N. Jarosik, D. Larson, M. R. Nolta, L. Page, et al., ApJS **192**, 18 (2011), arXiv:1001.4538. 9, 32

B. D. Fields and K. A. Olive, Nuclear Physics A **777**, 208 (2006), ADS. 9

W. J. Percival, R. C. Nichol, D. J. Eisenstein, J. A. Frieman, M. Fukugita, J. Loveday, A. C. Pope, D. P. Schneider, A. S. Szalay, M. Tegmark, et al., ApJ **657**, 645 (2007a), arXiv:astro-ph/0608636. 9

L. Anderson, E. Aubourg, S. Bailey, D. Bizyaev, M. Blanton, A. S. Bolton, J. Brinkmann, J. R. Brownstein, A. Burden, A. J. Cuesta, et al., ArXiv e-prints (2012), arXiv:1203.6594. 10, 32

W. J. Percival, S. Cole, D. J. Eisenstein, R. C. Nichol, J. A. Peacock, A. C. Pope, and A. S. Szalay, MNRAS **381**, 1053 (2007b), arXiv:0705.3323. 10

D. J. Eisenstein, I. Zehavi, D. W. Hogg, R. Scoccimarro, M. R. Blanton, R. C. Nichol, R. Scranton, H.-J. Seo, M. Tegmark, Z. Zheng, et al., ApJ **633**, 560 (2005), arXiv:astro-ph/0501171. 10

J. L. Feng, Annual Review of Astronomy and Astrophysics **48**, 495 (2010), arXiv:1003.0904. 10

G. Bertone, D. Hooper, and J. Silk, Physics Reports **405**, 279 (2005), arXiv:hep-ph/0404175. 10

T. A. Porter, R. P. Johnson, and P. W. Graham, Annual Review of Astronomy and Astrophysics **49**, 155 (2011), arXiv:1104.2836. 10

P. L. Brink, Journal of Low Temperature Physics **167**, 1048 (2012), ADS. 10

J. Martin, Comptes Rendus Physique **13**, 566 (2012), arXiv:1205.3365. 10

S. M. Carroll, Living Reviews in Relativity **4**, 1 (2001), arXiv:astro-ph/0004075. 10

S. Weinberg, Reviews of Modern Physics **61**, 1 (1989), ADS. 10

M. Kunz, Comptes Rendus Physique **13**, 539 (2012), arXiv:1204.5482. 10

E. J. Copeland, M. Sami, and S. Tsujikawa, International Journal of Modern Physics D **15**, 1753 (2006), arXiv:hep-th/0603057. 10

A. G. Riess, W. H. Press, and R. P. Kirshner, ApJ **473**, 88 (1996), arXiv:astro-ph/9604143. 11, 22

M. M. Phillips, ApJ **413**, L105 (1993), ADS. 11, 22, 29

Y. P. Pskovskii, Soviet Ast. **28**, 658 (1984), ADS. 11, 22

A. Conley, J. Guy, M. Sullivan, N. Regnault, P. Astier, C. Balland, S. Basa, R. G. Carlberg, D. Fouchez, D. Hardin, et al., ApJS **192**, 1 (2011), arXiv:1104.1443. 12, 30, 31, 34, 35

M. Betoule, J. Marriner, N. Regnault, J.-C. Cuillandre, P. Astier, and J. Guy, A&A (2012). 12, 45, 57, 58, 59, 60, 61, 62, 69

N. Regnault, A. Conley, J. Guy, M. Sullivan, J.-C. Cuillandre, P. Astier, C. Balland, S. Basa, R. G. Carlberg, D. Fouchez, et al., A&A **506**, 999 (2009), arXiv:0908.3808. 12, 55, 56, 57, 59, 61, 69

J. A. Holtzman, J. Marriner, R. Kessler, M. Sako, B. Dilday, J. A. Frieman, D. P. Schneider, B. Bassett, A. Becker, D. Cinabro, et al., AJ **136**, 2306 (2008), arXiv:0908.4277. 12, 30, 56, 57, 69

C. W. Stubbs, P. Doherty, C. Cramer, G. Narayan, Y. J. Brown, K. R. Lykke, J. T. Woodward, and J. L. Tonry, ApJS **191**, 376 (2010), arXiv:1003.3465. 12, 76, 77

M. Doi, M. Tanaka, M. Fukugita, J. E. Gunn, N. Yasuda, Ž. Ivezić, J. Brinkmann, E. de Haars, S. J. Kleinman, J. Krzesinski, et al., AJ **139**, 1628 (2010), arXiv:1002.3701. 12, 38, 63, 76, 77

E. Barrelet and C. Juramy, Nuclear Instruments and Methods in Physics Research A **585**, 93 (2008), ADS. 12, 78

J. Rich, *Fundamentals of Cosmology* (2010), ADS. 13

S. Dodelson, *Modern cosmology* (2003), ADS. 13

J. A. Peacock, *Cosmological Physics* (1999), ADS. 13

H. P. Robertson, Proceedings of the National Academy of Science **15**, 822 (1929), ADS. 13

A. G. Walker, Proceedings of the London Mathematical Society **42**, 90 (1936). 13

A. Friedmann, Zeitschrift fur Physik **10**, 377 (1922), ADS. 13

J. A. Frieman, M. S. Turner, and D. Huterer, Annual Review of Astronomy and Astrophysics **46**, 385 (2008), arXiv:0803.0982. 15

A. G. Riess, L. Macri, S. Casertano, M. Sosey, H. Lampeitl, H. C. Ferguson, A. V. Filippenko, S. W. Jha, W. Li, R. Chornock, et al., ApJ **699**, 539 (2009), arXiv:0905.0695. 15

E. Hubble and M. L. Humason, ApJ **74**, 43 (1931), ADS. 17

E. Hubble, Proceedings of the National Academy of Science **15**, 168 (1929), ADS. 17

G. Lemaître, Annales de la Société Scientifique de Bruxelles **47**, 49 (1927), ADS. 17

A. Sandage, Annual Review of Astronomy and Astrophysics **26**, 561 (1988), ADS. 17

W. Baade and F. Zwicky, Proceedings of the National Academy of Science **20**, 254 (1934), ADS. 17

R. Minkowski, PASP **53**, 224 (1941), ADS. 18

J. C. Wheeler and R. P. Harkness, Reports on Progress in Physics **53**, 1467 (1990), ADS. 18

J. H. Elias, K. Matthews, G. Neugebauer, and S. E. Persson, ApJ **296**, 379 (1985), ADS. 18

B. T. Hayden, P. M. Garnavich, R. Kessler, J. A. Frieman, S. W. Jha, B. Bassett, D. Cinabro, B. Dilday, D. Kasen, J. Marriner, et al., ApJ **712**, 350 (2010), arXiv:1001.3428. 18

W. D. Arnett, ApJ **253**, 785 (1982), ADS. 18

F. Hoyle and W. A. Fowler, ApJ **132**, 565 (1960), ADS. 20

W. Hillebrandt and J. C. Niemeyer, Annual Review of Astronomy and Astrophysics **38**, 191 (2000), arXiv:astro-ph/0006305. 20

A. M. Khokhlov, A&A **245**, 114 (1991), ADS. 20

D. Kasen, F. K. Röpke, and S. E. Woosley, Nature **460**, 869 (2009), arXiv:0907.0708. 20

M. Livio, in *Type Ia Supernovae, Theory and Cosmology*, edited by J. C. Niemeyer and J. W. Truran (2000), p. 33, arXiv:astro-ph/9903264. 20

J. Whelan and I. Iben, Jr., ApJ **186**, 1007 (1973), ADS. 20

B. Dilday, D. A. Howell, S. B. Cenko, J. M. Silverman, P. E. Nugent, M. Sullivan, S. Ben-Ami, L. Bildsten, M. Bolte, M. Endl, et al., Science **337**, 942 (2012), arXiv:1207.1306. 21

I. Iben, Jr. and A. V. Tutukov, ApJS **54**, 335 (1984), ADS. 21

K. Nomoto and I. Iben, Jr., ApJ **297**, 531 (1985), ADS. 21

H. Saio and K. Nomoto, A&A **150**, L21 (1985), ADS. 21

K. Nomoto and Y. Kondo, ApJ **367**, L19 (1991), ADS. 21

R. Pakmor, M. Kromer, S. Taubenberger, S. A. Sim, F. K. Röpke, and W. Hillebrandt, ApJ **747**, L10 (2012), arXiv:1201.5123. 21

F. K. Röpke, M. Kromer, I. R. Seitenzahl, R. Pakmor, S. A. Sim, S. Taubenberger, F. Ciaraldi-Schoolmann, W. Hillebrandt, G. Aldering, P. Antilogus, et al., ApJ **750**, L19 (2012), arXiv:1203.4839. 21

M. Fink, W. Hillebrandt, and F. K. Röpke, A&A **476**, 1133 (2007), arXiv:0710.5486. 21

M. Fink, F. K. Röpke, W. Hillebrandt, I. R. Seitenzahl, S. A. Sim, and M. Kromer, A&A **514**, A53 (2010), arXiv:1002.2173. 21

O. C. Wilson, ApJ **90**, 634 (1939), ADS. 22

W. Baade, ApJ **88**, 285 (1938), ADS. 22

I. P. Pskovskii, Soviet Ast. **21**, 675 (1977), ADS. 22

M. Hamuy, M. M. Phillips, N. B. Suntzeff, R. A. Schommer, J. Maza, and R. Aviles, AJ **112**, 2398 (1996a), arXiv:astro-ph/9609062. 22, 29

M. Hamuy, M. M. Phillips, N. B. Suntzeff, R. A. Schommer, J. Maza, and R. Aviles, AJ **112**, 2391 (1996b), arXiv:astro-ph/9609059. 22, 23

R. Kessler, A. C. Becker, D. Cinabro, J. Vanderplas, J. A. Frieman, J. Marriner, T. M. Davis, B. Dilday, J. Holtzman, S. W. Jha, et al., ApJS **185**, 32 (2009), arXiv:0908.4274. 23, 29, 30

M. Sullivan, D. Le Borgne, C. J. Pritchet, A. Hodsman, J. D. Neill, D. A. Howell, R. G. Carlberg, P. Astier, E. Aubourg, D. Balam, et al., ApJ **648**, 868 (2006), arXiv:astro-ph/0605455. 23

F. Mannucci, M. Della Valle, N. Panagia, E. Cappellaro, G. Cresci, R. Maiolino, A. Petrosian, and M. Turatto, A&A **433**, 807 (2005), arXiv:astro-ph/0411450. 23

D. A. Howell, M. Sullivan, A. Conley, and R. Carlberg, ApJ **667**, L37 (2007), arXiv:astro-ph/0701912. 23

M. Sullivan, A. Conley, D. A. Howell, J. D. Neill, P. Astier, C. Balland, S. Basa, R. G. Carlberg, D. Fouchez, J. Guy, et al., MNRAS **406**, 782 (2010), arXiv:1003.5119. 23, 29

H. Lampeitl, M. Smith, R. C. Nichol, B. Bassett, D. Cinabro, B. Dilday, R. J. Foley, J. A. Frieman, P. M. Garnavich, A. Goobar, et al., ApJ **722**, 566 (2010), arXiv:1005.4687. 23

P. L. Kelly, M. Hicken, D. L. Burke, K. S. Mandel, and R. P. Kirshner, ApJ **715**, 743 (2010), arXiv:0912.0929. 23

M. S. Bessell, PASP **102**, 1181 (1990), ADS. 24

M. Fukugita, T. Ichikawa, J. E. Gunn, M. Doi, K. Shimasaku, and D. P. Schneider, Astronomical Journal **111**, 1748 (1996), URL `http://adsabs.harvard.edu/abs/1996AJ...111.1748F`. 24

O. Boulade, X. Charlot, P. Abbon, S. Aune, P. Borgeaud, P.-H. Carton, M. Carty, J. Da Costa, H. Deschamps, D. Desforge, et al., in *Society of Photo-Optical Instrumentation Engineers (SPIE) Conference Series*, edited by M. Iye & A. F. M. Moorwood (2003), vol. 4841 of *Society of Photo-Optical Instrumentation Engineers (SPIE) Conference Series*, pp. 72–81. 24

K. Honscheid, D. L. DePoy, and for the DES Collaboration, ArXiv e-prints (2008), arXiv:0810.3600. 24

G. H. Rieke, Annual Review of Astronomy and Astrophysics **45**, 77 (2007), ADS. 24

L. Amendola, S. Appleby, D. Bacon, T. Baker, M. Baldi, N. Bartolo, A. Blanchard, C. Bonvin, S. Borgani, E. Branchini, et al., ArXiv e-prints (2012), arXiv:1206.1225. 25, 32

J. Green, P. Schechter, C. Baltay, R. Bean, D. Bennett, R. Brown, C. Conselice, M. Donahue, X. Fan, B. S. Gaudi, et al., ArXiv e-prints (2012), arXiv:1208.4012. 25, 32

R. Kessler, B. Bassett, P. Belov, V. Bhatnagar, H. Campbell, A. Conley, J. A. Frieman, A. Glazov, S. González-Gaitán, R. Hlozek, et al., PASP **122**, 1415 (2010), arXiv:1008.1024. 26

C. Lidman, V. Ruhlmann-Kleider, M. Sullivan, J. Myzska, P. Dobbie, K. Glazebrook, J. Mould, P. Astier, C. Balland, M. Betoule, et al., ArXiv e-prints (2012), arXiv:1205.1306. 26

R. Sharp, W. Saunders, G. Smith, V. Churilov, D. Correll, J. Dawson, T. Farrel, G. Frost, R. Haynes, R. Heald, et al., in *Society of Photo-Optical Instrumentation Engineers (SPIE) Conference Series* (2006), vol. 6269 of *Society of Photo-Optical Instrumentation Engineers (SPIE) Conference Series*, arXiv:astro-ph/0606137. 26

P. R. Newman, D. C. Long, S. A. Snedden, S. J. Kleinman, A. Nitta, M. Harvanek, J. Krzesinski, H. J. Brewington, J. C. Barentine, E. H. Neilsen, Jr., et al., in *Society of Photo-Optical Instrumentation Engineers (SPIE) Conference Series*, edited by A. F. M. Moorwood and M. Iye (2004), vol. 5492 of *Society of Photo-Optical Instrumentation Engineers (SPIE) Conference Series*, pp. 533–544, arXiv:astro-ph/0408167. 26

S. Smee, J. E. Gunn, A. Uomoto, N. Roe, D. Schlegel, C. M. Rockosi, M. A. Carr, F. Leger, K. S. Dawson, M. D. Olmstead, et al., ArXiv e-prints (2012), arXiv:1208.2233. 26

S. Jha, A. G. Riess, and R. P. Kirshner, ApJ **659**, 122 (2007), arXiv:astro-ph/0612666. 27

J. Guy, P. Astier, S. Baumont, D. Hardin, R. Pain, N. Regnault, S. Basa, R. G. Carlberg, A. Conley, S. Fabbro, et al., A&A **466**, 11 (2007), arXiv:astro-ph/0701828. 27, 28

A. Conley, M. Sullivan, E. Y. Hsiao, J. Guy, P. Astier, D. Balam, C. Balland, S. Basa, R. G. Carlberg, D. Fouchez, et al., ApJ **681**, 482 (2008), arXiv:0803.3441. 27

J. Guy, M. Sullivan, A. Conley, N. Regnault, P. Astier, C. Balland, S. Basa, R. G. Carlberg, D. Fouchez, D. Hardin, et al., A&A **523**, A7 (2010), arXiv:1010.4743. 29, 34

S. Bailey, G. Aldering, P. Antilogus, C. Aragon, C. Baltay, S. Bongard, C. Buton, M. Childress, N. Chotard, Y. Copin, et al., A&A **500**, L17 (2009), arXiv:0905.0340. 29

L. Wang, G. Goldhaber, G. Aldering, and S. Perlmutter, ApJ **590**, 944 (2003), arXiv:astro-ph/0302341. 29

A. Conley, G. Goldhaber, L. Wang, G. Aldering, R. Amanullah, E. D. Commins, V. Fadeyev, G. Folatelli, G. Garavini, R. Gibbons, et al., ApJ **644**, 1 (2006), arXiv:astro-ph/0602411. 29

M. Sullivan, J. Guy, A. Conley, N. Regnault, P. Astier, C. Balland, S. Basa, R. G. Carlberg, D. Fouchez, D. Hardin, et al., ApJ **737**, 102 (2011), arXiv:1104.1444. 29, 30

M. Hamuy, J. Maza, M. M. Phillips, N. B. Suntzeff, M. Wischnjewsky, R. C. Smith, R. Antezana, L. A. Wells, L. E. Gonzalez, P. Gigoux, et al., AJ **106**, 2392 (1993), ADS. 29

M. Hamuy, M. M. Phillips, J. Maza, N. B. Suntzeff, R. A. Schommer, and R. Aviles, AJ **109**, 1 (1995), ADS. 29

R. A. Knop, G. Aldering, R. Amanullah, P. Astier, G. Blanc, M. S. Burns, A. Conley, S. E. Deustua, M. Doi, R. Ellis, et al., ApJ **598**, 102 (2003), arXiv:astro-ph/0309368. 30

A. G. Riess, L.-G. Strolger, S. Casertano, H. C. Ferguson, B. Mobasher, B. Gold, P. J. Challis, A. V. Filippenko, S. Jha, W. Li, et al., ApJ **659**, 98 (2007), arXiv:astro-ph/0611572. 30

A. G. Riess, L.-G. Strolger, J. Tonry, S. Casertano, H. C. Ferguson, B. Mobasher, P. Challis, A. V. Filippenko, S. Jha, W. Li, et al., ApJ **607**, 665 (2004), arXiv:astro-ph/0402512. 30

M. Hicken, P. Challis, R. P. Kirshner, A. Rest, C. E. Cramer, W. M. Wood-Vasey, G. Bakos, P. Berlind, W. R. Brown, N. Caldwell, et al., ApJS **200**, 12 (2012), arXiv:1205.4493. 30

S. Blondin, T. Matheson, R. P. Kirshner, K. S. Mandel, P. Berlind, M. Calkins, P. Challis, P. M. Garnavich, S. W. Jha, M. Modjaz, et al., AJ **143**, 126 (2012), arXiv:1203.4832. 30

M. D. Stritzinger, M. M. Phillips, L. N. Boldt, C. Burns, A. Campillay, C. Contreras, S. Gonzalez, G. Folatelli, N. Morrell, W. Krzeminski, et al., AJ **142**, 156 (2011), arXiv:1108.3108. 30

G. Folatelli, M. M. Phillips, C. R. Burns, C. Contreras, M. Hamuy, W. L. Freedman, S. E. Persson, M. Stritzinger, N. B. Suntzeff, K. Krisciunas, et al., AJ **139**, 120 (2010), arXiv:0910.3317. 30

J. M. Silverman, R. J. Foley, A. V. Filippenko, M. Ganeshalingam, A. J. Barth, R. Chornock, C. V. Griffith, J. J. Kong, N. Lee, D. C. Leonard, et al., MNRAS **425**, 1789 (2012), arXiv:1202.2128. 30

W. J. Percival, B. A. Reid, D. J. Eisenstein, N. A. Bahcall, T. Budavari, J. A. Frieman, M. Fukugita, J. E. Gunn, Ž. Ivezić, G. R. Knapp, et al., MNRAS **401**, 2148 (2010), arXiv:0907.1660. 32

A. Albrecht, G. Bernstein, R. Cahn, W. L. Freedman, J. Hewitt, W. Hu, J. Huth, M. Kamionkowski, E. W. Kolb, L. Knox, et al., ArXiv Astrophysics e-prints (2006), arXiv:astro-ph/0609591. 32

J. A. Peacock, P. Schneider, G. Efstathiou, J. R. Ellis, B. Leibundgut, S. J. Lilly, and Y. Mellier, Tech. Rep. (2006), arXiv:astro-ph/0610906. 32

Y. Suto, in *Society of Photo-Optical Instrumentation Engineers (SPIE) Conference Series* (2010), vol. 7733 of *Society of Photo-Optical Instrumentation Engineers (SPIE) Conference Series*, arXiv:1007.1256. 32

J. E. Gunn, M. Carr, S. A. Smee, J. D. Orndorff, R. H. Barkhouser, M. Hart, C. L. Bennett, J. E. Greene, T. Heckman, H. Karoji, et al., ArXiv e-prints (2012), arXiv:1210.2740. 32

K. S. Dawson, D. J. Schlegel, C. P. Ahn, S. F. Anderson, É. Aubourg, S. Bailey, R. H. Barkhouser, J. E. Bautista, A. Beifiori, A. A. Berlind, et al., ArXiv e-prints (2012), arXiv:1208.0022. 32

LSST DESC, ArXiv e-prints (2012), arXiv:1211.0310. 32

J. P. Bernstein, R. Kessler, S. Kuhlmann, R. Biswas, E. Kovacs, G. Aldering, I. Crane, C. B. D'Andrea, D. A. Finley, J. A. Frieman, et al., ApJ **753**, 152 (2012), arXiv:1111.1969. 33

K. Perrett, M. Sullivan, A. Conley, S. González-Gaitán, R. Carlberg, D. Fouchez, P. Ripoche, J. D. Neill, P. Astier, D. Balam, et al., AJ **144**, 59 (2012), arXiv:1206.0665. 34

C. Buton, Y. Copin, G. Aldering, P. Antilogus, C. Aragon, S. Bailey, C. Baltay, S. Bongard, A. Canto, F. Cellier-Holzem, et al., ArXiv e-prints (2012), arXiv:1210.2619. 38, 64, 65

H. Tüg, N. M. White, and G. W. Lockwood, A&A **61**, 679 (1977), ADS. 40

D. S. Hayes, D. W. Latham, and S. H. Hayes, ApJ **197**, 587 (1975), ADS. 40

D. S. Hayes and D. W. Latham, ApJ **197**, 593 (1975), ADS. 40

J. B. Oke and R. E. Schild, ApJ **161**, 1015 (1970), ADS. 40

D. S. Hayes, ApJ **159**, 165 (1970), ADS. 40

D. S. Hayes, in *Calibration of Fundamental Stellar Quantities*, edited by D. S. Hayes, L. E. Pasinetti, and A. G. D. Philip (1985), vol. 111 of *IAU Symposium*, pp. 225–249. 40, 44, 71

D. S. Finley and D. Koester, in *Bulletin of the American Astronomical Society* (1991), vol. 23 of *Bulletin of the American Astronomical Society*, p. 907. 40

R. Kurucz, ATLAS9 Stellar Atmosphere Programs and 2 km/s grid. Kurucz CD-ROM No. 13. Cambridge, Mass.: Smithsonian Astrophysical Observatory, 1993. **13** (1993), ADS. 41

I. Hubeny and T. Lanz, Astrophysics Source Code Library p. 9022 (2011), ADS. 41

I. Hubeny and T. Lanz, ApJ **439**, 875 (1995), ADS. 41

P. H. Hauschildt, S. Starrfield, S. N. Shore, F. Allard, and E. Baron, ApJ **447**, 829 (1995), ADS. 41

K. Werner, J. L. Deetjen, S. Dreizler, T. Nagel, T. Rauch, and S. L. Schuh, in *Stellar Atmosphere Modeling*, edited by I. Hubeny, D. Mihalas, and K. Werner (2003), vol. 288 of *Astronomical Society of the Pacific Conference Series*, p. 31, arXiv:astro-ph/0209535. 42

T. Rauch and J. L. Deetjen, in *Stellar Atmosphere Modeling*, edited by I. Hubeny, D. Mihalas, and K. Werner (2003), vol. 288 of *Astronomical Society of the Pacific Conference Series*, p. 103, arXiv:astro-ph/0403239. 42

P.-E. Tremblay and P. Bergeron, ApJ **696**, 1755 (2009), arXiv:0902.4182. 42, 43

P. Bergeron, D. Saumon, and F. Wesemael, ApJ **443**, 764 (1995), ADS. 42

CALSPEC, *Calspec*, http://www.stsci.edu/hst/observatory/cdbs/calspec.html (2011), URL `http://www.stsci.edu/hst/observatory/cdbs/calspec.html`. 42, 55, 57, 69

M. A. Barstow, J. B. Holberg, I. Hubeny, S. A. Good, A. J. Levan, and F. Meru, MNRAS **328**, 211 (2001), arXiv:astro-ph/0107529. 42

D. S. Finley, D. Koester, and G. Basri, ApJ **488**, 375 (1997), ADS. 43

A. Gianninas, P. Bergeron, and M. T. Ruiz, ApJ **743**, 138 (2011), arXiv:1109.3171. 43

D. Koester, H. Schulz, and V. Weidemann, A&A **76**, 262 (1979), ADS. 42

R. C. Bohlin, L. Colina, and D. S. Finley, AJ **110**, 1316 (1995), ADS. 43

R. C. Bohlin, in *The Future of Photometric, Spectrophotometric and Polarimetric Standardization*, edited by C. Sterken (2007), vol. 364 of *Astronomical Society of the Pacific Conference Series*, p. 315, arXiv:astro-ph/0608715. 43

R. C. Bohlin, in *HST Calibration Workshop : Hubble after the Installation of the ACS and the NICMOS Cooling System*, edited by S. Arribas, A. Koekemoer, and B. Whitmore (2003), p. 115. 43

R. C. Bohlin, M. E. Dickinson, and D. Calzetti, AJ **122**, 2118 (2001), ADS. 43

R. C. Bohlin, AJ **120**, 437 (2000), ADS. 43

R. C. Bohlin and R. L. Gilliland, AJ **128**, 3053 (2004a), ADS. 44

R. C. Bohlin and R. L. Gilliland, AJ **127**, 3508 (2004b), ADS. 44

A. U. Landolt, AJ **104**, 340 (1992), ADS. 53, 54, 57, 69

A. U. Landolt, AJ **88**, 439 (1983), ADS. 54

H. L. Johnson and W. W. Morgan, ApJ **117**, 313 (1953), ADS. 54

G. E. Kron, S. C. B. Gascoigne, and H. S. White, AJ **62**, 205 (1957), ADS. 54

A. W. J. Cousins, MmRAS **81**, 25 (1976), ADS. 54

A. U. Landolt, AJ **78**, 959 (1973), ADS. 54

A. U. Landolt, in *The Future of Photometric, Spectrophotometric and Polarimetric Standardization*, edited by C. Sterken (2007), vol. 364 of *Astronomical Society of the Pacific Conference Series*, pp. 27–+. 53

A. U. Landolt and A. K. Uomoto, AJ **133**, 768 (2007), arXiv:0704.3030. 53, 55, 57, 69

J. Manfroid, F. Selman, and H. Jones, The Messenger **104**, 16 (2001), ADS. 60, 61

J. Manfroid, A&A Suppl. **113**, 587 (1995), ADS. 60

E. A. Magnier and J.-C. Cuillandre, PASP **116**, 449 (2004), ADS. 61

N. Padmanabhan, D. J. Schlegel, D. P. Finkbeiner, J. C. Barentine, M. R. Blanton, H. J. Brewington, J. E. Gunn, M. Harvanek, D. W. Hogg, Ž. Ivezić, et al., ApJ **674**, 1217 (2008), arXiv:astro-ph/0703454. 63

C. W. Stubbs, F. W. High, M. R. George, K. L. DeRose, S. Blondin, J. L. Tonry, K. C. Chambers, B. R. Granett, D. L. Burke, and R. C. Smith, PASP **119**, 1163 (2007a), arXiv:0708.1364. 63

D. L. Burke, T. Axelrod, S. Blondin, C. Claver, Ž. Ivezić, L. Jones, A. Saha, A. Smith, R. C. Smith, and C. W. Stubbs, ApJ **720**, 811 (2010), ADS. 64

J. M. Houston and J. P. Rice, Metrologia **43**, 31 (2006), ADS. 72

S. W. Brown, G. P. Eppeldauer, and K. R. Lykke, Appl. Opt. **45**, 8218 (2006), ADS. 72

S. W. Brown, G. P. Eppeldauer, and K. R. Lykke, Metrologia **37**, 579 (2000), ADS. 72

M. E. Kaiser, S. R. McCandliss, R. Pelton, D. Sahnow, W. V. Dixon, P. D. Feldman, B. W. Gaither, J. S. Lazear, H. W. Moos, A. Riess, et al., in *Hubble after SM4. Preparing JWST* (2010a). 74

M. E. Kaiser, J. W. Kruk, S. R. McCandliss, D. J. Sahnow, R. H. Barkhouser, W. Van Dixon, P. D. Feldman, H. W. Moos, J. Orndorff, R. Pelton, et al., ArXiv e-prints (2010b), arXiv:1001.3925. 74

J. T. McGraw, P. C. Zimmer, D. C. Zirzow, J. T. Woodward, K. R. Lykke, C. E. Cramer, S. E. Deustua, and D. C. Hines, in *Society of Photo-Optical Instrumentation Engineers (SPIE) Conference Series* (2012), vol. 8450 of *Society of Photo-Optical Instrumentation Engineers (SPIE) Conference Series*. 75

J. L. Marshall and D. L. DePoy, ArXiv Astrophysics e-prints (2005), arXiv:astro-ph/0510233. 76

C. W. Stubbs, S. K. Slater, Y. J. Brown, D. Sherman, R. C. Smith, J. L. Tonry, N. B. Suntzeff, A. Saha, J. Masiero, and S. Rodney, in *The Future of Photometric, Spectrophotometric and Polarimetric Standardization*, edited by C. Sterken (2007b), vol. 364 of *Astronomical Society of the Pacific Conference Series*, p. 373, arXiv:astro-ph/0609260. 77

J.-P. Rheault, D. L. Depoy, T. W. Behm, E. W. Kylberg, K. Cabral, R. Allen, and J. L. Marshall, in *Society of Photo-Optical Instrumentation Engineers (SPIE) Conference Series* (2010), vol. 7735 of *Society of Photo-Optical Instrumentation Engineers (SPIE) Conference Series*. 77

J. E. Albert, M. H. Fagin, Y. J. Brown, C. W. Stubbs, N. A. Kuklev, and A. J. Conley, ArXiv e-prints (2012), arXiv:1207.1938. 77

S. C. Keller, B. P. Schmidt, M. S. Bessell, P. G. Conroy, P. Francis, A. Granlund, E. Kowald, A. P. Oates, T. Martin-Jones, T. Preston, et al., Publications of the Astronomical Society of Australia **24**, 1 (2007), arXiv:astro-ph/0702511. 78

A. Guyonnet, Ph.D. thesis, Université Pierre et Marie Curie (2012). 85, 90

F. Villa, Ph.D. thesis, Université Pierre et Marie Curie (2012). 90